WHICH ENVIRONMENTAL CONDITIONS AND CORE PRECIPITATION CHARACTERISTICS LED TO THE RAPID INTENSIFICATION OF HURRICANE EARL (2010)?

by

Gabriel Anthony Susca-Lopata

A thesis submitted to the faculty of
The University of Utah
in partial fulfillment of the requirements for the degree of

Master of Science

Department of Atmospheric Sciences

The University of Utah

August 2014

Copyright © Gabriel Anthony Susca-Lopata 2014

All Rights Reserved

The University of Utah Graduate School

STATEMENT OF THESIS APPROVAL

The thesis of **Gabriel Anthony Susca-Lopata**

has been approved by the following supervisory committee members:

Edward J. Zipser , Chair **3/24/2014**
Date Approved

Zhaoxia Pu , Member **3/24/2014**
Date Approved

William James Steenburgh , Member **3/24/2014**
Date Approved

and by **Kevin Perry** , Chair/Dean of

the Department/College/School of **Atmospheric Sciences**

and by David B. Kieda, Dean of The Graduate School.

ABSTRACT

Global analysis fields, infrared and passive microwave satellite observations, lightning data, and airborne radar reflectivity and dual-Doppler wind analyses show the evolution of environmental conditions, precipitation characteristics, and kinematic structure before, during, and after the rapid intensification (RI) of Hurricane Earl (2010). The relationship between the RI and environmental conditions, intense inner-core convection, inner-core precipitation coverage, core cold-cloud precipitation symmetry, and the radial distribution of convection is examined.

The onset of RI occurs despite moderate vertical wind shear. An episode of intense convection occurs before the RI onset, but an examination of the mesoscale and convective-scale kinematic processes during this convective 'burst' suggests that the strength of convection alone did not cause the onset of RI. Instead, the dual-Doppler, lightning, and microwave data suggest that the precipitation characteristic that ultimately led to the onset of RI was an increasing trend in cold-cloud precipitation symmetry following the migration of inner-core convection into the northeastern and northern quadrants of the storm within a few hours before RI onset.

The evolution of precipitation during the RI suggests that the most important inner-core precipitation characteristics supporting RI are the cold-cloud precipitation symmetry and the predominance of strong convective updrafts within (instead of outside of) the radius of maximum wind (RMW). The wind and precipitation data from Earl indicate that the RMW at multiple levels must be examined. When the RMW is substantially slanted, only considering the low-level RMW can lead to the false conclusion that the strongest convection is located outside of the RMW.

TABLE OF CONTENTS

ABSTRACT iii

ACKNOWLEDGEMENTS vii

CHAPTER

1. INTRODUCTION 1

2. LITERATURE REVIEW 6

    2.1. Impact of Large-Scale Environmental Conditions 6
    2.2. Precipitation Characteristics and Tropical Cyclone Intensity Change 8

3. DATA AND METHODS 11

    3.1. Hurricane Earl 11
    3.2. Global Atmospheric and SST Analyses 12
    3.3. GOES Infrared Brightness Temperatures 13
    3.4. Passive Microwave Satellite Data 13
    3.5. NOAA P3 In Situ and Radar Data 16
    3.6. WWLLN 20
    3.7. Center Fixes 21
    3.8. Variational Mesoscale Analyses 21
    3.9. What Is a Convective Burst? 22

4. LARGE-SCALE ENVIRONMENTAL CONDITIONS 29

5. PRECIPITATION CHARACTERISTICS AND RAPID INTENSIFICATION 39

    5.1. Evolution of Precipitation Characteristics and Kinematic Structure 39
    5.2. Convection, Alignment, and the Onset of RI 46

6. DISCUSSION 84

    6.1. Summary 84

6.2. Conclusions 87

REFERENCES 89

ACKNOWLEDGEMENTS

This research was supported by NASA grants NNX09AC44G and NNX11AB59G under the leadership of Drs. Ramesh Kakar and Scott Braun. I would like to thank my advisor, Dr. Ed Zipser, for providing guidance and teaching during the course of this project. I also thank Dr. Jonathan Zawislak for helpful feedback and advice regarding this research. For all that they have taught me about observations and the behavior of tropical precipitation systems, I thank the members of the University of Utah tropical meteorology group and Dr. Chuntao Liu of Texas A&M University Corpus Christi.

Dr. Rob Rogers, Dr. Paul Reasor, and the radar team at the NOAA Hurricane Research Division (HRD) provided dual-Doppler analyses and Doppler radial velocity data, and contributed important information and instructions for the use of these datasets. Drs. David Raymond and Carlos Lopez Carrillo of New Mexico Tech prepared Doppler radar data for their analysis software and contributed invaluable instructions and advice on the usage of this software. I also wish to thank the World Wide Lightning Location Network (http://wwlln.net), a collaboration among over 50 universities and institutions, for providing the lightning location data used in this thesis. Many other people contributed advice on the data used or considered for this thesis, and I wish to express my appreciation to Dr. Robert Holzworth of the University of Washington (WWLLN), Paola Salio of the University of Buenos Aires (IR), Barry Damiano of the NOAA Aircraft

Operations Center (NOAA P3 in-situ), Dr. Wesley Berg of Colorado State University (SSMI(S)), “Molly” at the National Snow and Ice Data Center (AMSRE), Shirley Murillo of the NOAA HRD (NOAA HWIND), and Simone Tanelli of the NASA Jet Propulsion Laboratory (NASA APR2).

CHAPTER 1

INTRODUCTION

Tropical cyclone (TC) intensity forecasts have improved very slowly in the past few decades, and average National Hurricane Center (NHC) 48-hour intensity forecast errors remain in the range of 10–20 kt (NHC, 2013). Intensity forecasts are particularly poor for rapidly strengthening or weakening TCs. Because of the large forecast errors associated with rapidly intensifying TCs, and the need to more accurately forecast the strength of landfalling storms, improving forecasts of rapidly strengthening storms is a top priority of the hurricane research and forecasting communities (Hurricane Intensity Research Working Group 2006).

TC intensity forecasting is difficult because intensity change is influenced by both large-scale environmental conditions around the storm and smaller scale processes within the vortex core (Marks and Shay 1998). Past research has successfully identified environmental conditions favorable for intensification, and this understanding forms the basis for current statistical TC intensity forecast models (e.g., DeMaria et al. 2005; Kaplan et al. 2010); but debate continues about the relationship between the vortex-to-micro-scale processes within TCs and TC intensity change. Much of the potential improvement in TC intensity forecasting is thought to lie in an improved understanding of the effects of these internal processes.

Some research has addressed the issue of TC internal processes by attempting to determine which kinds of precipitation characteristics lead to TC intensification. This research has yielded varied and sometimes seemingly conflicting results, with potential indicators of intensification including intense inner-core convection (Kelley et al. 2004; Hennon 2006; Guimond et al. 2010), high inner-core coverage of at least moderate rainfall (Cecil and Zipser 1999; Jiang and Ramirez 2013), and axisymmetric convective rings (Willoughby 1990; Harnos and Nesbitt 2011; Kieper and Jiang 2012).

If an improved understanding of the precipitation characteristics conducive to TC intensification is gained, there may already be sufficient routine observations of tropical cyclones to apply these findings in an operational setting. NHC forecasters often use information about the appearance of the clouds and precipitation within a TC to inform their short-term intensity forecasts (e.g., Beven 2005). Several studies have established statistical relationships between TC precipitation characteristics and future intensity change (Cecil and Zipser 1999; Jiang 2012; Jiang and Ramirez 2013; Kieper and Jiang 2012; Rogers et al. 2013a), and recent modeling efforts indicate that some of these relationships could be applied to improvements in statistical intensity forecast models (Jones et al. 2006; Kieper and Jiang 2012; Rozoff et al. 2012).

This thesis will address the relationship between TC precipitation properties and intensity change in the context of Hurricane Earl — one of the best-sampled cases of rapid intensification during the 2010 tri-agency field programs, and indeed, one of the best sampled in history. Rapid intensification (RI) is defined, following Kaplan and DeMaria (2003), as an intensification rate of at least 15 m s^{-1} (30 kt) per 24 hours. Earl also represents a prime example of a poorly forecast rapid change in TC strength. The NHC forecast issued near the onset of the RI (Table 1) significantly under-forecast the rate at which Earl strengthened, and by the end of the RI, the 36-hour NHC forecast maximum surface wind speed was 35 kt weaker than the observed maximum wind.

Using a combination of global analysis fields, satellite infrared and passive microwave data, in-situ aircraft measurements, lightning data, and dual-Doppler wind retrievals, this study will document the environmental conditions, precipitation characteristics, and kinematic structure of Earl before RI onset, during RI, and immediately after the end of RI. This documentation will allow for an investigation of the possible causes of the RI of Earl, with a focus on the following questions:

- What is the role of large-scale environmental conditions in the RI of Earl?
- Which core precipitation features appear to serve as necessary and/or sufficient conditions for RI? Symmetric precipitation rings, persistent intense 'convective bursts,' individual strong convective 'towers,' or something else?
- What is the importance of the radial distribution of convection relative to the RMW?

The remaining chapters are organized as follows: Chapter 2 provides a review of relevant literature. Chapter 3 describes the radar, satellite, lightning, global analysis, and aircraft in-situ datasets used to illustrate the time evolution of Hurricane Earl. Chapter 4 summarizes the large-scale environmental conditions. Chapter 5 describes the evolution of convective intensity, frequency and coverage of intense convection, precipitation coverage, precipitation symmetry, and the radial distribution of convection. Chapter 5 also examines in greater depth the interaction between the environmental shear, mesoscale vortex structure, and core convection immediately before the onset of RI.

Chapter 6 discusses the results in the previous chapters and ends with some concluding remarks and recommendations for future TC research.

Table 1. Comparison of NHC Best Track with NHC forecast at 0900 UTC August 29 [NHC forecast available online at http://www.nhc.noaa.gov/archive/2010/al07/al072010.discus.016.shtml].

Forecast Hour	Valid Time	Latitude	Longitude	Forecast Wind	Best Track Wind
INITIAL	08/29/0900Z	16.9N	56.9W	55 KT	--
12HR	08/29/1800Z	17.3N	59.1W	65 KT	75 KT
24HR	08/30/0600Z	17.9N	61.4W	70 KT	95KT
36HR	08/30/1800Z	18.7N	63.6W	80 KT	115KT
48HR	08/31/0600Z	19.9N	65.4W	90 KT	115KT
72HR	09/01/0600Z	23.5N	69.0W	100 KT	105KT
96HR	09/02/0600Z	29.0N	72.0W	105 KT	125KT
120HR	09/03/0600Z	34.5N	72.0W	105 KT	85KT

CHAPTER 2

LITERATURE REVIEW

2.1. Impact of Large-Scale Environmental Conditions

The following large-scale environmental conditions support TC intensification: low shear, high sea surface temperatures (SSTs), and high low-to-midlevel relative humidity. Warm sea surface temperatures are necessary for the development of strong hurricanes, and the sea surface temperature determines the maximum intensity that a TC can reach given favorable atmospheric conditions (Merrill 1988; DeMaria and Kaplan 1994). The entrainment of dry air at low or midlevels can weaken TCs (Dunion and Velden 2004), so higher environmental relative humidity is preferred for intensifying TCs (DeMaria et al. 2005).

The importance of vertical shear stems from the weakening effects that high vertical shear can have on tropical cyclones. Shear induces several processes that can act to weaken TCs, including tilting of the vortex (Reasor et al. 2013; DeMaria 1996; Jones 1995), and enabling ventilation of the warm core both at upper-levels (Frank and Ritchie 2001) and mid-to-lower-levels (Riemer 2010; Didlake and Houze 2013). Which mechanisms have the greatest influence on TC intensity is not known, but the link between deep-layer shear and weakening is well established, and several studies show that real tropical cyclones tend to weaken in the presence of vertical shear approaching or exceeding ~10 m s^{-1} (Chan and Kepert 2010; Gallina and Velden 2002).

Knowledge of the effects of large-scale environmental conditions is codified in the Statistical Hurricane Intensity Prediction Scheme (SHIPS; DeMaria et al. 2005) and Rapid Intensification Index (SHIPS-RII; Kaplan et al. 2010) models, and both the SHIPS and SHIPS-RII include these environmental factors as 'predictors' of future hurricane intensity and the probability of RI, respectively. Some of the lack of intensity forecast improvement might stem from the inability of current SHIPS and RII parameters to account for the nuances of different scenarios associated with high shear. For example, some storms intensify in the presence of high shear when that shear is associated with an upper-level trough and the TC is located in a region of favorable synoptic forcing from the trough (Molinari et al. 2006). The interaction between different environmental conditions might also be an important factor determining the environmental effects on intensity. Both modeling (Riemer et al. 2010) and observational studies (Didlake and Houze 2013) suggest that vertical shear enables ventilation of the warm core with midlevel environmental air, so the environmental humidity might become more important in moderate to high shear environments. Together these research results suggest that for storms that exist in a combination of favorable and unfavorable environmental conditions (e.g., high shear and high SST), a better assessment of the nuances of the environmental conditions and their interactions with each other might lead to better forecasts.

However, an improved assessment of the environmental conditions might not improve forecasting of RI. Hendricks et al. (2010) showed that environmental conditions are quite similar for intensifying and rapidly intensifying storms, suggesting that given favorable environmental conditions, TC internal processes are the main controller of the rate of intensification. This indicates that a better understanding of the relationship between TC internal conditions and intensification is necessary for improved intensity forecasts, especially in the context of anticipating RI events.

2.2. Precipitation Characteristics and Tropical Cyclone Intensity Change

Several studies have statistically linked intense convection to TC intensification. The multistorm satellite results of Steranka et al. (1986) and Hennon (2006) suggest that episodes of intense core convection that persist for several hours tend to precede TC intensification. On the smaller scale of individual convective cells, Kelley et al. (2004) and Jiang (2012) showed that TCs with extremely tall inner-core radar echoes have a higher probability of intensification and RI than storms without these tall convective cells. Case studies have also described many events in which intense inner-core convection appears to lead to TC intensification. The observational studies of Heymsfield et al. (2001) and Guimond et al. (2010) as well as the simulation results of Chen and Zhang (2013) suggest that descent and adiabatic warming forced by intense (~10 m s^{-1} or stronger updrafts) convection can cause significant warming in the hurricane eye. Nguyen et al. (2008) noted local vorticity anomalies associated with convective updrafts in an idealized TC simulation, and concluded that rotating convective updrafts, or 'vortical hot towers,' are the main convective features responsible for TC intensification. Houze et al. (2009) observed deep, rotating convection in a developing tropical depression, and Sanger et al. (2014) found some observational evidence of 'vortical' towers in an intensifying tropical storm.

Although intense convection might contribute to RI or even cause it in some cases, the results of Jiang and Ramirez (2013) show that the necessary inner-core convective conditions for RI are actually rather modest: RI events require the existence of 40 dBZ echoes reaching > 4 km altitude, 20 dBZ echoes > 8 km, and infrared (IR) brightness temperatures < 220 K. In other words, convection must exist, but it need not be intense. Jiang and Ramirez (2013) also found that the raining area and volumetric rain tend to be higher for RI events than for other intensity change categories, and raining area and volumetric rain of 3000 km^2 and 5000 mm hr^{-1} km^2 are necessary for RI, indicating that rainfall coverage is a more important indicator of RI than convective intensity.

The importance of precipitation coverage may reflect the role of increased precipitation symmetry in intensifying storms. The importance of precipitation symmetry is supported by the findings of Rogers et al. (2013a), who showed that relative to steady-state TCs (intensity change within ±10 kt $(24hr)^{-1}$), intensifying TCs ($\geq \pm 20$ kt $(24hr)^{-1}$) contained greater azimuthal rainfall coverage in both the eyewall and outer core regions. Precipitation symmetry might also serve as a sufficient condition for RI, as the appearance of an axisymmetric precipitation ring often precedes RI (Willoughby 1990; Harnos and Nesbitt 2011; Kieper and Jiang 2012), especially in the presence of favorable environmental conditions (Harnos and Nesbitt 2011; Kieper and Jiang 2012). Kieper and Jiang (2012) showed that convection in this ring does not have to be intense, and in many cases the precipitation ring can even be composed entirely of warm rain and shallow convection before the onset of RI. The observational findings about precipitation symmetry support the notion that axisymmetric convective heating has a much greater influence on TC intensity than asymmetric forcing (Nolan et al. 2007).

Inner-core convection occurs in the context of the powerful TC primary and secondary circulations, and the radial location of a latent heat source relative to that circulation might determine the degree to which that heating leads to TC intensification. In idealized axisymmetric model experiments, the wind speed increase relative to the heating magnitude increases with decreasing radius (Schubert and Hack 1982; Pendergrass and Willoughby 2009), with the highest heating efficiencies inside the radius of maximum wind (RMW; Pendergrass and Willoughby 2009; Vigh and Schubert 2009). Rogers et al. (2013a) showed that strong convective updrafts tend to be located within the RMW in intensifying TCs and outside of the RMW in steady-state TCs, indicating that convective contributions to TC intensification are enhanced within the RMWs of real storms.

The interaction between the environmental conditions and TC-core precipitation systems must be considered along with the core precipitation characteristics. While intensification and RI appear to proceed via heating from axisymmetric convective rings in low-shear environments, studies of RI in higher shear environments suggest that convective intensity is a more useful indicator of RI in sheared storms (Harnos and Nesbitt 2011; Molinari and Vollaro 2010; Nguyen and Molinari 2012). Highly sheared storms often cannot form axisymmetric precipitation rings, so in the absence of a symmetric heat source, the vorticity and heat contributions from intense convection might become necessary for intensification.

CHAPTER 3

DATA AND METHODS

3.1. Hurricane Earl

Figure 1, Figure 2, and Figure 3 show the NHC Best Track track and intensity of Earl (tropical cyclone report; Cangiolosi 2011). Earl developed from an African easterly wave that entered the Atlantic Ocean on 23 August 2010, reaching tropical storm strength by 2100 UTC August 25. From August 26 through August 28, Earl tracked westward across the tropical Central Atlantic and slowly strengthened. Then, between 0600 UTC August 29 and 1800 UTC August 30, Earl underwent RI from a 55-kt tropical storm to a 115-kt hurricane.

This study focuses primarily on the periods before, during, and immediately after Earl's rapid intensification (RI). Earl was sampled by the National Oceanic and Atmospheric Administration (NOAA) WP-3D (P3) and Gulfstream IV (GIV) aircraft as part of the ongoing NOAA Intensity Forecasting Experiment (IFEX, Rogers et al. 2013b), and by the National Aeronautics and Space Administration (NASA) DC-8 aircraft as part of the Genesis and Rapid Intensification Processes campaign (GRIP, Braun et al. 2013). The Air Force WC-130J (C130) aircraft also flew frequent reconnaissance flights into Earl, with the first flight soon after the onset of RI. The combination of NOAA, NASA, and Air Force observations make Earl one of the best-observed cases of RI ever. In this case study, field campaign data from the NOAA and Air Force aircraft are combined with satellite observations, lightning data, and large-scale analysis fields for the purpose of studying the precipitation characteristics and kinematic structure before, during, and immediately after the RI of Earl.

3.2. Global Atmospheric and SST Analyses

The National Centers for Environmental Prediction (NCEP) Final (FNL) Operational Global Tropospheric Analysis (http://rda.ucar.edu/datasets/ds083.2/) wind and humidity fields are utilized for an assessment of the large-scale atmospheric conditions affecting Earl. The FNL analyses contain wind fields at 26 pressure levels between 1000–10 mb. Humidity is stored at the same pressure levels as the wind data between 1000–100 mb, but no humidity fields exist at pressures lower than 100 mb. The horizontal resolution of data points is 1° latitude/longitude. The NCEP Global Data Assimilation System (GDAS) creates the FNL fields four times daily, with analyses valid at the synoptic times of 0000, 0600, 1200, and 1800 UTC.

Atmospheric environmental parameters are calculated from the NCEP FNL analyses. For both the shear and relative humidity (RH), values are calculated within an annulus between 1.8–7.2 degrees from the Best Track center. To calculate vertical shear, the vector average horizontal wind components are calculated separately at a lower level and an upper level. The shear magnitude and direction are then computed from the vector difference between the average wind vector at the lower and higher pressure-levels.

SST data are taken from the NCEP Real Time Global (RTG) SST Analyses (http://polar.ncep.noaa.gov/sst/rtg_high_res/). NCEP produces these analyses once daily by interpolating 24 hours of buoy, ship, and satellite SST data to a 1/12°- resolution grid.

3.3. GOES Infrared Brightness Temperatures

The strength of the IR observations lies in the high spatial and temporal resolution of geostationary satellite (GOES) data. The gridded IR dataset used here has a temporal resolution of 30 minutes and a horizontal resolution of 3 km. With this high-temporal resolution data, an hourly time series of GOES IR fractional coverage of relatively high cloud tops (for 213, 203 and 193 K brightness temperatures) within 200 km of Earl's center is constructed.

Out of all the remote sensing platforms used here, infrared (IR) data provides the least amount of objective information about TC-core precipitation characteristics. While cold brightness temperatures can indicate the presence of deep convection, similar cold temperatures can also be associated with high anvil clouds, even after convection has dissipated beneath them. Therefore, an accurate description of TC precipitation characteristics must include data from other platforms such as passive microwave and radar instruments.

3.4. Passive Microwave Satellite Data

Satellite passive microwave (PMW) measurements have a lower spatial and temporal resolution than GOES data. PMW radiometers are on low altitude earth-orbiting satellites, so the temporal frequency for measurements of Earl is typically a few hours. However, unlike IR observations, PMW data can provide relatively unambiguous information about convective intensity and precipitation coverage.

Special Sensor Microwave Imager/Sounder (SSMI(S)) brightness temperatures are taken from the Defense Satellite Meteorological Program (DMSP) F15, F16, F17, and F18 satellites. The SSMI(S) measurements are from the Fundamental Climate Data

Record (FCDR; Sapiano et al. 2013) of intercalibrated microwave imager brightness temperatures. Tropical Rainfall Measuring Mission (TRMM) Microwave Imager (TMI) level-1 calibrated data are taken from the University of Utah Precipitation Feature Database (Liu et al. 2008). Brightness temperatures from the Advanced Microwave Scanning Radiometer Earth Observing System (AMSRE) are obtained from the from the National Snow and Ice Data Center (NSIDC) AMSR-E/Aqua Global Swath Brightness Temperatures dataset (Ashcroft and Wentz 2013). Images of 89 GHz brightness temperatures from the Advanced Microwave Sounder Unit - B (AMSU-B) are obtained from the University of Wisconsin Cooperative Institute for Meteorological Satellite Studies (UW-CIMSS) AMSU homepage (http://tropic.ssec.wisc.edu/real-time/amsu/) and the Naval Research Laboratory (NRL) TC page (http://www.nrlmry.navy.mil/TC.html), and an image of the TRMM TMI 37 GHz color composite is also obtained from the NRL TC page.

Each of these datasets contains brightness temperatures between 85–91 GHz. The AMSRE, TMI, and SSMI(S) scan conically and measure brightness temperature in this channel at both vertical and horizontal polarizations. The AMSU-B is a cross-track scanning instrument, so the polarization of the data varies along with the scan angle. Although the exact center frequency of the channel varies between instruments (85 GHz for TMI and SSMI, 89 GHz for AMSRE, 91 GHz for SSMIS), PMW observations between 85–91 GHz respond very similarly to atmospheric features. The 85–91 GHz brightness temperatures are depressed over frozen and mixed-phase precipitating regions due to scattering from frozen precipitation. Brightness temperatures are also depressed in regions of dry air over oceans and lakes because of low water surface emissivity at 85–91

GHz. Land emissivity is high at these frequencies, so brightness temperatures are elevated over landmasses.

Unfortunately, the combination of scattering and absorption effects in 85–91 GHz data creates ambiguities in interpretation of these measurements, and over the ocean it is difficult to objectively distinguish regions of dry clear air from regions of cold-cloud precipitation, since both can result in similar brightness temperatures. Spencer et al. (1989) resolved this ambiguity by defining ‘polarization corrected temperature’ (PCT) as a linear combination of the horizontally (TB_H) and vertically (TB_V) polarized brightness temperatures.

$$\mathrm{PCT} = 1.818(\mathrm{TB_H}) - 0.818(\mathrm{TB_V}) \qquad \text{(eq. 1)}$$

Water surfaces appear colder for TB_H than for TB_V, so by weighting towards TB_H, equation 1 removes the contrast in brightness temperature over land versus ocean surfaces. The ice-scattering signals are retained, so the depression of PCT is directly related to the vertically integrated ice water path, and hence to convective intensity (Spencer et al. 1989; Vivekanandan et al. 1991).

The spatial resolution of 85–91 GHz measurements varies between instruments — the SSMI and SSMIS have a resolution of 12.5 km, while the TMI and AMSRE have a spatial resolution of approximately 6 km. The cross-track-scanning AMSU-B has a spatial resolution of 16 km at nadir, with spatial resolution decreasing to near 36 km at the limbs of the swaths (Vila et al. 2007). For the higher-resolution polarized data (SSMI(S), TMI, AMSRE), the spatial resolution allows for the identification of precipitation features such as eyewalls, rainbands, and clusters of convective cells.

Using 85–91 GHz PCTs from the AMSRE, TMI, and SSMI(S) instruments, time series of the following inner-core (within 100 km from center) precipitation parameters are constructed: minimum 85–91 GHz PCT, mean PCT, and fractional areas of PCT ≤250 K and PCT≤200 K. Only overpasses with complete or nearly complete inner-core data coverage are included. The minimum PCT provides a rough estimate of the maximum convective intensity (Liu et. al, 2011). Generally, PCTs ≤250 K correspond to at least moderate rainfall rates (Spencer et al. 1989), while PCTs ≤200 K represent more-intense convection (Cecil and Zipser 1999). The mean PCT serves as a combined estimate of both deep precipitation coverage and convective strength.

To generate a time-radius cross-section of PCT, data are sorted into overlapping radial bins. TRMM TMI and AMSRE data are sorted into 10 km wide overlapping radial bins (0–10 km, 5–15 km, 10–20 km, etc.), while SSMI(S) data are sorted into 20 km wide bins (10–30 km, 20–40 km, etc.). The use of overlapping bins allows for radial grid steps that are smaller than the actual footprint size of the microwave measurements. Once the data are sorted into radial bins, the average PCT in each bin is calculated. With the exception of two overpasses, most PMW passes contain complete (100%) data coverage inside 150 km; for the two that do not, the bin-average PCTs are not computed beyond 100 km.

3.5. NOAA P3 In Situ and Radar Data

Figure 4 shows the timing of the NOAA P3 flights during the time period of interest. The P3 flew once before the onset of RI, three times during the RI, and once a few hours after the end of RI. Flights are named according to the date, and a letter, ‘I,’ or ‘H,’ indicating the aircraft (N43F and N42F, respectively). The P3s record flight-level horizontal and vertical wind using the aircraft's onboard inertial navigation systems. The NOAA Aircraft Operations Center quality controls the flight-level data, and provides 1-Hz wind data on the NOAA Hurricane Research Division (HRD) website (http://www.aoml.noaa.gov/hrd/data_sub/hurr.html).

The NOAA P3s are also equipped with vertically scanning 3.22 cm wavelength Doppler radars on the tail end of each aircraft (Tail Doppler Radars, or TDRs). The TDRs employ a 'fore-aft' scanning strategy, or FAST (Gamache et al. 1995), in which the radar alternates between fore and aft scans as the aircraft moves through the storm. FAST scanning results in nearly simultaneous measurements of two components of the wind, with the horizontal spacing of these measurements dependent on how frequently the radar shifts between the fore and aft scans. In the case of the NOAA P3, the along track resolution is approximately 1.4 km (Houze et al. 2005). Retrievals of the full three-dimensional wind field can be obtained from the TDR pseudo-dual-Doppler measurements through solution of the continuity equation.

The HRD performs an automated quality control and Doppler retrieval on the TDR observations from NOAA P3 flights into TCs (Gamache et al. 2008). The automated quality control removes errors from sea-surface reflection and samples with low signal-to-noise ratio, unfolds the radial velocities, and subtracts aircraft motion and hydrometeor fall speeds from the radial winds. The HRD analysis program then retrieves the three-dimensional wind using the variational scheme described in Reasor et al. (2009), and creates a reflectivity analysis with the same spatial resolution as the wind retrieval. The P3 flies successive radial passes when sampling developed TCs, and the HRD software produces a separate analysis for each of these radial transects. The analyses are produced in real-time at a horizontal and vertical resolution of 5 km and 0.5 km, respectively.

The HRD also produces higher resolution (2 km horizontal, 0.5 km vertical) wind and reflectivity analyses with experimentally modified versions of the analysis software (Rogers 2012, personal communication), and these experimental, high-resolution 'TDR analyses' are used here. For these experimental analyses, the lowest level is sea level and the highest level is 18 km. The quality control of the TDR data is less strict for these high-resolution analyses, so sometimes HRD scientists manually edit the resulting analysis fields. HRD scientists also noted calibration differences between the two TDRs, and following the recommendation of P. Reasor (2012, personal communication), 7 dBZ has been added to the reflectivity analyses from the N43F TDR ('I' flights, Figure 4) to correct this calibration inconsistency.

Figure 5 shows an example of a TDR analysis. The TDR analyses can depict the convective-scale structure of the wind and reflectivity fields, but the TDR data coverage is limited by attenuation, radar sensitivity, and ultimately by the maximum unambiguous range of the TDR (~60–70 km in Earl); thus, the analysis coverage is confined to areas near the P3 flight track. This lack of analysis coverage is partially remedied by compositing the TDR analyses for a given flight, creating higher-coverage 'merged' analyses for each P3 flight. Although compositing results in a loss of effective resolution, the merged analyses can still effectively illustrate mesoscale structures that remain mostly unchanged over 3–6 hours. Relatively slowly-evolving aspects of Earl's structure, such as the azimuthally averaged primary and secondary circulations and some aspects of the mesoscale structure of the wind and precipitation fields, are examined with the merged analyses. Quickly-evolving convective-scale features are studied with the TDR analyses.

Azimuthally averaged winds and reflectivities are calculated from the merged analyses. Azimuthally averaged values are only calculated in regions that meet the following azimuthal data coverage thresholds: at a given radius and any altitude above sea level, the total azimuthal data coverage must be ≥40%, and the azimuthal data coverage in each quadrant must be >10%.

The radius of maximum tangential wind (RMW) is calculated from the azimuthally averaged winds. The RMWs at 2 km ('2-km RMW') and 8 km ('8-km RMW') altitude are then interpolated between P3 flights to create hourly RMW locations at those altitudes. Low azimuthal data coverage prevents calculation of the 8-km RMW from the 828I flight, so the 8-km RMW is only interpolated for times between 6–40 hours after the onset of RI. These RMW locations are created for the purpose of exploring the relationship between other convective proxies (such as passive microwave PCT and lightning) and the RMW.

'Strong updraft' locations are defined as TDR analysis grid points with 8-km vertical velocity greater than 5.5 m s^{-1}, since 8-km vertical velocities above this threshold represent the 99th percentile of 8-km vertical velocity in the HRD TDR analysis dataset (Rogers et al. 2013a). Strong updraft grid counts and locations are calculated separately for each P3 flight. For a given flight, any single storm-relative grid location with a strong updraft will only count as one strong updraft grid, even if the P3 retrieved velocities show strong updrafts at that location in more than one TDR analysis. This is done in an attempt to avoid potential biases towards high strong updraft counts in regions that are sampled in more than one P3 transect.

3.6. WWLLN

The World Wide Lightning Location Network (WWLLN; Rodger et al. 2006) is a network of approximately 60 ground observation stations that detect very low frequency (VLF) radiation from lightning strikes. WWLLN detection efficiency varies strongly with the peak current of lightning strikes, with much higher detection efficiencies for stronger currents. Due to this bias towards stronger currents, WWLLN favors detection of cloud to ground (CG) lightning. The WWLLN reporting technique ensures that the location accuracy is ~10 km (Holzworth 2014, personal communication), and recent validation efforts (Abarca et al. 2010; Hutchins et al. 2012) indicate that WWLLN had CG detection efficiency of 10–15% in the vicinity of Hurricane Earl. These validation results also strongly suggest that the location accuracy was ~5 km for the northern Caribbean and nearby Atlantic Ocean regions during the lifetime of Hurricane Earl.

Electrification of convective cells requires much stronger updrafts than what is typically observed in tropical maritime convection (Black and Hallett 1999; Reinhart et al. 2014), so lightning can serve as a proxy for intense convective activity in tropical cyclones. Abarca et al. (2011) showed that despite its low detection efficiencies, WWLLN accurately captures the mesoscale spatial structure of lightning within TCs, so WWLLN data can serve as a useful indication of the frequency and spatial distribution of very intense convection in Earl. For Earl, WWLLN also represents the only data source that can indicate the spatial and temporal evolution of intense convection on a time scale of an hour or less, compared with several hours or more from PMW observations and TDR analyses. Time series and Hovmoller plots of lightning are created here for that purpose, and maps of lightning locations are also examined.

3.7. Center Fixes

The NHC Best Track TC positions only exist at synoptic times and the Best Track data are spatially smoothed, so interpolating between Best Track positions can lead to erroneous TC position estimates. Environmental conditions are calculated over a large spatial region, so highly accurate TC centers are not necessary for those parameters. On the other hand, the NHC Best Track is not a good dataset to utilize for studying TC-core convective characteristics, so a separate dataset of hourly TC center position and motion estimates is created from the NHC advisory fixes for that purpose. First, several of the NHC advisory positions are manually modified to decrease the difference between the advisory fixes and the vortex center locations depicted in available NOAA and Air Force flight-level data, PMW images, and TDR analyses. Then, hourly TC locations and motion estimates are calculated by interpolating between the partially modified NHC advisory positions. This set of center-fix and motion estimates will be referred to as the ‘hourly center-fix’ data or HCF.

3.8. Variational Mesoscale Anaylses

While the merged TDR analyses provide good coverage of the lower and mid-tropospheric winds in the inner-core of Earl, large gaps remain in the merged analysis wind fields, especially in the upper troposphere and in the outer-core regions of the tropical cyclone. For the purpose of obtaining information about the mesoscale characteristics of Earl’s wind field in these regions, mesoscale three-dimensional variational wind analyses are constructed from the TDR radial velocities and the 1-Hz P3 flight-level horizontal wind data.

The quality controlled (Gamache et al. 2008) TDR radial velocities and the flight-level horizontal winds are renavigated to a common time that represents the middle of the period during which the P3 flight flew in Earl. The winds are then retrieved with the variational analysis program developed by C. Lopez Carrillo and D. Raymond at the New Mexico Institute of Mining and Technology (Lopez Carrillo and Raymond 2011). As with the TDR merged analyses, the analyses are named according to the P3 flight (828I, 829H, etc.).

These variational ('NMT-3dvar') analyses have a horizontal resolution of 0.1° and a vertical resolution of 0.5 km, with the bottom of the grid at sea level and the top at 17 km. The horizontal resolution obscures many of the features seen in the TDR merged analyses, but it allows the analysis to cover a larger area. The use of a larger grid volume also allows the variational analysis software to obtain sufficient Doppler samples in regions of low Doppler data density. In regions without Doppler or flight-level data, the program estimates the wind through the continuity constraint and horizontal smoothing terms of the analysis scheme (Lopez Carrillo and Raymond, 2011).

3.9. What Is a Convective Burst?

There are many different definitions of 'convective bursts' in TC literature (Steranka et al. 1986; Hennon 2006; Rogers et al. 2013a). Unfortunately, these different definitions can lead to confusion, since some definitions refer to periods of intense convection on the meso-β spatial scale and temporal scales of several hours or more (Steranka et al. 1986; Hennon 2006), while others describe individual vigorous convective-scale features (Guimond et al. 2010; Rogers et al. 2013a). Hereafter, this thesis will use a vortex-scale definition of a convective burst as a period of persistent, intense inner-core convection on a temporal scale of several hours and on a spatial scale of the TC inner-core.

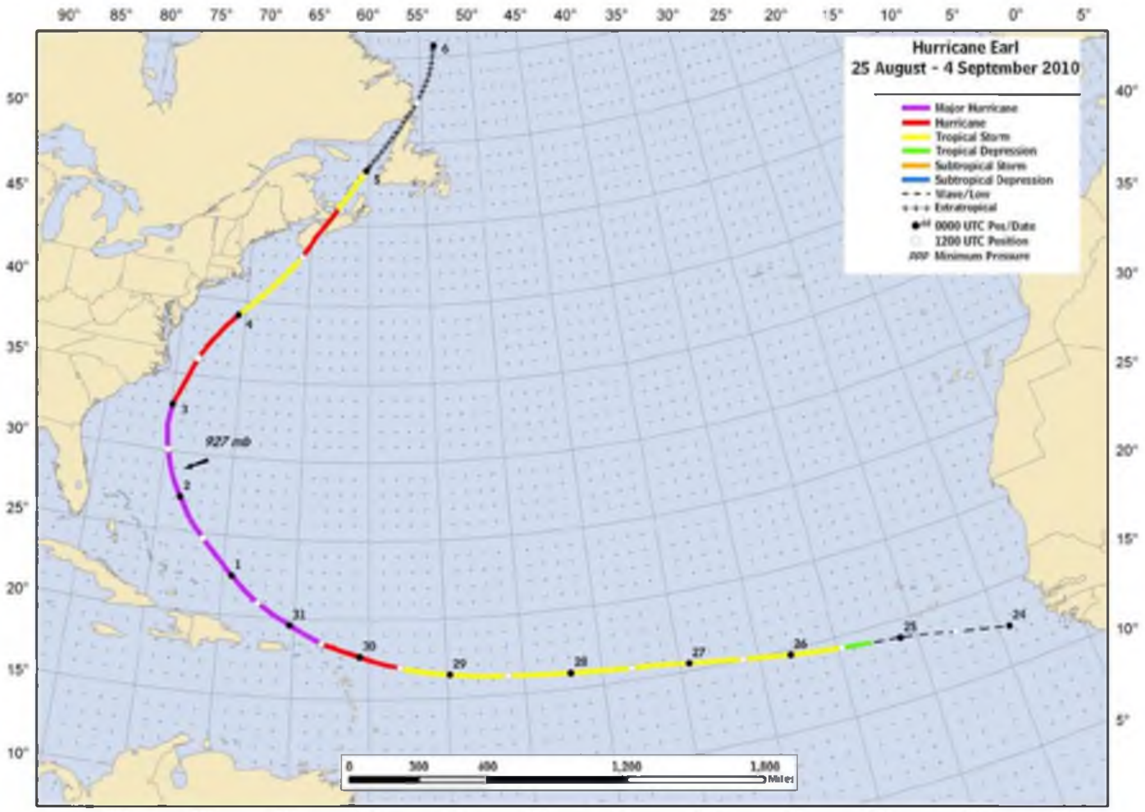
Hurricane Earl
25 August - 4 September 2010
Major Hurricane
Hurricane
Tropical Storm
Tropical Depression
Subtropical Storm
Subtropical Depression
Wave/Low
Extratropical
0000 UTC Pos/Date
1200 UTC Position
### Minimum Pressure
927 mb
24
25
26
27
28
29
30
31
1
2
3
4
5
6
0
300
600
1,200
1,800
Miles
90°
85°
80°
75°
70°
65°
60°
55°
50°
45°
40°
35°
30°
25°
20°
15°
10°
5°
0°
5°
50°
45°
40°
35°
30°
25°
20°
15°
10°
40°
35°
30°
25°
20°
15°
10°
5°
75°
70°
65°
60°
55°
50°
45°
40°
35°
30°
25°
20°

Figure 1. NHC best-track track of Hurricane Earl. Reprinted, with permission of NOAA, from Cangiolosi (2011) “Tropical cyclone report hurricane Earl (AL072010).”

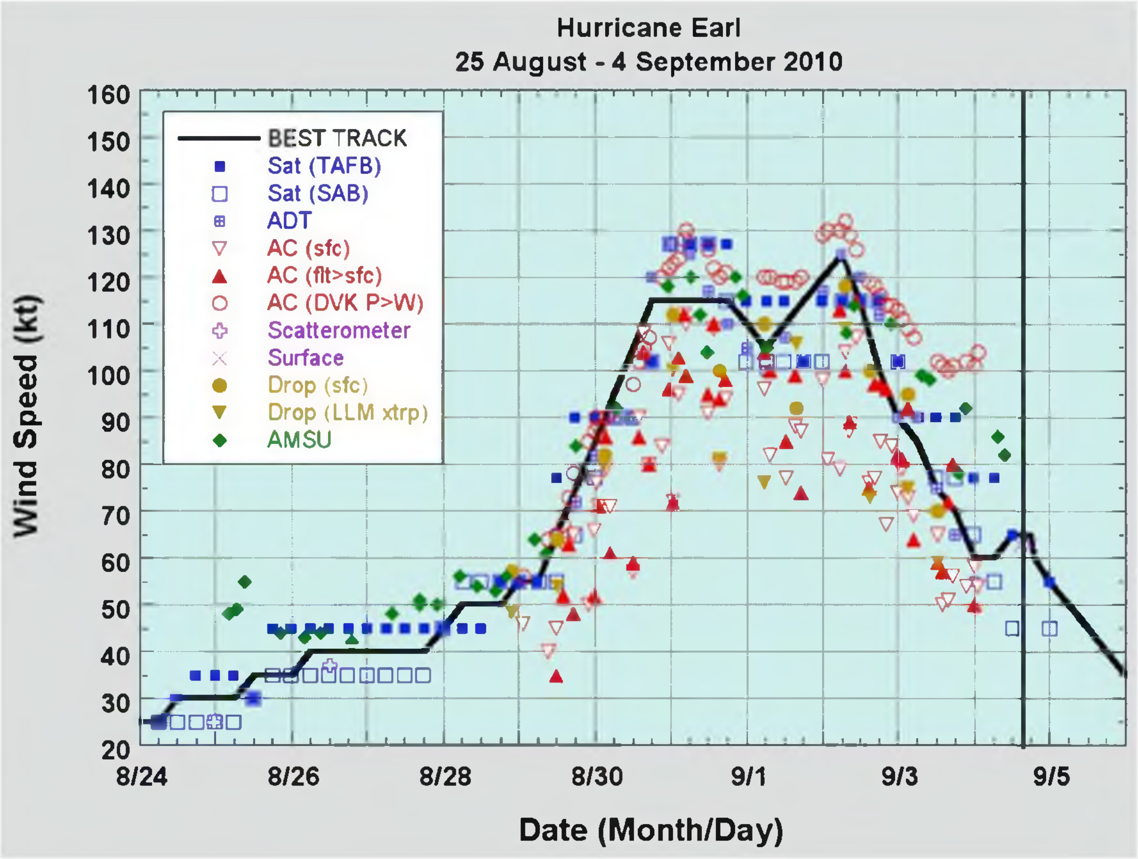

Figure 2. Hurricane Earl NHC Best Track maximum surface wind speed. Reprinted, with permission of NOAA, from Cangiolosi (2011) "Tropical cyclone report hurricane Earl (AL072010)."

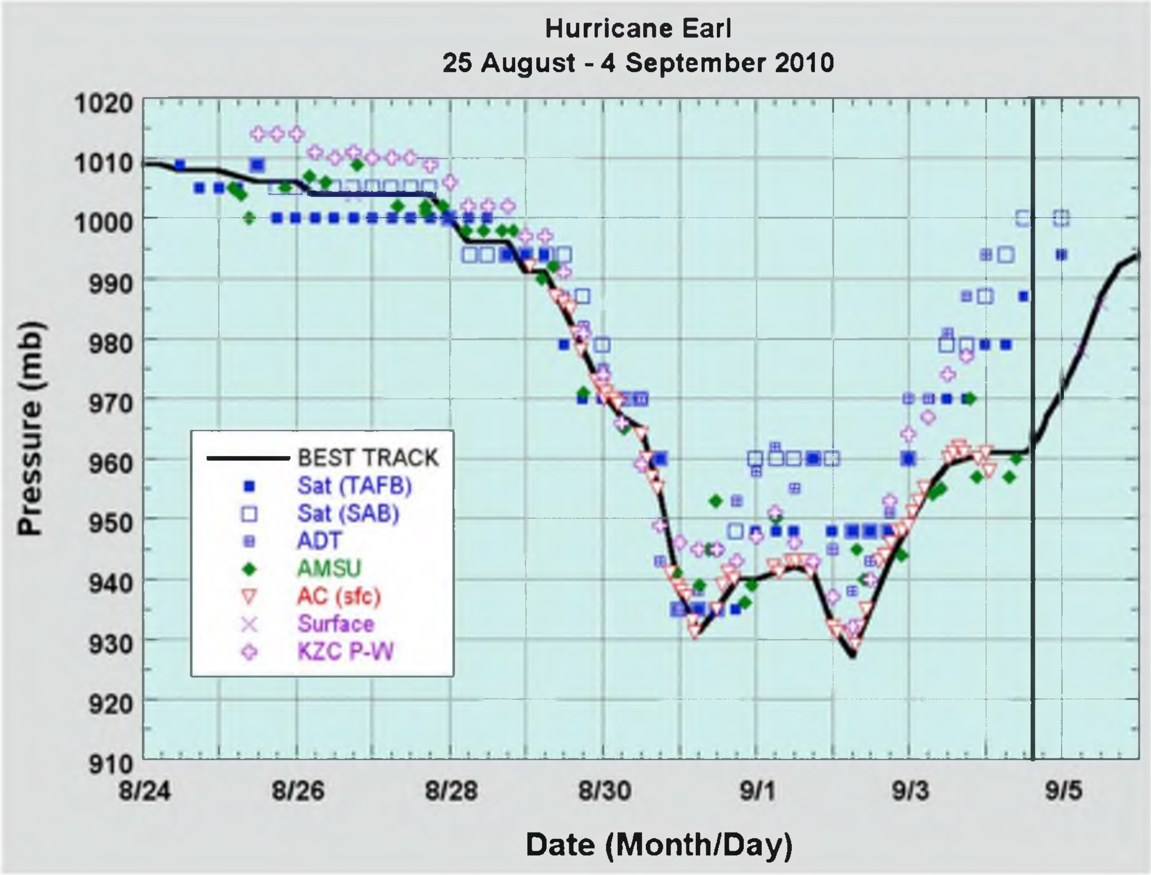

Figure 3. NHC Best Track minimum MSLP for Hurricane Earl. Reprinted, with permission of NOAA, from Cangiolosi (2011) "Tropical cyclone report hurricane Earl (AL072010)."

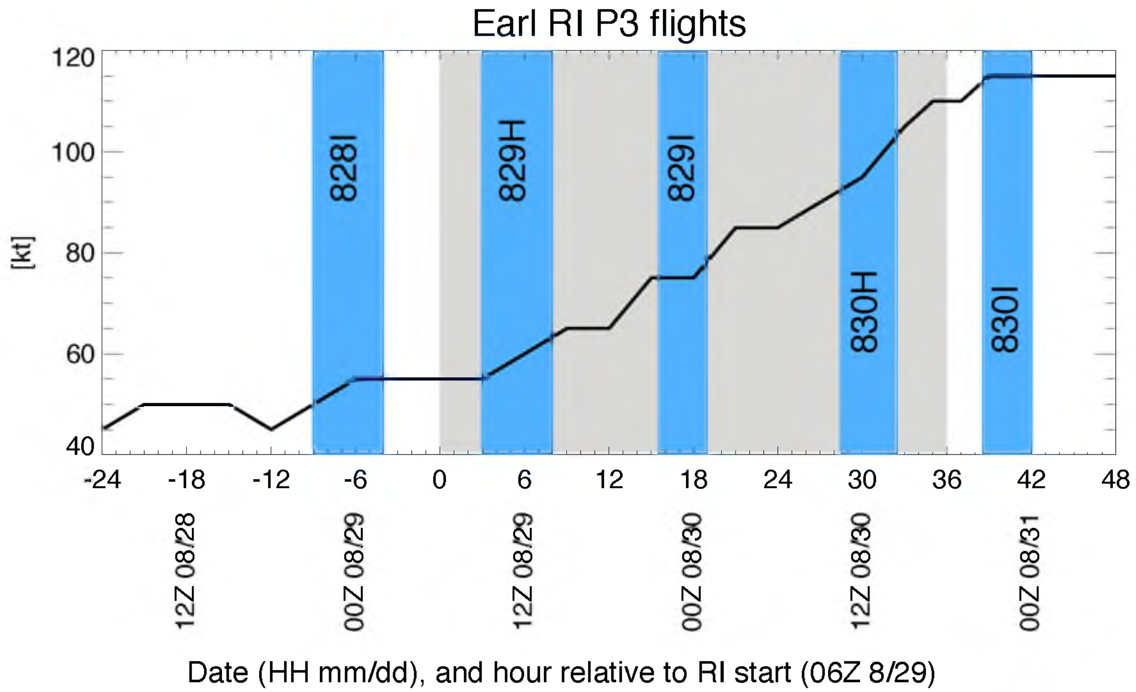

Figure 4. Timing of NOAA P3 flights into Earl and NHC Advisory maximum surface winds. Shaded regions indicate approximate times during which the P3 TDR collected data in Earl. Grey shading indicates the 36-hour RI period.

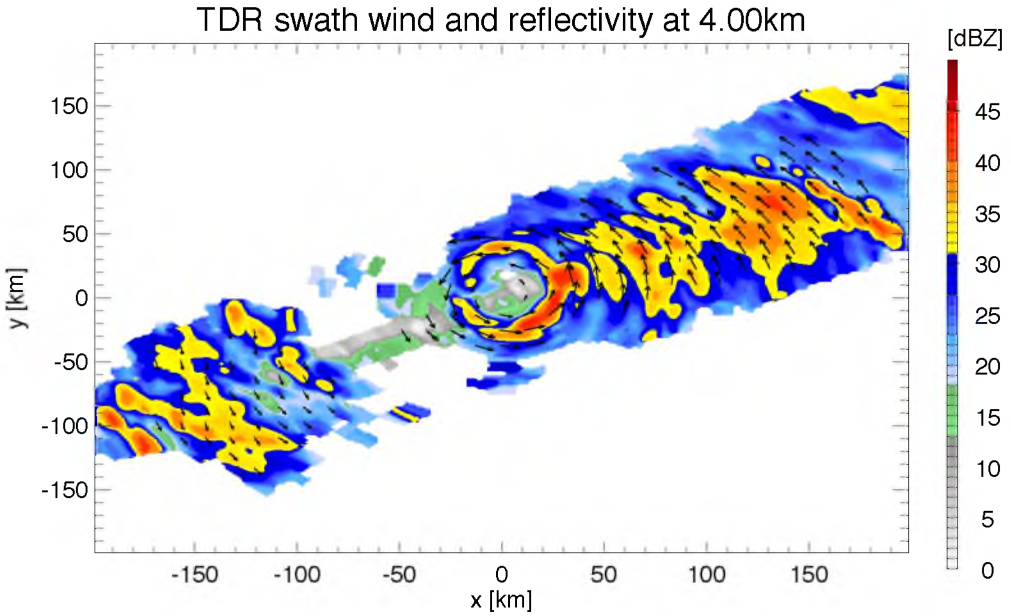

Figure 5. Example of a TDR analysis: reflectivity and horizontal wind vectors for P3 transect at 1222 UTC August 30.

CHAPTER 4

LARGE-SCALE ENVIRONMENTAL CONDITIONS

Figure 6 shows a time series of NCEP RTG analysis SSTs beneath Earl. The SSTs beneath Earl are at levels that favor rapid intensification of Atlantic TCs (Kaplan and DeMaria 2003) as early as 30 hours before the onset of RI. Improving SST conditions may have played some role in the timing of the start of RI, as the SSTs increase by approximately 1°C between 12 hours before and 18 hours after the onset of RI. The SST decreases very slightly after the end of RI, so the near steady-state intensity after the end of Earl's RI was probably not caused by changes in SST. SHIPS Rapid Intensification Index (SHIPS-RII, Kaplan et al. 2010) messages 0–24 hours after the end of RI (not shown) have values of 'POT' (difference between storm strength and maximum potential intensity; Kaplan and DeMaria 2003) remaining between 37–40 kt, providing further indication that the end of RI was not caused by the coincident slight reduction in SST.

The low-level (850–700 mb), midlevel (650–400 mb), and upper-level (400–200 mb) layer-average RH is shown in Figure 7. Lower-tropospheric RH in the vicinity of Earl holds steady around 60% before the RI onset, during RI, and after the end of RI. Although this value of RH is below the mean for rapidly intensifying Atlantic storms (Kaplan and DeMaria 2003; Kaplan et al. 2010), it is still high enough to support RI. The upper-level RH increases after the start of rapid intensification, indicating that the upper-level RH is responding to the rapid intensification rather than causing it — the outflow cirrus deck expands to large radii as the storm strengthens, increasing the environmental RH at upper levels.

Low-to-midlevel (850–500 mb) and deep-layer (850–300 mb, 850–200 mb, and 850–150 mb) shear magnitudes are displayed in Figure 8 and deep-layer shear directions are shown in Figure 9. While the 850–300 mb shear remains below 6 m s^{-1} leading up to RI, the 850–200 mb and 850–150 mb shears increase to moderate levels (7–12 m s^{-1}) between 18 hours before and 12 hours after the onset of RI. These moderate levels of northeasterly (Figure 9) 850–200 mb and 850–150 mb shear are near the threshold levels at which several studies show a tendency for TC weakening (Chan and Kepert 2010). Deep-layer shear decreases by 18–24 hours after the onset of RI, and remains below ~6 m s^{-1} through the rest of the RI period. Deep-layer shear increases sharply in the 12 hours following the end of RI. However, because changes in TC strength tend to lag behind changes in shear (Gallina and Velden 2002), it is unlikely that this later increase in shear halted the RI of Earl.

While the later stages of Earl's RI may have been enhanced by a favorable decrease in environmental shear, the early stages of Earl's RI cannot easily be explained by changes in the shear. Instead, the existence of possibly detrimental levels of vertical shear before and during RI raises the question of how RI initiated in Earl despite this shear. A partial answer may lie in the level at which the shear occurred before the start of RI and during the early stages of the RI. As Figure 8 shows, between 18 hours before and 12 hours after the onset of RI, most of the shear occurred between the middle and upper troposphere, with very little vertical shear below 500 mb.

Figure 10 illustrates the evolution of upper-level winds in the western Atlantic region. Before the start of RI and at RI onset, an outflow channel from Hurricane Danielle appears to exert a northeasterly cross-storm flow near Earl's center (Figure 10a-b), indicating that this outflow jet was the source of the moderate mid-to-upper-level shear affecting Earl at that time. By 18 hours after the onset of RI, (Figure 10c), Earl has moved west of this region of shear, and Earl remains in a region of weak upper-level flow through the end of RI (Figure 10d).

Before the start of RI and during the early stages of RI, the lack of low-to-midlevel shear may have provided a relatively favorable environment, leaving the lower and midlevel portions of Earl's vortex relatively unaffected by shear and thereby allowing Earl to undergo RI despite the seemingly hostile environment. This would be consistent with the statistical modeling results of Rhome et al. (2006), which suggest that 850–500 mb environmental shear is a better predictor of hurricane intensity than the deep-layer shear parameter currently employed in the operational SHIPS model (DeMaria et al. 2005). On the other hand, the simulation results of Chen and Zhang (2013) showed the warm core of a simulated rapidly intensifying storm developing at upper-levels, thus they emphasized the role of upper-level winds in future TC strength. Ultimately, the role of the upper-level shear in Earl may have depended upon the level at which the heating occurred in Earl. The upper-level thermodynamics of Earl's inner-core were not sampled by any of the GRIP instruments before the onset of RI, so there are no reliable measurements of the upper-level portions of Earl's warm core before RI onset. On the other hand, the TDR wind measurements do extend to upper levels; therefor it *is* possible to observe the mid- and upper-level storm-relative flows in Earl's inner-core before RI onset. The effect of the large-scale shear on these inner-core storm-relative flows will be discussed in Chapter 5.

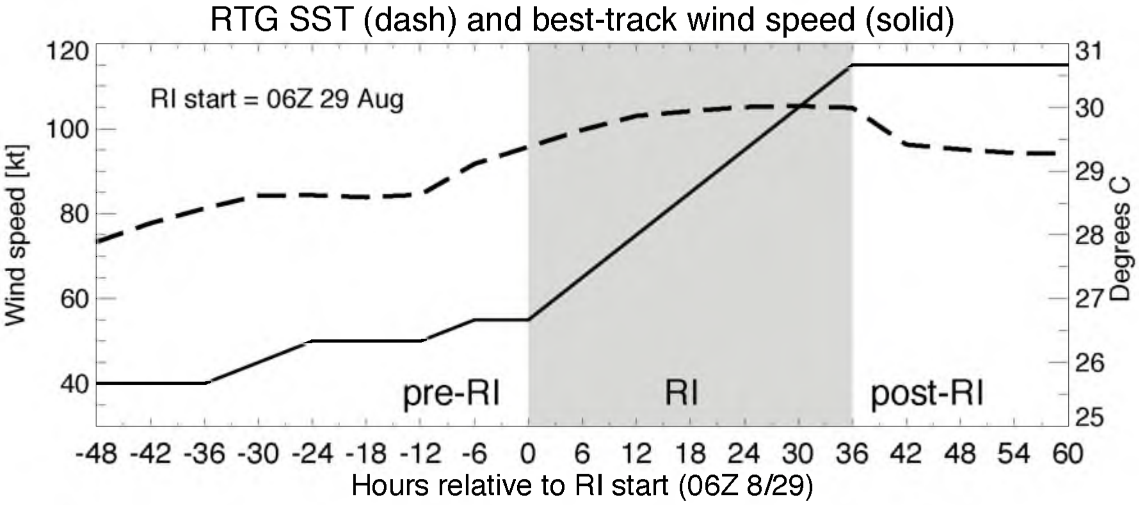

Figure 6. NCEP RTG analysis mean SST within 3 degrees lat/lon from Earl's Best Track center locations (dashed line), and NHC Best Track maximum wind speed (solid line). RI time period is grey-shaded.

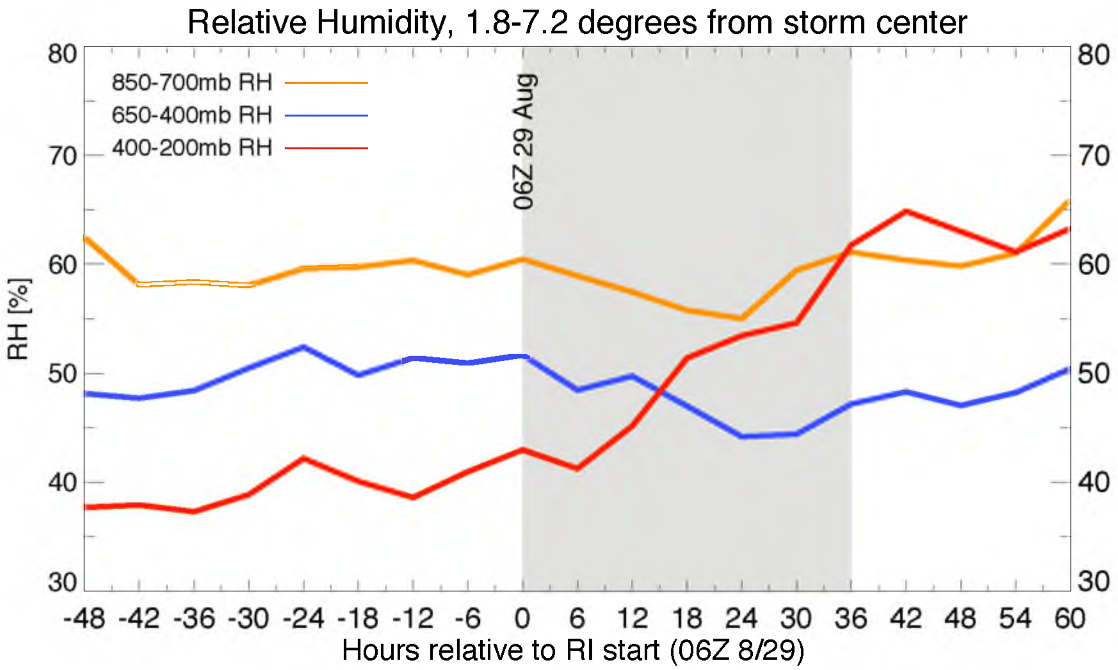

Figure 7. NCEP FNL low-level, midlevel, and upper-level layer-average RH. Pressure layers indicated by legend in upper-left corner. RI is grey-shaded.

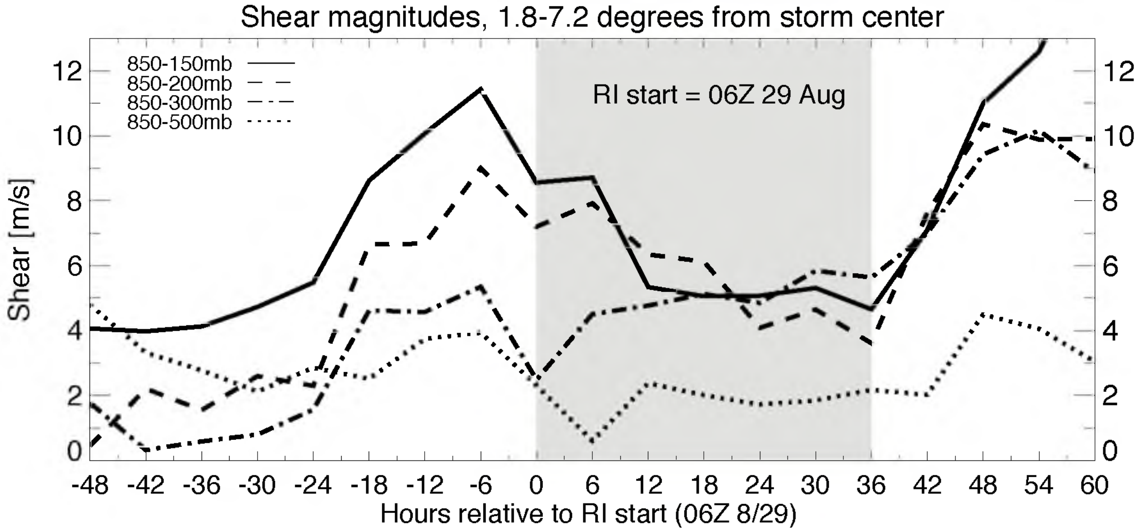

Figure 8. NCEP FNL vertical shear magnitudes. Pressure layers indicated by legend in upper-left corner. RI is grey-shaded.

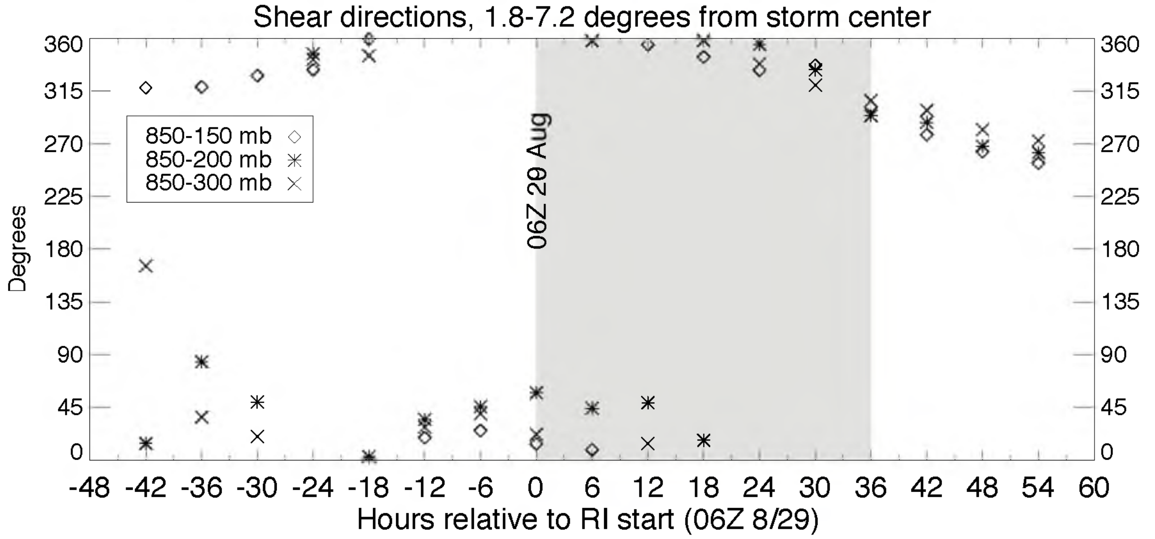

Figure 9. NCEP FNL deep-layer vertical shear directions. Pressure layers indicated by legend. RI is grey-shaded.

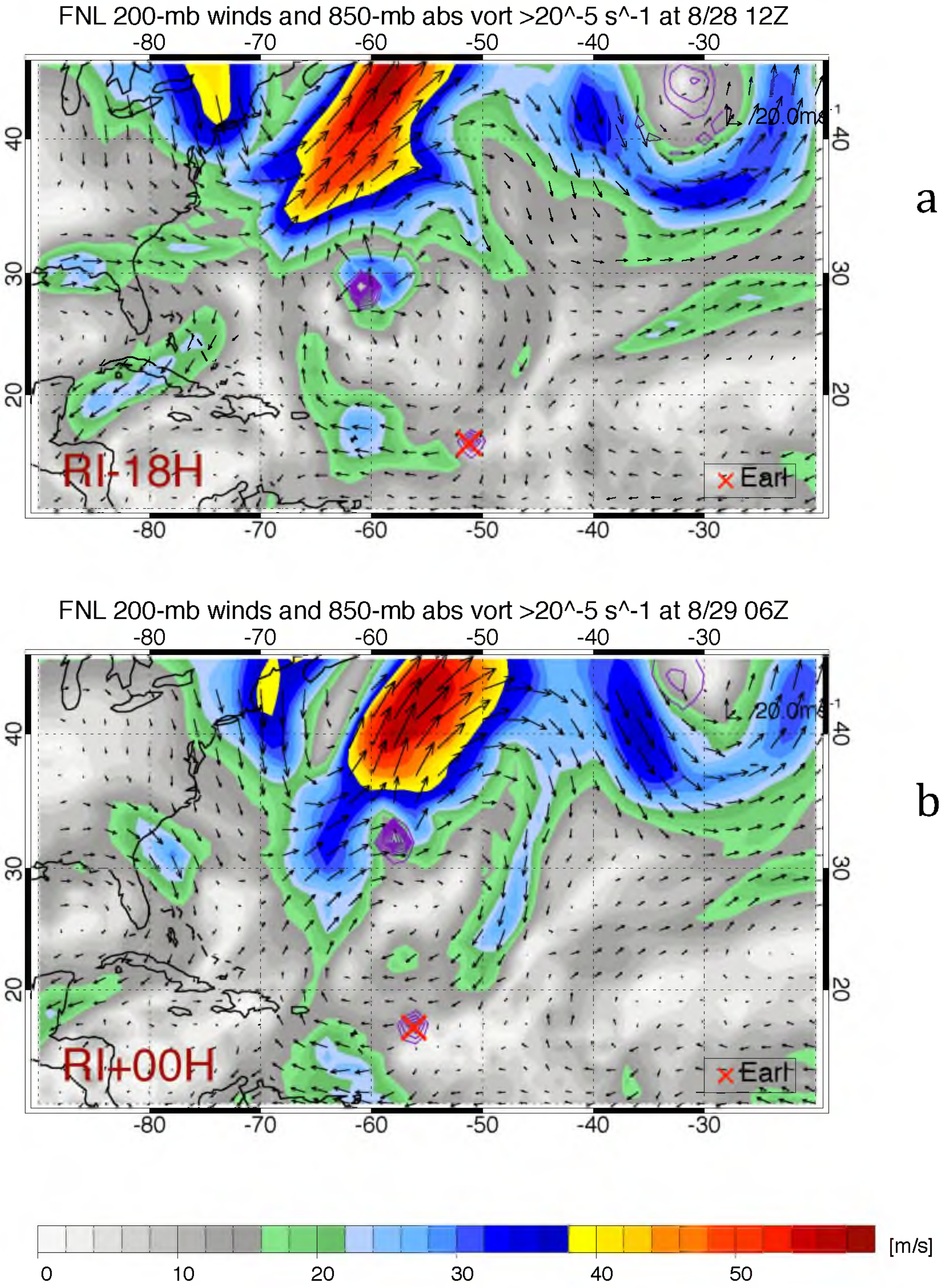

FNL 200-mb winds and 850-mb abs vort >20^-5 s^-1 at 8/28 12Z

FNL 200-mb winds and 850-mb abs vort >20^-5 s^-1 at 8/29 06Z

-80
-70
-60
-50
-40
-30
40
30
20
20.0ms-1
RI-18H
Earl
a
RI+00H
b
0
10
20
30
40
50
[m/s]

Figure 10. FNL 200-mb wind and 850-mb absolute vorticity (purple contours for vorticity $>20^{-5}$ s^{-1}, interval $>20^{-5}$ s^{-1}) at 1200 UTC August 28 (a), 0600 UTC August 29 (b), 0000 UTC August 30 (c), and 1800 UTC August 30. Red ‘X’ marks HCF TC fixes. Danielle is near 29N, 61W at 1200 UTC August 28.

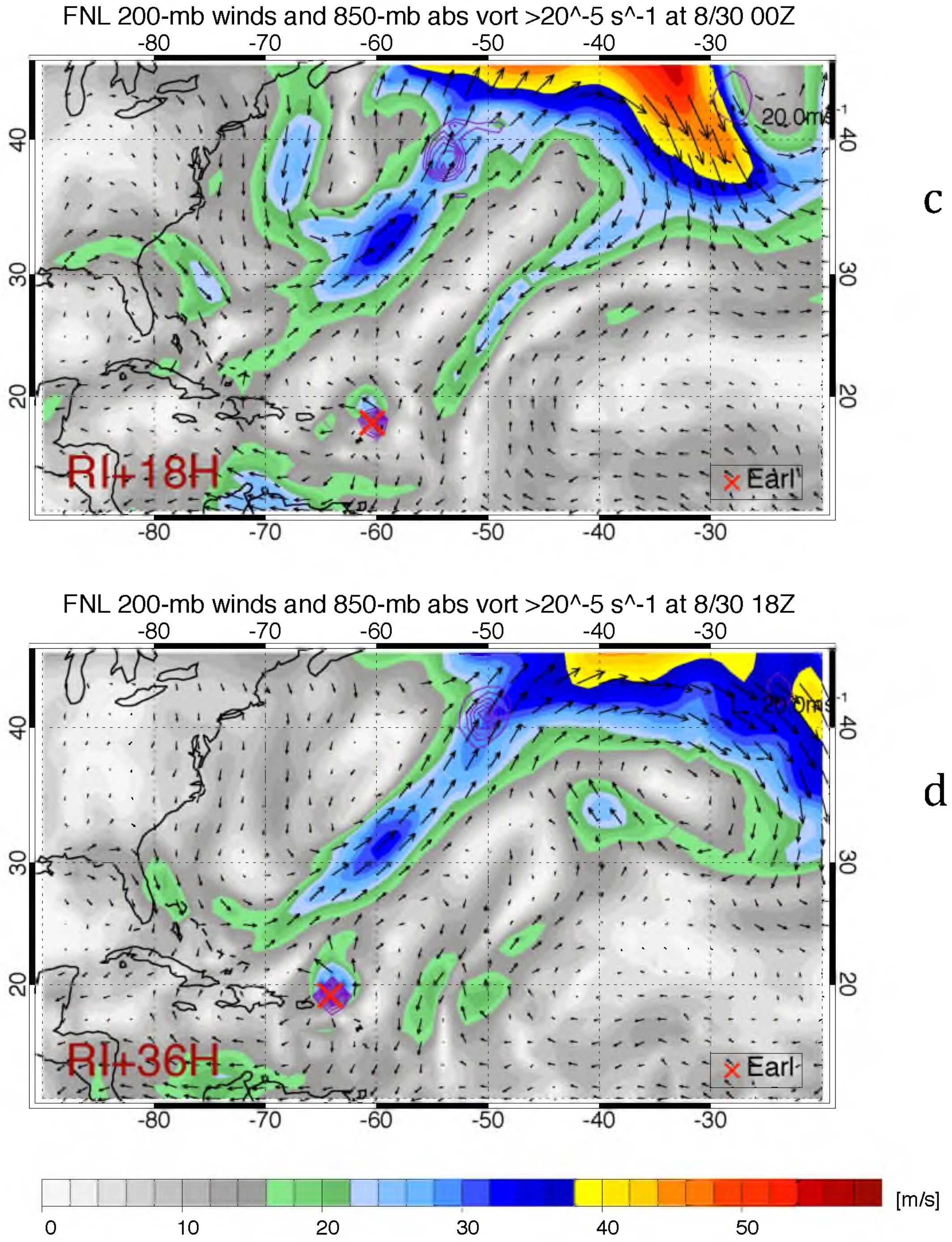
FNL 200-mb winds and 850-mb abs vort >20^-5 s^-1 at 8/30 00Z
-80
-70
-60
-50
-40
-30
40
30
20
20.0m s-1
RI+18H
Earl
c
FNL 200-mb winds and 850-mb abs vort >20^-5 s^-1 at 8/30 18Z
RI+36H
Earl
d
0
10
20
30
40
50
[m/s]

Figure 10. (Continued)

CHAPTER 5

PRECIPITATION CHARACTERISTICS AND RAPID INTENSIFICATION

5.1. Evolution of Precipitation Characteristics and Kinematic Structure

Plan-view maps of several PMW overpasses are displayed in Figure 11, illustrating the evolution of the precipitation field before RI onset, during the RI, and after the end of RI. In the period 30–48 hours before the onset of RI, cold-cloud precipitation coverage and convective intensity fluctuate dramatically between PMW passes, with a complete lack of deep inner-core convection at some times (Figure 11a-b; other PMW passes not shown). By 26 hours before the start of RI, cold-cloud precipitation coverage and convective intensity increase in the inner-core, and the inner-core convection organizes into a feature resembling a developing eyewall (Figure 11c). TMI 37 GHz color imagery (Figure 12) at this time reveals a cyan ring (Kieper and Jiang 2012) associated with the proto-eyewall feature. The appearance of a cyan ring commonly precedes RI, and in favorable environmental conditions the cyan ring is associated with a 74% probability of RI (Kieper and Jiang 2012). Deep layer shear was <6 m s^{-1} 24 hours before the start of RI, so the appearance of the developing eyewall and cyan ring feature strongly suggests that if vertical shear had not increased in the following 12 hours, the onset of RI probably would have occurred closer to 0600 UTC

August 28.

As the shear increases 12–24 hours before the onset of RI, the proto-eyewall feature disappears from PMW imagery and is replaced by a more asymmetric inner-core deep precipitation field (Figure 11d-e). The GOES IR time series in Figure 13 shows that coverage of relatively cold (tall) cloud tops decreases immediately following the increase in shear. Then, between 2–12 hours prior to the onset of RI, the tall-cloud coverage increases despite the shear. The PMW time series in Figure 14 and Figure 15 show mean inner-core convective intensity and area of strong convection also increasing during this period, and the lightning time series in Figure 16 reveals a peak in inner-core lightning frequency occurring 2–6 hours before the onset of RI. This combination of observations shows that an episode of intense, persistent convection, or a ‘convective burst,’ occurred approximately 2–12 hours prior to the start of RI, with the strongest convection likely occurring 2–6 hours before RI onset. Between 7–14 hours before the onset of RI, the feature responsible for the convective burst is a persistent region of intense convection in the eastern and southeastern quadrants of the inner-core (Figure 11e). The lightning Hovmollers (Figure 18) and the TDR merged analysis reflectivities (Figure 19a) both indicate that a significant portion of the strong convection in this ‘burst’ was located within the 2-km RMW.

Time series of strong updraft counts are shown in Figure 20 and Figure 21. 828I inner-core strong updraft counts are low compared to the other P3 flights (Figure 20), but this is probably because the strong convection sampled by the TDR remains within the same region during most of the 828I flight. Data coverage issues with the 828I TDR analyses may also have prevented an accurate census of strong updraft area. Therefore, this relatively low strong-updraft area should not be interpreted as contradicting the PMW and IR indications of an episode of strong convection at this time.

An examination of the TDR and NMT-3dvar wind fields 4–9 hours before RI onset (Figure 22a and Figure 23) reveals kinematic characteristics that may have impeded intensification during the convective burst. The vortex was tilted by nearly 0.5° between 2–8 km at this time, likely in response to the preceding increase in shear. This tilt generates strong upper-level flow across the low-level circulation center. The wind directions in Figure 23 suggest that much of the upper-tropospheric heating from inner-core convection would have been advected away from the low-level center, reducing the ability of the inner-core convection to contribute to wind speed increases at this time. The model results of Nolan et al. (2007) and Chen and Zhang (2013) both suggest that upper-level heating makes a greater contribution to intensity change than low-level heating, and if this was the case for Earl, the cross-storm flow induced by vortex tilt may have prevented the inner-core convection from strengthening the storm. The lower-and midlevel kinematic structure was also not ideal during the 828I flight. Strong azimuthally averaged midlevel inflow existed at 80–140 km radii (Figure 22a), and this flow may have allowed low-equivalent potential temperature (θ_e) air to enter the inner-core of Earl (Riemer et al. 2010; Didlake and Houze 2013), further impeding intensification.

The AMSU-B image in Figure 24a indicates that one hour before the onset of RI the strongest inner-core convection is less intense than ~6 hours earlier. However, the azimuthal coverage of cold-cloud precipitation near (~100–120 km radii) the inner-core in this image suggests an increase in cold-cloud precipitation symmetry between ~1–7 hours before RI onset (compare to Figure 11e). The AMSU-B image in Figure 24b and the SSMIS image in Figure 11f also both exhibit an increased azimuthal coverage of near-inner-core cold-cloud precipitation relative to the SSMIS image before RI onset (Figure 11e). Taken together, the PMW images in Figure 24 and Figure 11e-f suggest that an increasing trend in near-inner-core deep precipitation symmetry was underway at the start of RI, and that this increasing cold-cloud precipitation symmetry contributed to the RI onset.

The 250 K area time series in Figure 15 shows a consistently nonzero 250-K area during the 30-hour period prior to the start of RI, indicating that this necessary condition for RI was satisfied well before RI onset (see Figure 3 in Jiang and Ramirez 2013). The 250-K area remains nearly constant from 26 hours before to 6 hours after the onset of RI; thus, changes in inner-core deep precipitation coverage probably did not cause the RI of Earl. Instead, the evolution of convection before the RI onset strongly suggests that the necessary condition for RI was either the sustained convective burst 2–12 hours prior to the start of RI, an increasing trend in near-inner-core cold-cloud precipitation symmetry at the onset of RI, or a combination of both of these features. Harnos and Nesbitt (2011) suggested that in environments of moderate to high deep-layer shear (>5 m s^{-1}), intense asymmetric convection might lead to RI. The time series of convective parameters in Earl seem to support this argument, but this is not enough to determine whether the convective burst or the increasing trend in deep precipitation symmetry was a more important contributor to the onset of RI.

Looking at the period 3–8 hours after the onset of RI, the TDR and NMT-3dvar analyses show important changes in the vortex-scale kinematic structure. The vortex becomes nearly vertically aligned up to 8 km (Figure 25) despite the continuing moderate vertical shear, and strong azimuthally averaged midlevel inflow is no longer present (Figure 22b). While the vertical structure of radial wind appears to become more conducive to intensification soon after the start of RI, the radial structure of tangential wind remains apparently unfavorable 3–8 hours after RI onset. Earl has a relatively 'flat' azimuthally averaged tangential wind profile (Willoughby 1990) in both the 828I and 829H merged analyses (Figure 26a-b), and a peaked wind profile does not appear in the TDR analyses until the 829I flight (15–19 hours after the onset of RI, Figure 26c). Willoughby (1990) described two scenarios for TC development: a peaked wind profile and well-defined convective ring associated with TC intensification, and a flat wind profile and weaker convection associated with weakening TCs. Earl is different from either of these scenarios in that during the early stages of RI the storm contained a flat wind profile and intense convection in the absence of a well-defined convective ring.

PMW and lightning time series show a second episode of intense inner-core convection approximately 6–12 hours after the onset of RI (Figure 15 and Figure 16). Lightning data indicate that this episode contains a lower frequency of strong convective updrafts than the episode before RI onset. However, this later convective episode may have contributed more to the RI than the preceding convective burst. The lightning Hovmoller (Figure 18) and strong updraft counts time series (Figure 21) show that most of the strongest convection is confined within the RMW during the convective episode 6–12 hours after RI onset. The vortex is relatively well-aligned by the onset of this second burst, suggesting that unlike during the times 4–9 hours before RI onset, upper-level heating 6–12 hours after the start of RI could efficiently contribute to increases in wind speed (Chen and Zhang 2013).

Lightning and TDR time series show that most of the strongest convection dissipates by 15–20 hours after RI onset (Figure 16, Figure 20), but large areas of strong and moderate deep convection remain (Figure 11h, Figure 15, and Figure 19c). The PCT distribution in Figure 17 suggests that the lowest radial bin-average PCT lay near or slightly outside of the RMW at this time. However, the RMW was highly slanted (Figure 26c), so this convection may be located within the RMW at 10–12 km altitude. The rate of wind speed change did not decrease during this period, suggesting that as with many TCs (Jiang and Ramirez 2013), intense convective cells may have enhanced the intensification, but the strongest convection was not necessary for RI.

PMW plan views depict the formation of a convective ring (Willoughby 1990) eyewall (Figure 11i) 18–24 hours after the onset of RI. The PMW and TDR plan views and the PMW Hovmoller plot show that this convective ring contracts over the following 18 hours (Figure 11j-k, Figure 17, Figure 19d-e). The deep-layer vertical shear is between 4–6 m s^{-1} during the later 18 hours of RI, approximately half the magnitude of the 7–12 m s^{-1} 850–200 and 850–150 mb shears that persisted between 12 hours before and 6 hours after the RI onset (Figure 8). Unlike the earlier periods of RI, this later mode of intensification more closely resembles the axisymmetric convective ring scenario described in Willoughby (1990). The convective ring development and contraction following a decrease in shear provides further indication that, in agreement with the results of Harnos and Nesbitt (2011) and Kieper and Jiang (2012), the convective ring mode of intensification tends to occur in favorable environmental conditions. In the case of Earl, the ongoing RI may have also contributed to the formation of the convective ring. The PMW inner-core 250-K percent area decreases following the formation of the ring-like eyewall (Figure 15), suggesting that in stronger hurricanes, as Cecil and Zipser (1999) conjectured, eyewall processes become more important than the cold-cloud precipitation characteristics within an arbitrarily defined ‘inner-core’ region.

The convective ring eyewall forms across and within the 8-km RMW (Figure 17), and contracts over the rest of the RI period. By 28–32 hours after the onset of RI, the eyewall convective ring, ascending portion of the secondary circulation, and the vast majority of strong convective cells are all located within the RMW (Figure 19d, Figure 21, and Figure 22d), representing a kinematic and convective structure that favors further efficient convective heating and storm strengthening (Pendergrass and Willoughby 2009; Vigh and Schubert 2009; Rogers et al. 2013a). TDR and merged TDR analyses show that a favorable convective and kinematic structure persists following the end of RI (Figure 19e, Figure 21, and Figure 22e), and Best Track data show that the minimum MSLP of Earl continues to drop for 12 hours after the maximum wind speed stops increasing (Figure 3). The azimuthally averaged secondary circulation from the 830I flight (39–42 hours after RI onset) exhibited a deep region of inner-rainband ascent outside of the eyewall (Figure 22e), suggesting the beginnings of a secondary eyewall. PMW imagery 47 hours after the onset of RI (about 11 hours after the end of RI; Figure 11l) shows that a secondary eyewall did in fact form. This secondary eyewall probably prevented tightening of the primary eyewall pressure gradient, causing the maximum wind speed to reach a steady state even as the primary eyewall convection led to further decreases in MSLP. The TDR merged analyses indicate that the secondary eyewall had begun to form before the deep-layer vertical shear reached levels associated with TC weakening (10 m s^{-1} 12 hours after the end of RI), suggesting that the decrease in MSLP was halted by interference from the secondary eyewall and not by the concurrent increase in shear.

5.2. Convection, Alignment, and the Onset of RI

Figure 27 shows the 828I NMT-3dvar analysis 4-km wind vectors and radial winds and contoured 91 GHz PCT at 2300 UTC August 28 (the same PMW pass as in Figure 11e). The deep precipitation field features a stationary rainband complex (Willoughby et al. 1984) and a region of strong convection in the southern and eastern quadrants of the inner-core, in a pattern strongly resembling the Chen et al. (2006) composite for moderately sheared (850–200 mb shear >7.5 m s^{-1}) TCs. The strongest midlevel inflow occurs in the southern and southeastern quadrants, within the stationary rainband. TDR analysis cross-sections in Figure 28 and Figure 29 illustrate the vertical structure of the inflow in the eastern and southeastern quadrants. Air flows inward at midlevels in a broad region of mostly stratiform precipitation, and then descends into the lower troposphere near the center of Earl. Didlake and Houze (2013) observed a similar mid-tropospheric inflow and downdraft circulation in a rainband of Hurricane Rita (2005) in the presence of 10 m s^{-1} of 850–200 mb shear. The resemblance between the precipitation structure in Earl and past studies of sheared TCs suggests that both the asymmetric cold-cloud precipitation structure and the associated mesoscale circulation in Earl were produced as a response to the moderate shear.

Didlake and Houze (2013) hypothesized that the midlevel inflow in the stationary rainband acts to weaken a TC by two mechanisms: inward transport of low-θ_e air ventilates the warm core, and the organized region of inflow increases the tangential wind outside of the eyewall, leading to the formation of a secondary eyewall. The thermodynamic effect would be even more pronounced in Earl, because unlike in Rita

(2005), the stationary band of Earl is directly attached to the inner-core convection. The winds in Figure 29 suggest that the connection between the midlevel inflow and the inner-core convection allows the midlevel inflow to descend into the inner-core boundary layer through convective downdrafts near the TC center. As Riemer et al. (2010) noted, the transport of low-θ_e air into the boundary layer would be even more detrimental to the TC heat engine than the ventilation of mid-tropospheric air into the midlevel portion of the TC warm core. Earl did not have an eyewall before the onset of RI, but the expansion of the RMW between the 828I and 829H flights suggests that the kinematic structure associated with the stationary rainband before RI onset acted to increase the tangential wind well outside of the RMW, which may have delayed the onset of RI. The combination of detrimental kinematic and thermodynamic processes during the 828I flight provide further evidence that even though persistent, strong inner-core convection was present 4–9 hours before RI onset, the vortex-scale kinematic structure may have prevented rapid intensification during that time period.

Figure 30a-f illustrates the spatial evolution of cloud cover and lightning locations during the pre-RI convective burst. Between 6–10 hours before the onset of RI, the strongest convection is located in the eastern and southeastern quadrants of the inner-core (Figure 30a-c, Figure 11e). About 4–5 hours before RI onset, the inner-core lightning frequency increases dramatically and the strongest convection migrates to the northeastern and northern quadrants (Figure 30d-e, reflectivity in Figure 28). The lightning cluster remains in the northern and northeastern quadrants 2–3 hours before the onset of RI as the lightning frequency decreases, signaling the end of the convective burst (Figure 30f).

The migration of convection into the northeastern and northern quadrants 2–6 hours before RI onset may have been the change in precipitation structure that allowed RI to occur. The AMSU-B images in Figure 24 indicate an increasing trend in near-inner-core cold-cloud precipitation symmetry soon after this convective migration, suggesting that the migration of convection into the northern and northeastern quadrants may have caused these increases in cold-cloud precipitation symmetry. The increasing trend in cold-cloud precipitation symmetry near RI onset likely contributed to increased vortex alignment, and increased vortex alignment could then have caused further increases in cold-cloud precipitation symmetry. Alternatively, the evolution of the 828I TDR analysis 8-km wind (Rogers et al. 2014) suggests that the upper-level vortex may have rotated cyclonically into the northeastern and northern quadrants of Earl at the same time that the convective burst migrated into those quadrants. This possible vortex precession may have also contributed to decreases in vortex tilt. Whether the initial decreases in vortex tilt were caused by the precession of the vortex or increases in cold-cloud precipitation symmetry, a positive feedback between increases in cold-cloud precipitation symmetry and vortex alignment likely developed and led to the vertically aligned vortex and continued increases in cold-cloud precipitation symmetry observed soon after RI onset (Figure 25b and Figure 11f-g).

By 3–8 hours after RI onset, the azimuthally averaged midlevel inflow is much weaker than before RI onset (Figure 22a-b). The midlevel inflow and downdraft circulation 4–9 hours before RI onset was likely a kinematic component of the highly asymmetric deep precipitation structure observed at that time. Therefore, the vortex alignment and increase in cold-cloud precipitation symmetry between the 828I and 829H flights was likely also responsible for the improved azimuthally averaged radial wind structure observed in the 829H merged TDR analysis.

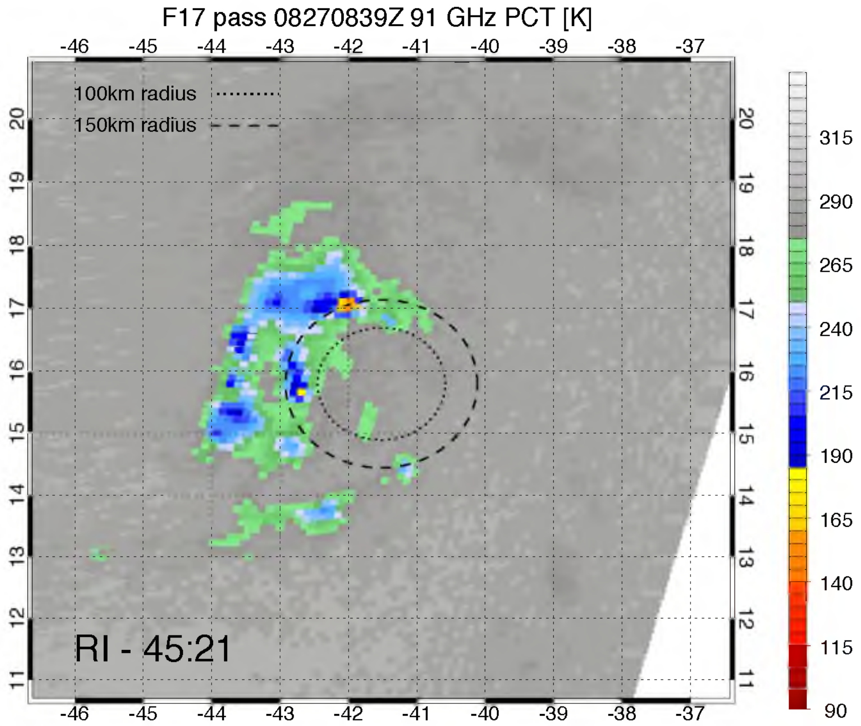
F17 pass 08270839Z 91 GHz PCT [K]
100km radius
150km radius
RI - 45:21
-46
-45
-44
-43
-42
-41
-40
-39
-38
-37
20
19
18
17
16
15
14
13
12
11
315
290
265
240
215
190
165
140
115
90

a

Figure 11. 85–91 GHz PCT from various satellites at 0839 UTC August 27 (a), 2233 UTC August 27 (b), 0413 UTC August 28 (c), 1639 UTC August 28 (d), 2227 UTC August 28 (e), 1102 UTC August 29 (f), 1723 UTC August 29 (g), 2351 UTC August 29 (h), 0357 UTC August 30 (i), 1226 UTC August 30 (j), 1806 UTC August 30 (k), and 0438 UTC August 31 (l).

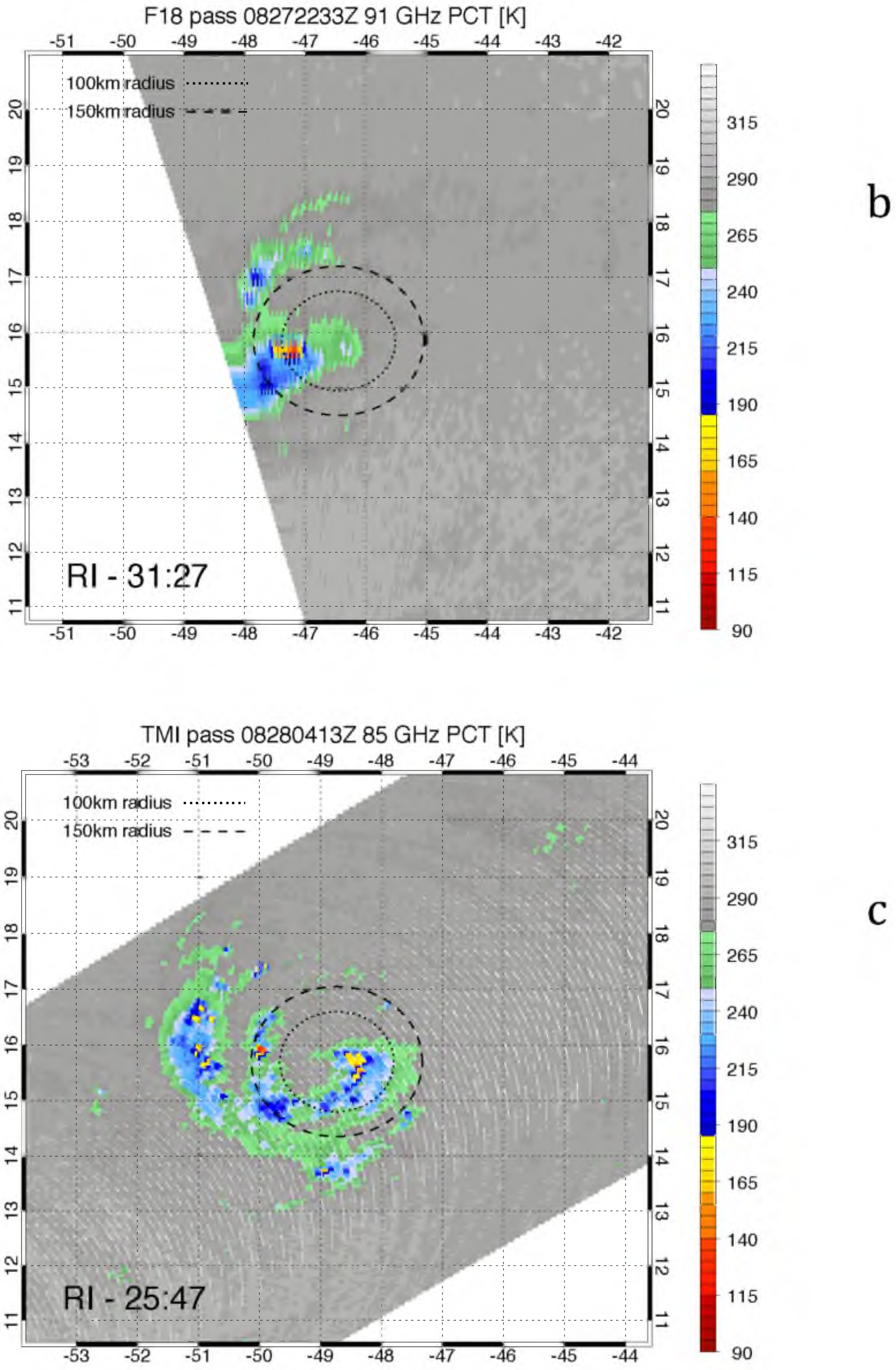
F18 pass 08272233Z 91 GHz PCT [K]
100km radius
150km radius
RI - 31:27
b
TMI pass 08280413Z 85 GHz PCT [K]
100km radius
150km radius
RI - 25:47
c
315
290
265
240
215
190
165
140
115
90

Figure 11. (Continued)

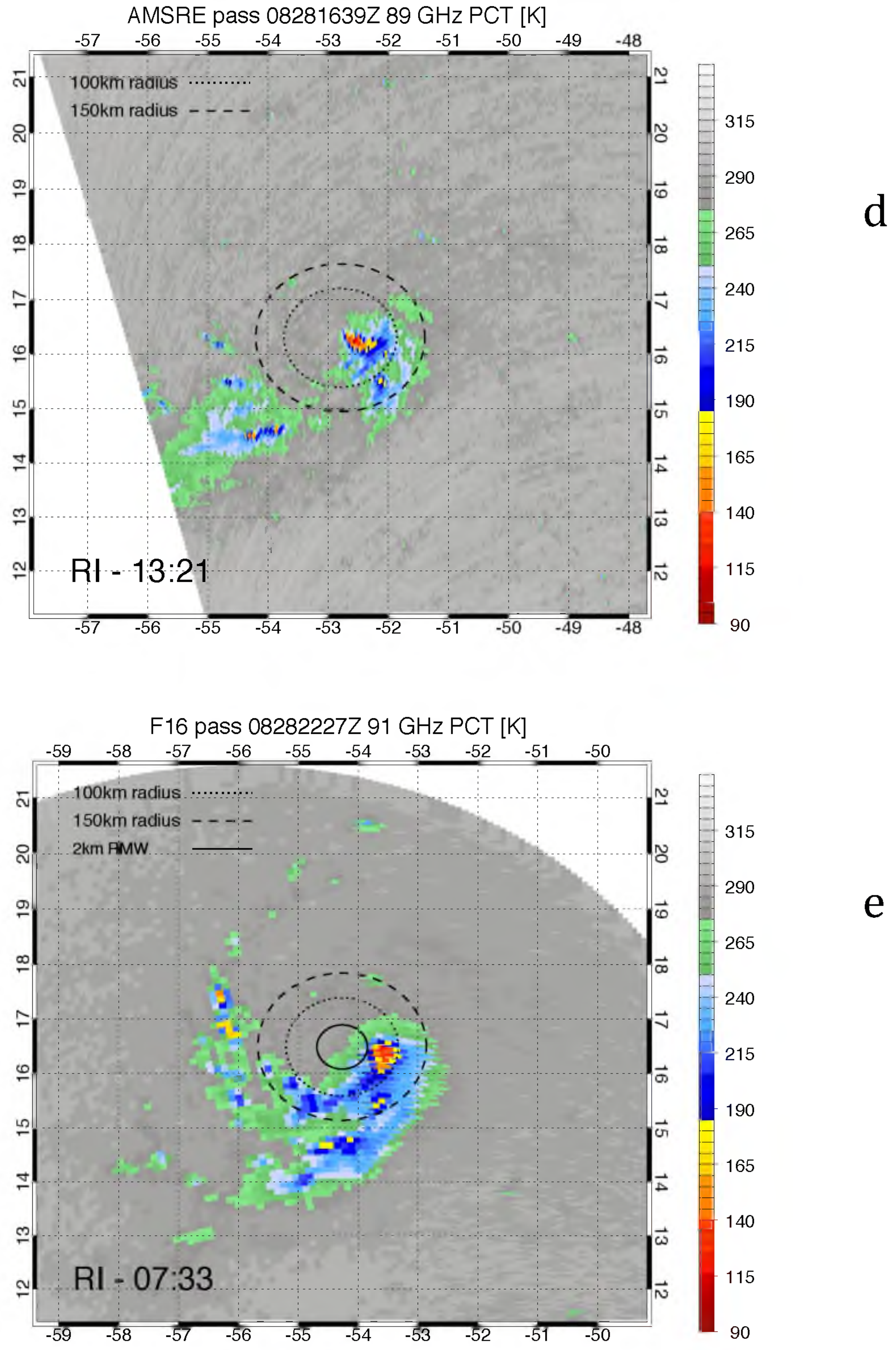
AMSRE pass 08281639Z 89 GHz PCT [K]
-57 -56 -55 -54 -53 -52 -51 -50 -49 -48
21 20 19 18 17 16 15 14 13 12
100km radius
150km radius
RI - 13:21
315 290 265 240 215 190 165 140 115 90
d
F16 pass 08282227Z 91 GHz PCT [K]
-59 -58 -57 -56 -55 -54 -53 -52 -51 -50
21 20 19 18 17 16 15 14 13 12
100km radius
150km radius
2km RMW
RI - 07:33
315 290 265 240 215 190 165 140 115 90
e

Figure 11. (Continued)

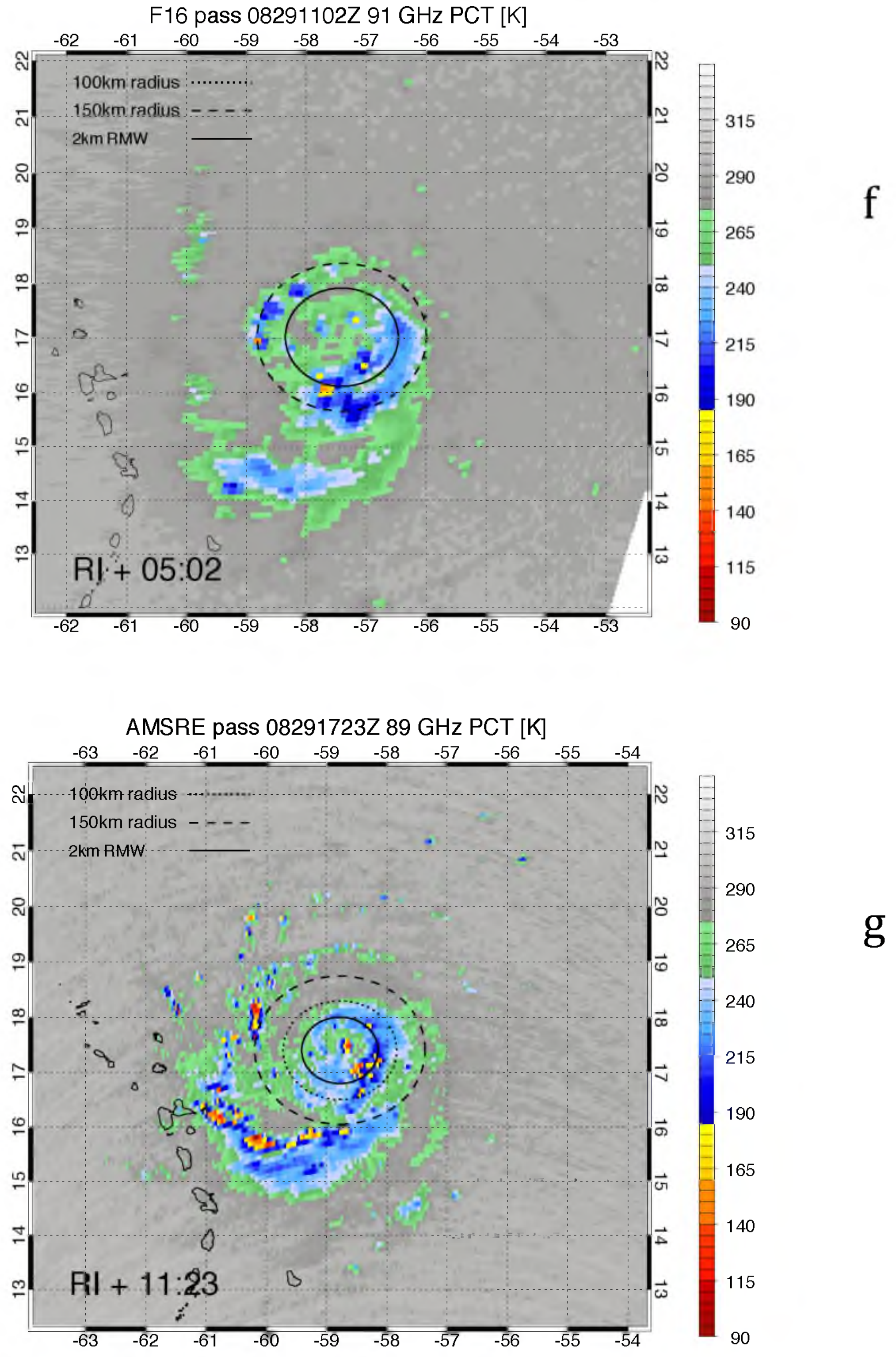
F16 pass 08291102Z 91 GHz PCT [K]
-62
-61
-60
-59
-58
-57
-56
-55
-54
-53
22
21
20
19
18
17
16
15
14
13
100km radius
150km radius
2km RMW
RI + 05:02
315
290
265
240
215
190
165
140
115
90
f
AMSRE pass 08291723Z 89 GHz PCT [K]
-63
-62
-61
-60
-59
-58
-57
-56
-55
-54
22
21
20
19
18
17
16
15
14
13
100km radius
150km radius
2km RMW
RI + 11:23
315
290
265
240
215
190
165
140
115
90
g

Figure 11. (Continued)

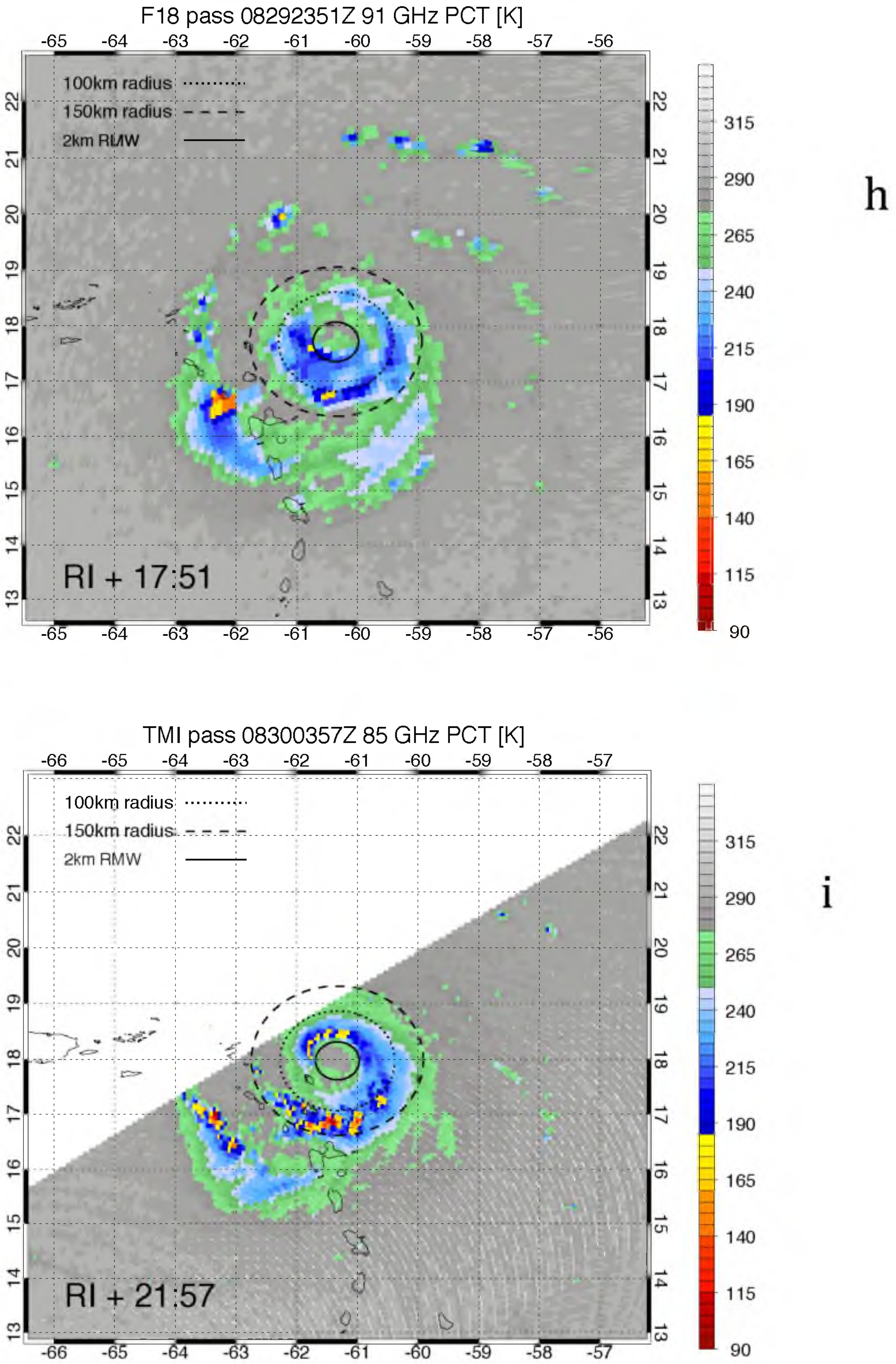
F18 pass 08292351Z 91 GHz PCT [K]
100km radius
150km radius
2km RMW
RI + 17:51
-65
-64
-63
-62
-61
-60
-59
-58
-57
-56
22
21
20
19
18
17
16
15
14
13
315
290
265
240
215
190
165
140
115
90
h
TMI pass 08300357Z 85 GHz PCT [K]
100km radius
150km radius
2km RMW
RI + 21:57
-66
-65
-64
-63
-62
-61
-60
-59
-58
-57
22
21
20
19
18
17
16
15
14
13
315
290
265
240
215
190
165
140
115
90
i

Figure 11. (Continued)

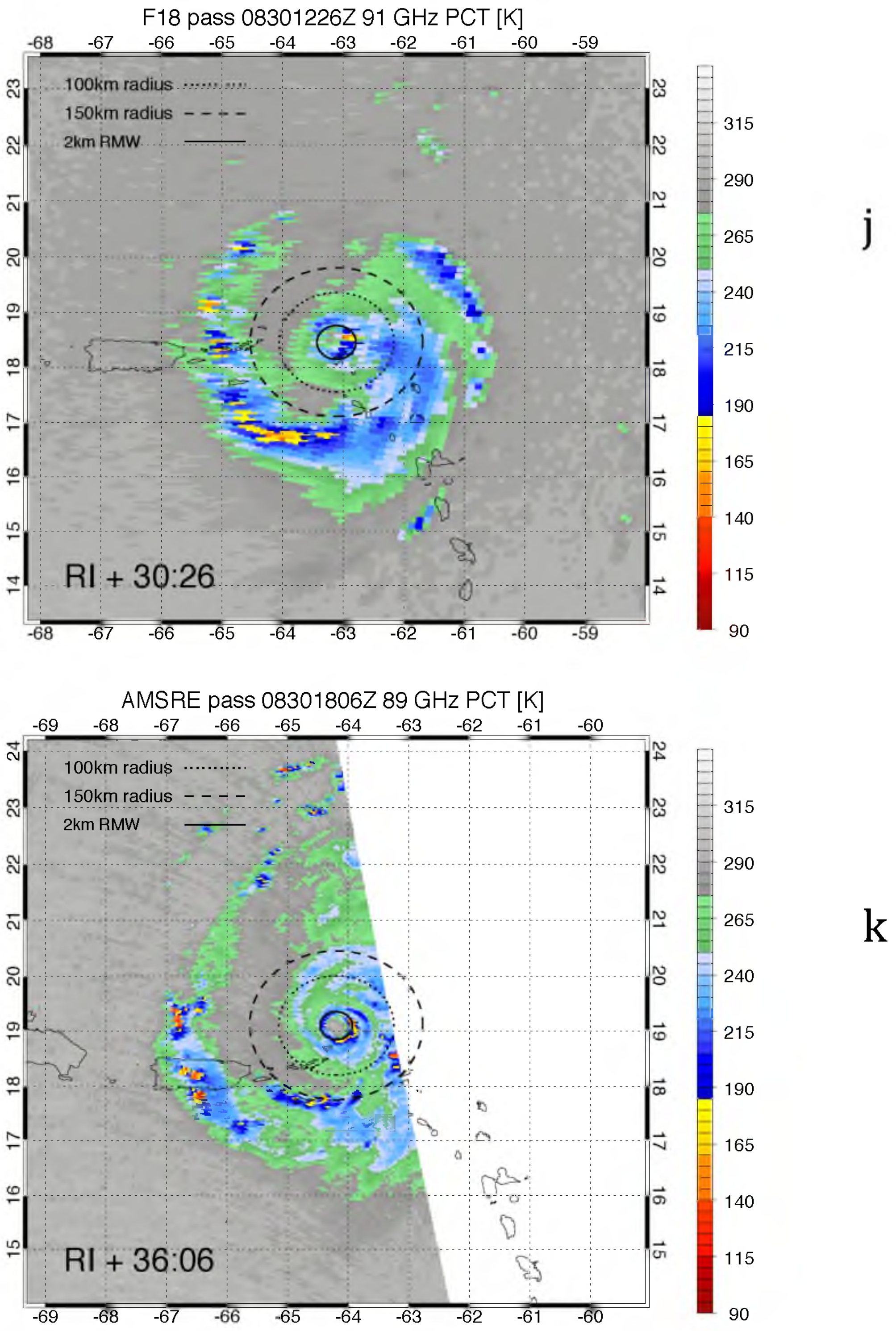
F18 pass 08301226Z 91 GHz PCT [K]
-68 -67 -66 -65 -64 -63 -62 -61 -60 -59
23 22 21 20 19 18 17 16 15 14
100km radius
150km radius
2km RMW
RI + 30:26
315 290 265 240 215 190 165 140 115 90
j
AMSRE pass 08301806Z 89 GHz PCT [K]
-69 -68 -67 -66 -65 -64 -63 -62 -61 -60
24 23 22 21 20 19 18 17 16 15
100km radius
150km radius
2km RMW
RI + 36:06
315 290 265 240 215 190 165 140 115 90
k

Figure 11. (Continued)

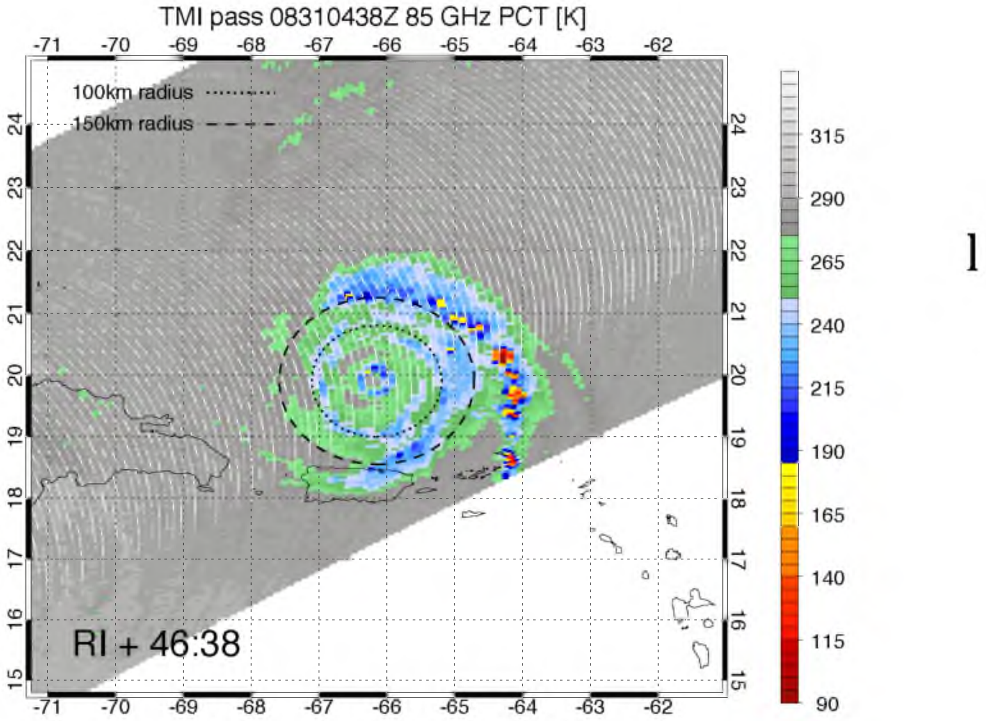
TMI pass 08310438Z 85 GHz PCT [K]
100km radius
150km radius
RI + 46:38
-71
-70
-69
-68
-67
-66
-65
-64
-63
-62
15
16
17
18
19
20
21
22
23
24
315
290
265
240
215
190
165
140
115
90
l

Figure 11. (Continued)

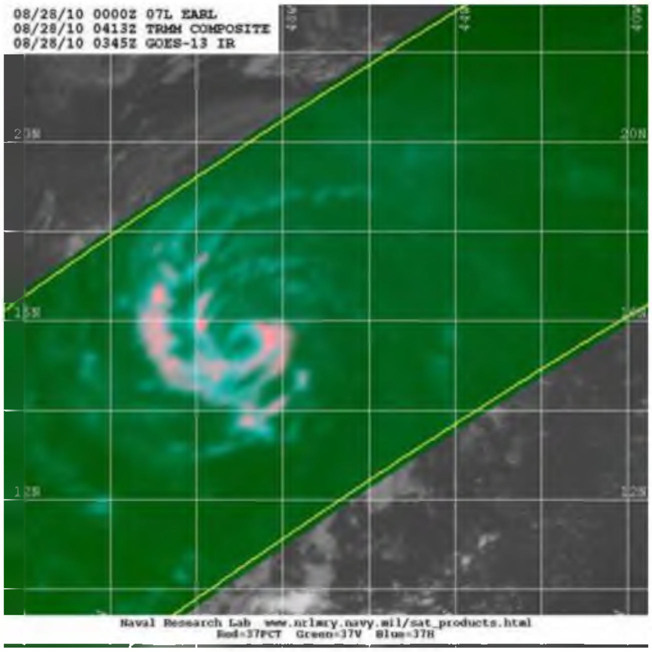
08/28/10 0000Z 07L EARL
08/28/10 0413Z TRMM COMPOSITE
08/28/10 0345Z GOES-13 IR
48W
44W
40W
20N
20N
16N
16N
12N
12N
Naval Research Lab www.nrlmry.navy.mil/sat_products.html
Red=37PCT Green=37V Blue=37H

RI-25:47

Figure 12. TRMM TMI 37 GHz color composite at 0413 UTC August 28.

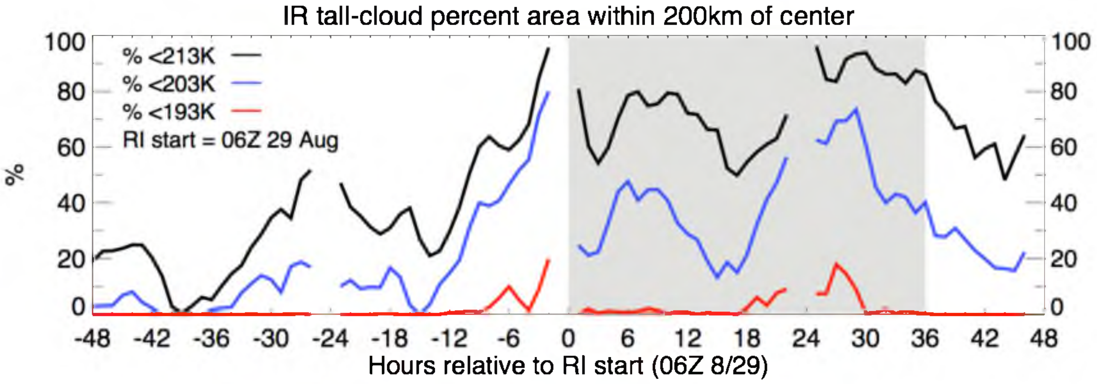

Figure 13. GOES IR fractional coverage of relatively cold (tall) cloud tops within 200 km from TC center. Gaps in the time series represent periods in the IR dataset in which 5% or more of the data points are missing within 500 km of the HCF center; as a consequence, the fractional areas are considered inaccurate for those times. RI is grey-shaded.

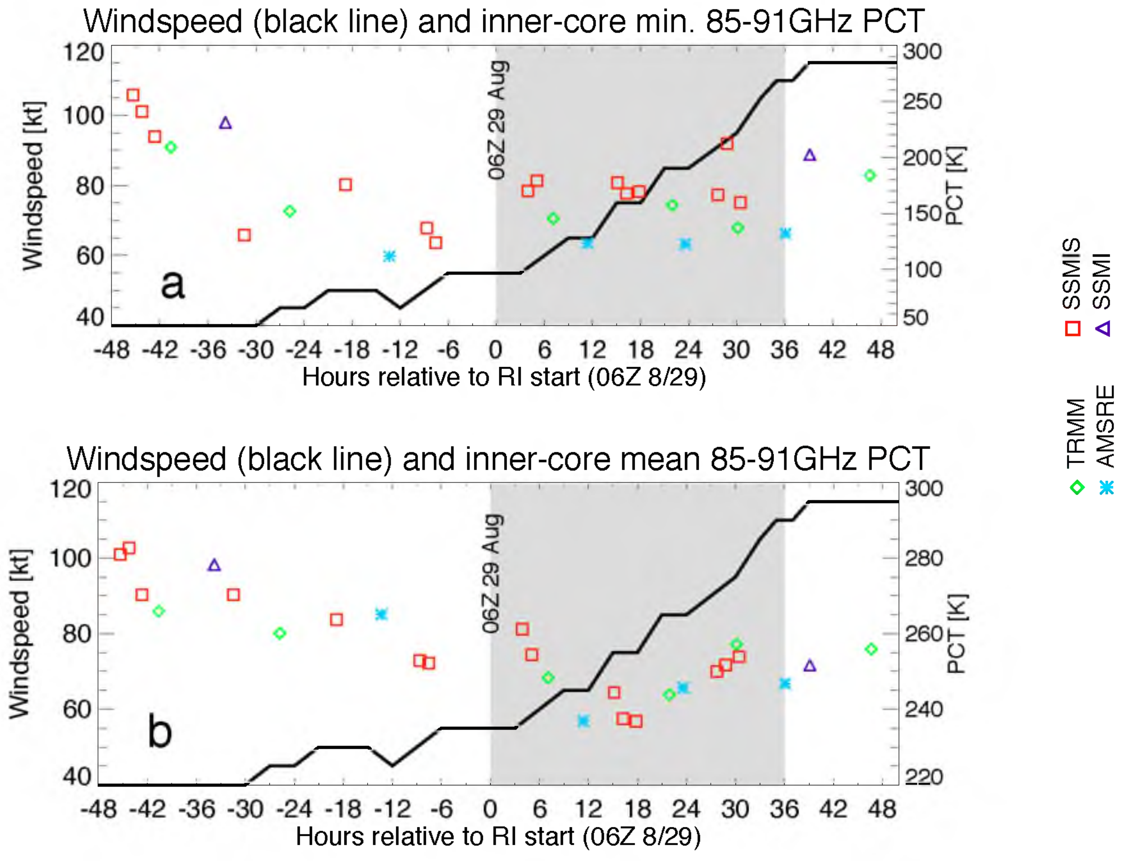

Figure 14. NHC advisory windspeed, and minimum (a) and mean (b) 85–91 GHz PCT within 100 km from TC center. Center fixes are interpolated from HCF data, with additional subjective adjustments made based on flight-level data, TDR analyses, and PMW images. RI is grey-shaded.

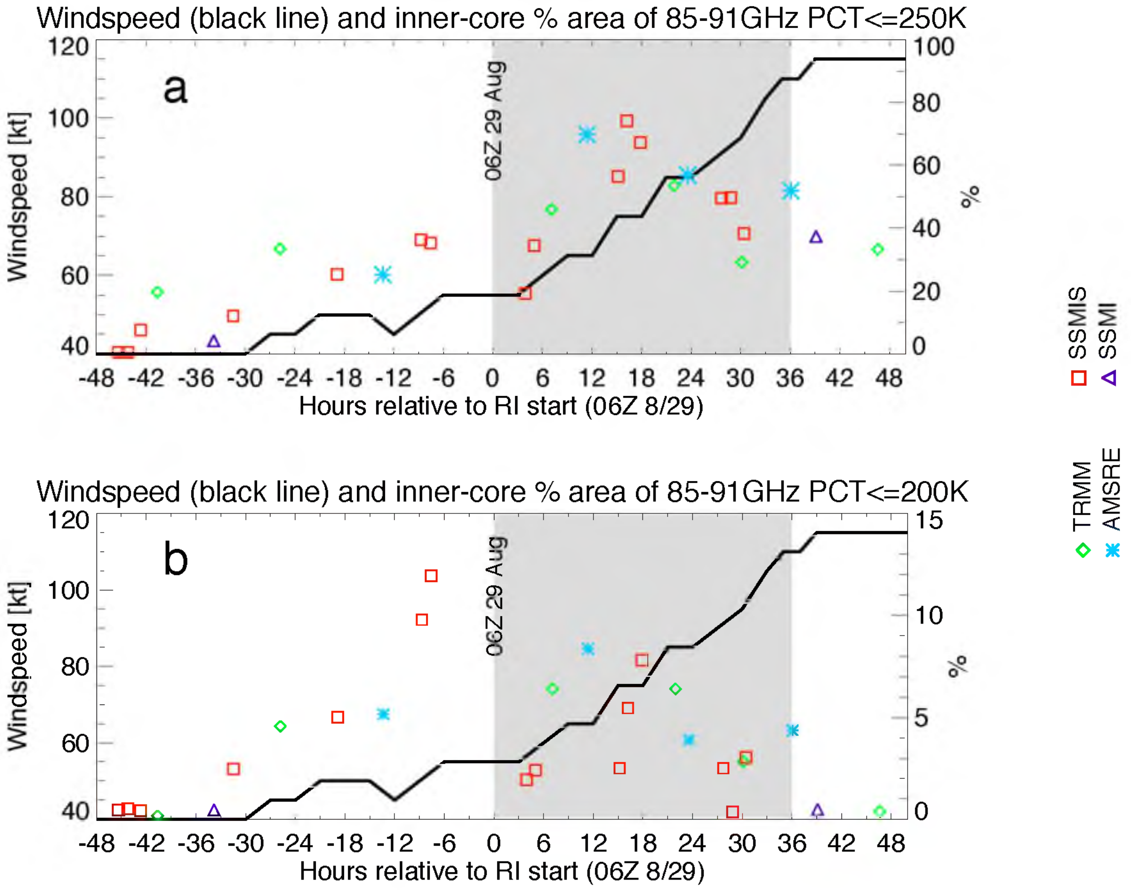

Figure 15. NHC advisory windspeed and fractional areas of PCT≤250 K (a) and PCT≤200 K (b) within 100 km from TC center. Center fixes are interpolated from HCF data, with additional subjective adjustments made based on flight-level data, TDR analyses, and PMW images. RI is grey-shaded.

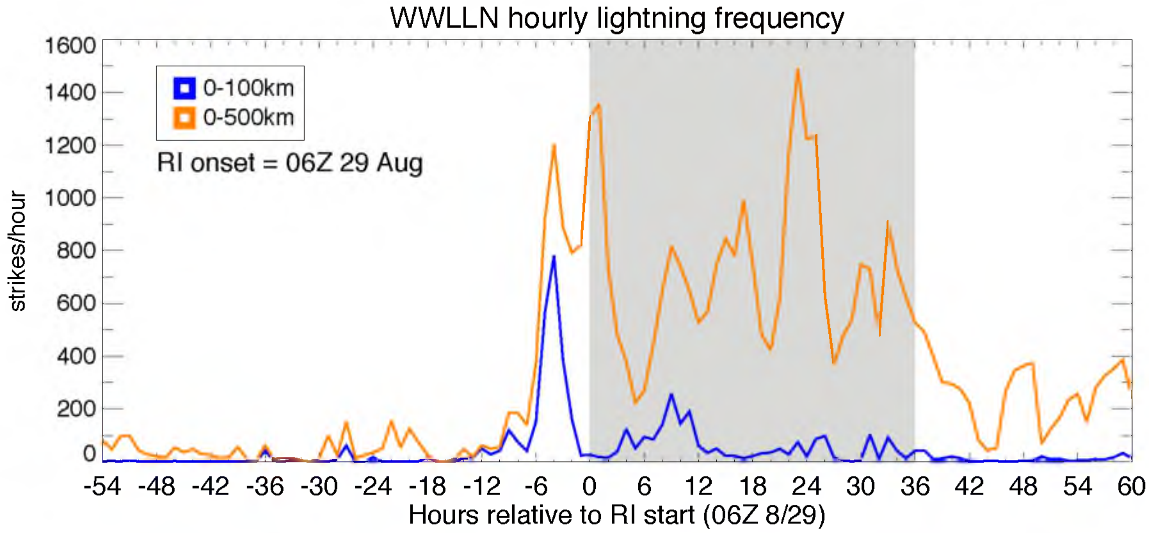

Figure 16. WWLLN hourly lightning frequency (strikes/hour) within 100 km and 500 km from center (as in Corbosiero et al. 2013, except with HCF TC centers). RI is grey-shaded.

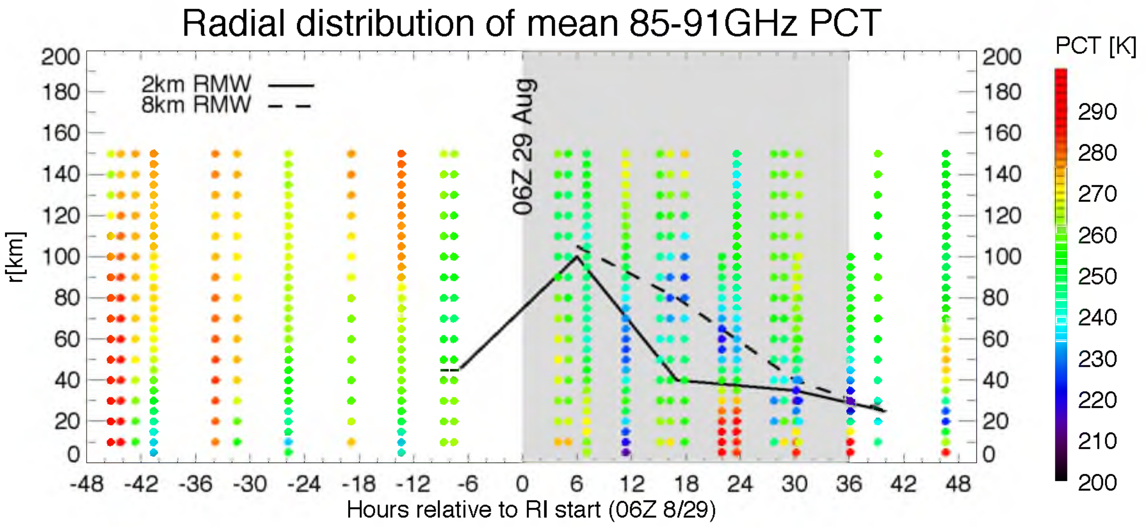

Figure 17. Radial distribution of mean 85–91 GHz PCT. RI is grey-shaded. The 2-km (solid) and 8-km (dash) interpolated P3 RMW locations are overlaid.

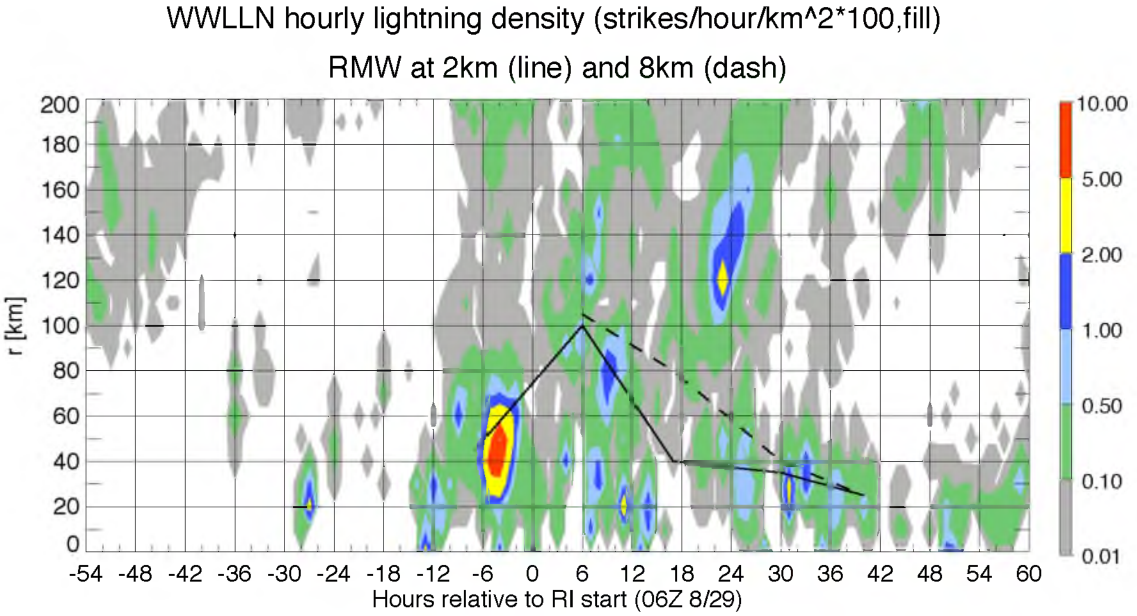

Figure 18. Hovmoller plots of WWLLN hourly lightning density. TC centers are from HCF dataset. Radial bins are 10 km wide. The 2-km (solid) and 8-km (dash) interpolated P3 RMW locations are overlaid.

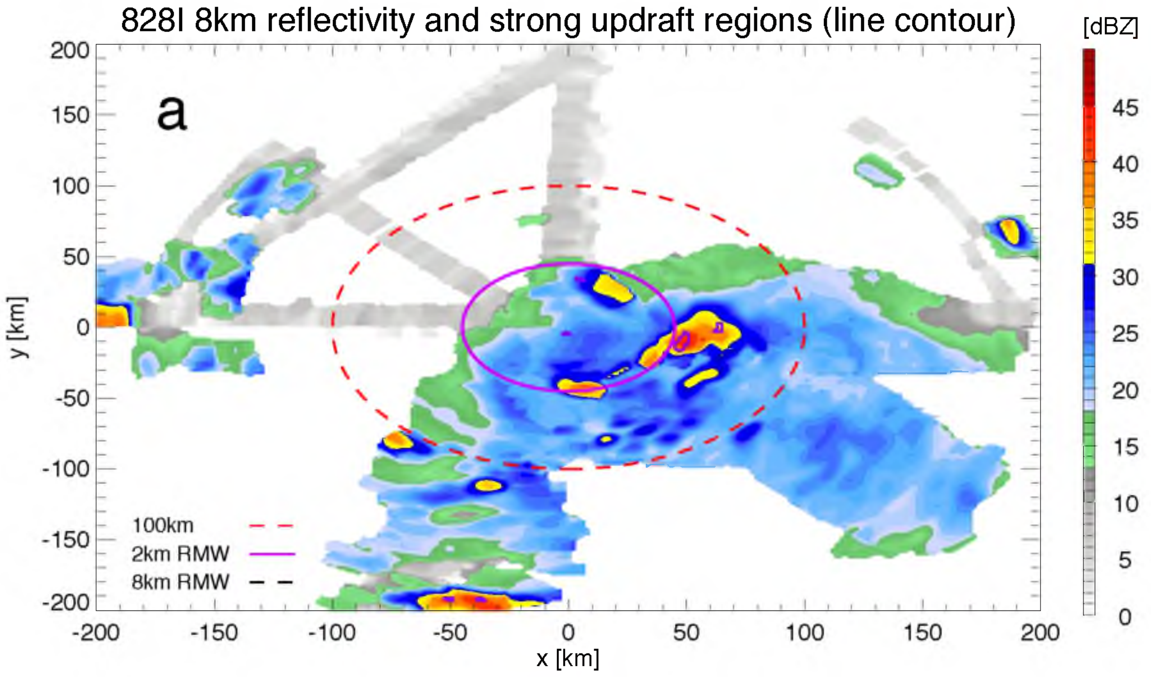

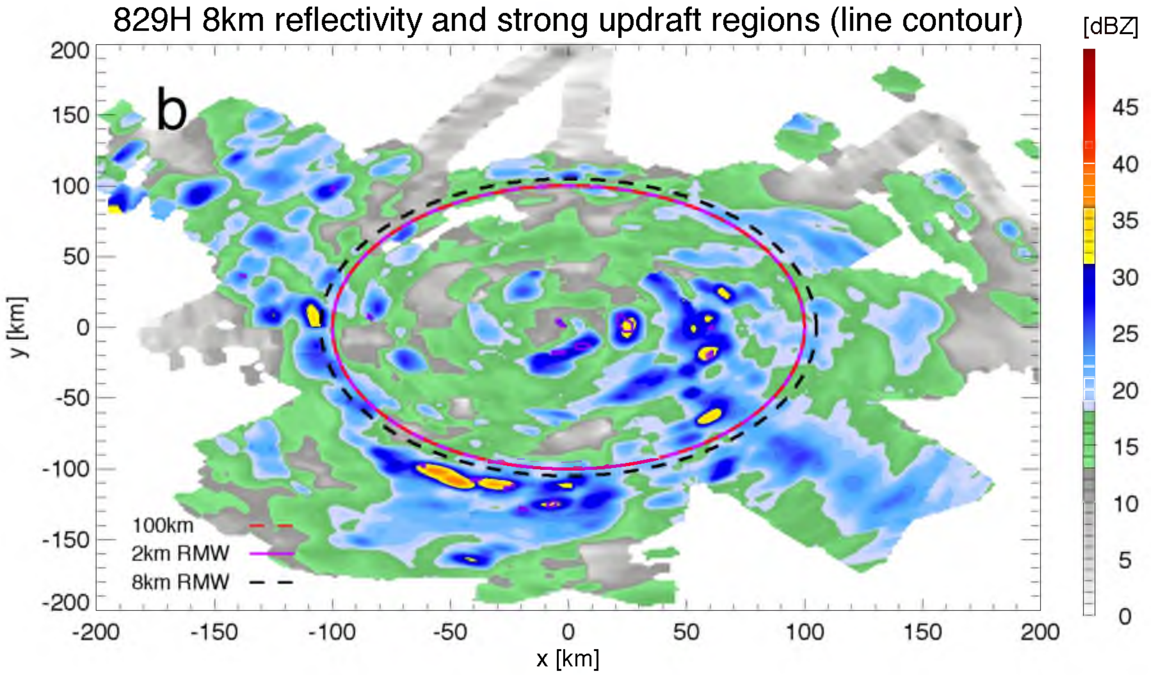

Figure 19. TDR merged analysis 8-km reflectivity (shaded) and TDR analysis strong updraft areas (purple line contour) for the 828I (a), 829H (b), 829I (c), 830H (d), and 830I (e) NOAA P3 flights (see Figure 4).

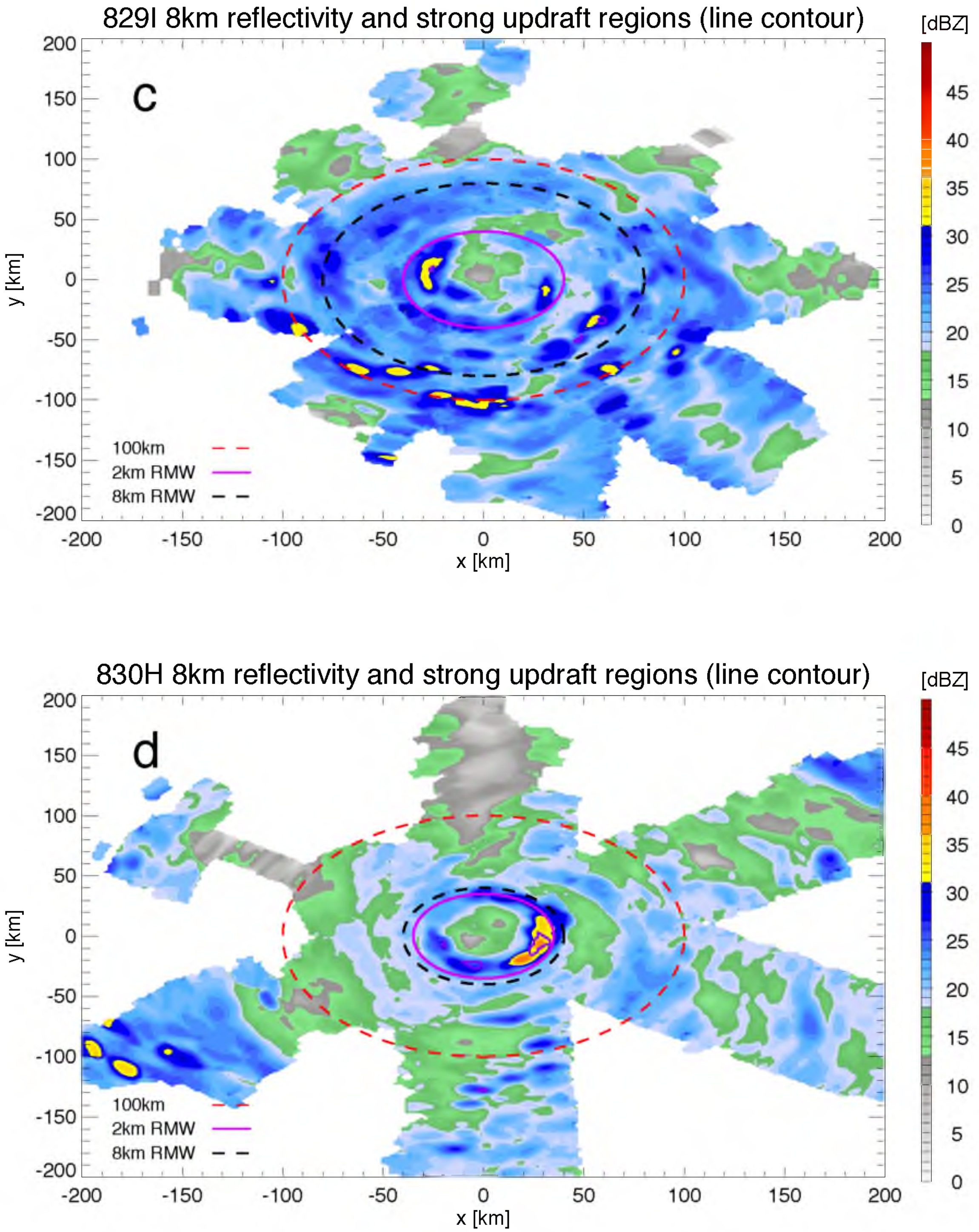

Figure 19. (Continued)

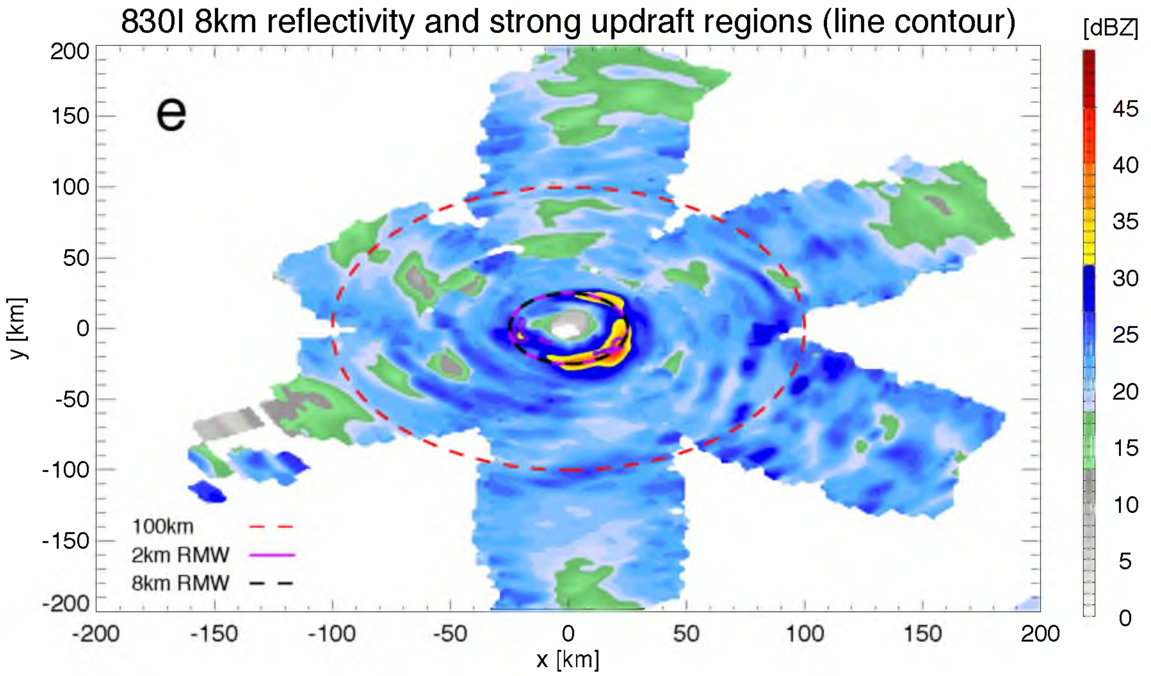

Figure 19. (Continued)

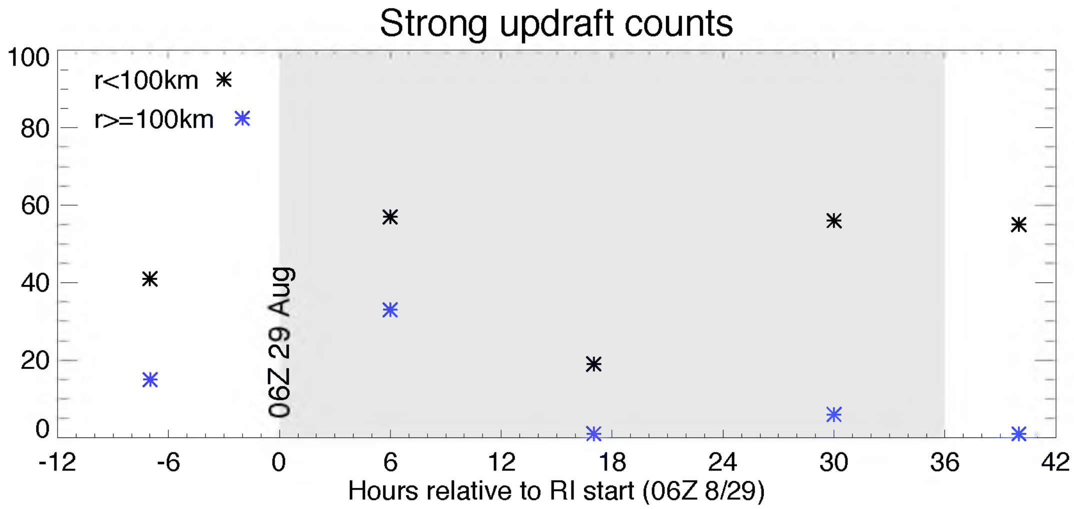

Figure 20. TDR analyses number of strong updrafts for Earl RI P3 flights. Points are plotted at the estimated center-time of the corresponding P3 flight (see Figure 4). RI is grey-shaded.

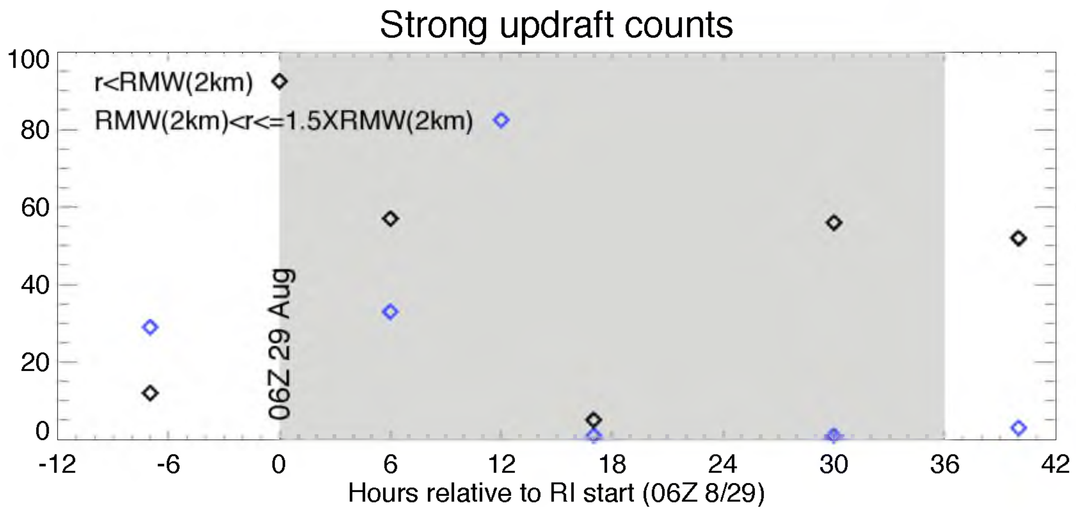

Figure 21. As in Figure 20, but for strong updraft counts within and outside of the 2-km RMW.

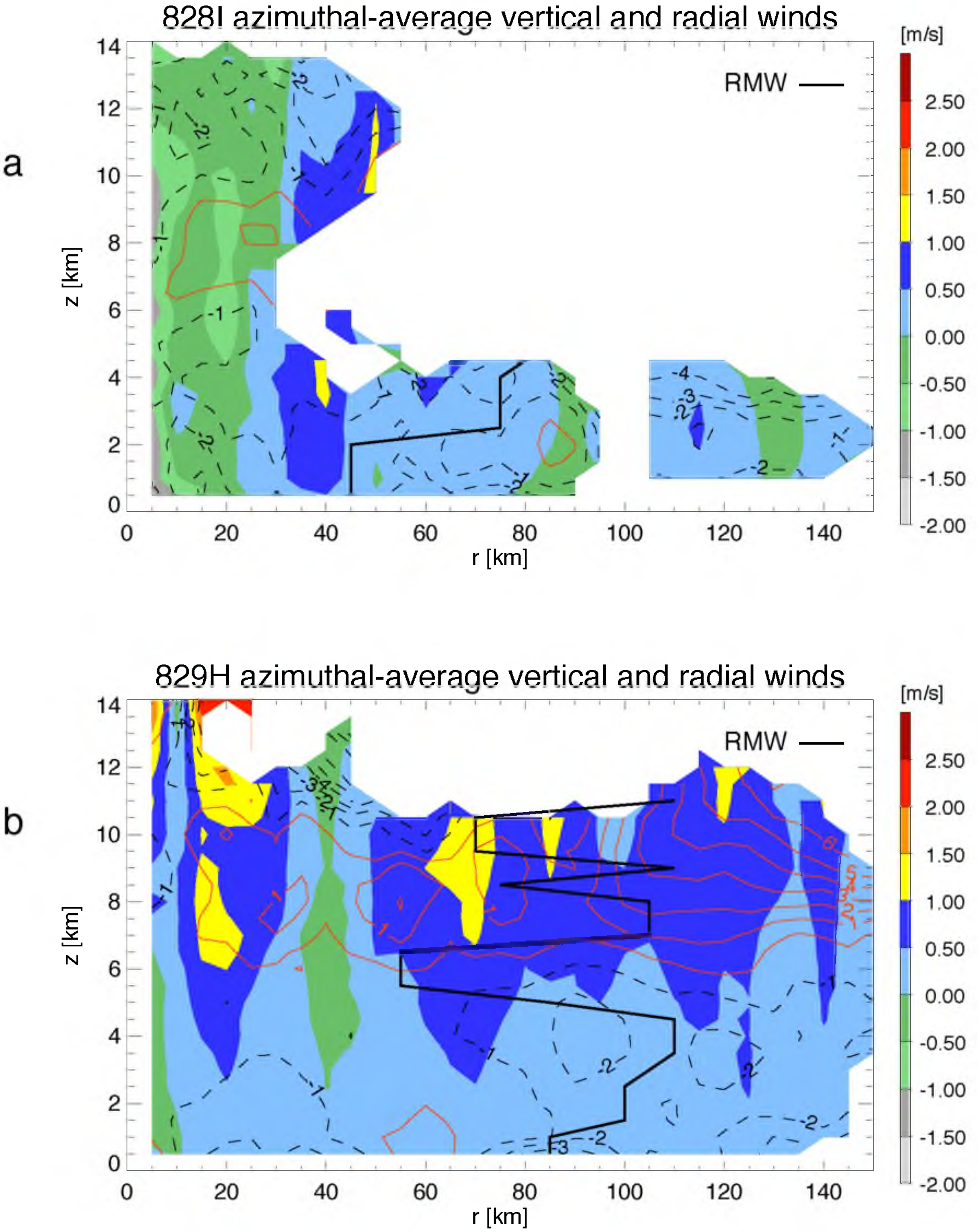

Figure 22. Merged analyses azimuthally averaged vertical (shaded) and radial (contour) winds for the 828I (a), 829H (b), 829I (c), 830H (d), and 830I (e) NOAA P3 flights. All values are in m s^{-1}.

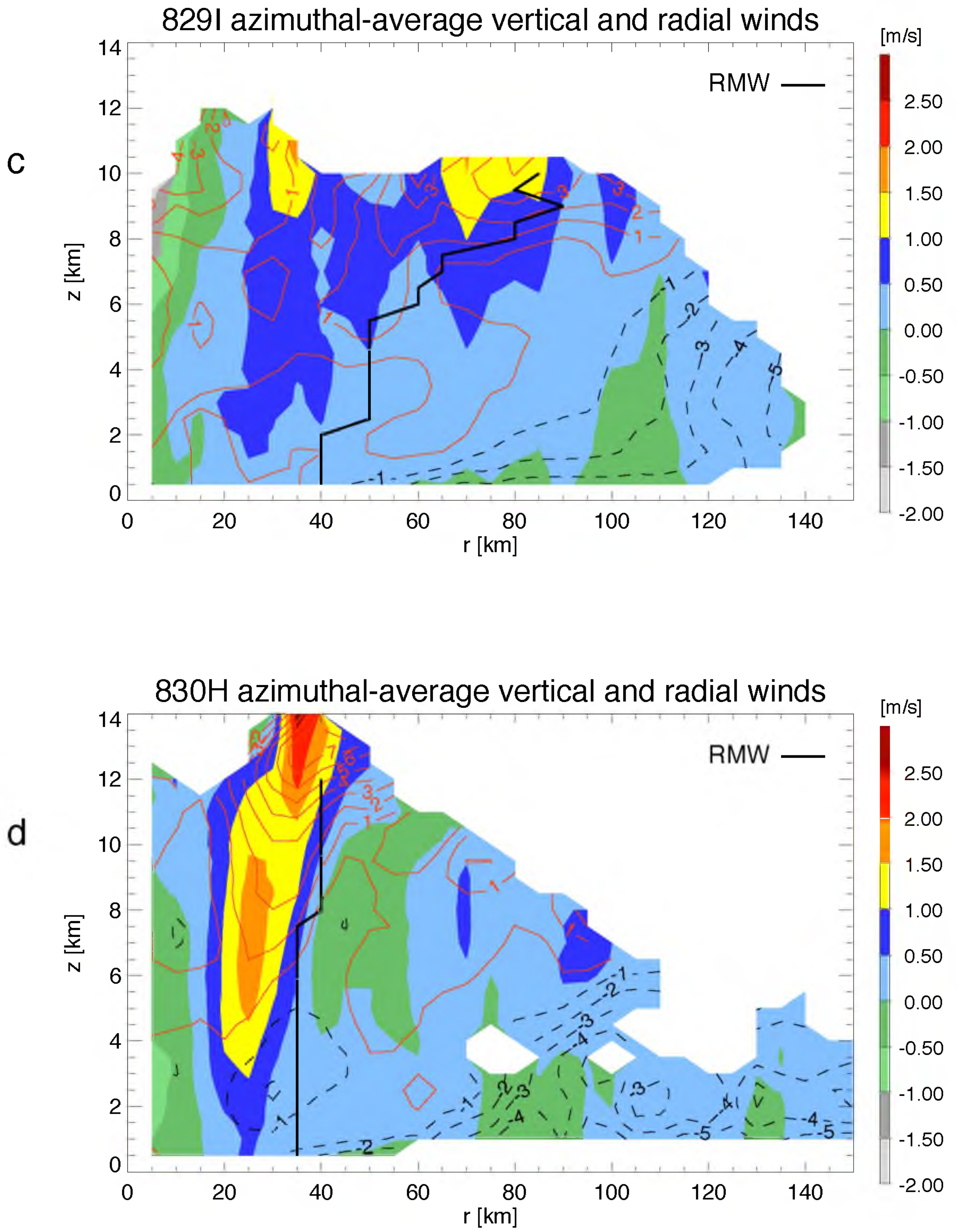

Figure 22. (Continued)

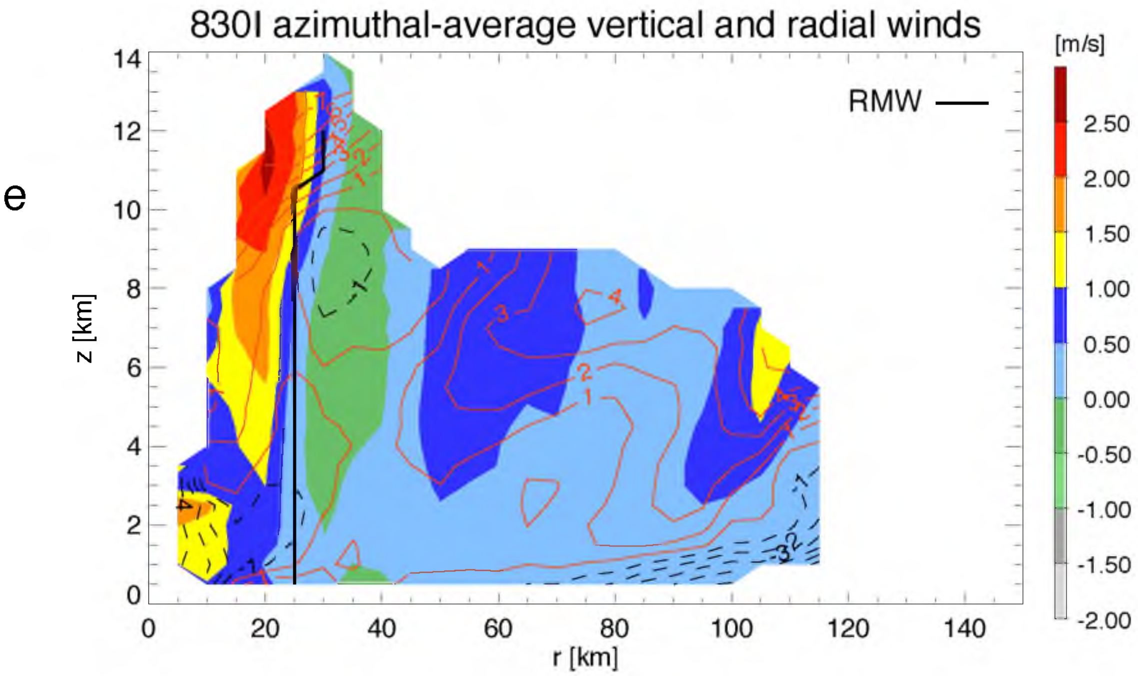

Figure 22. (Continued)

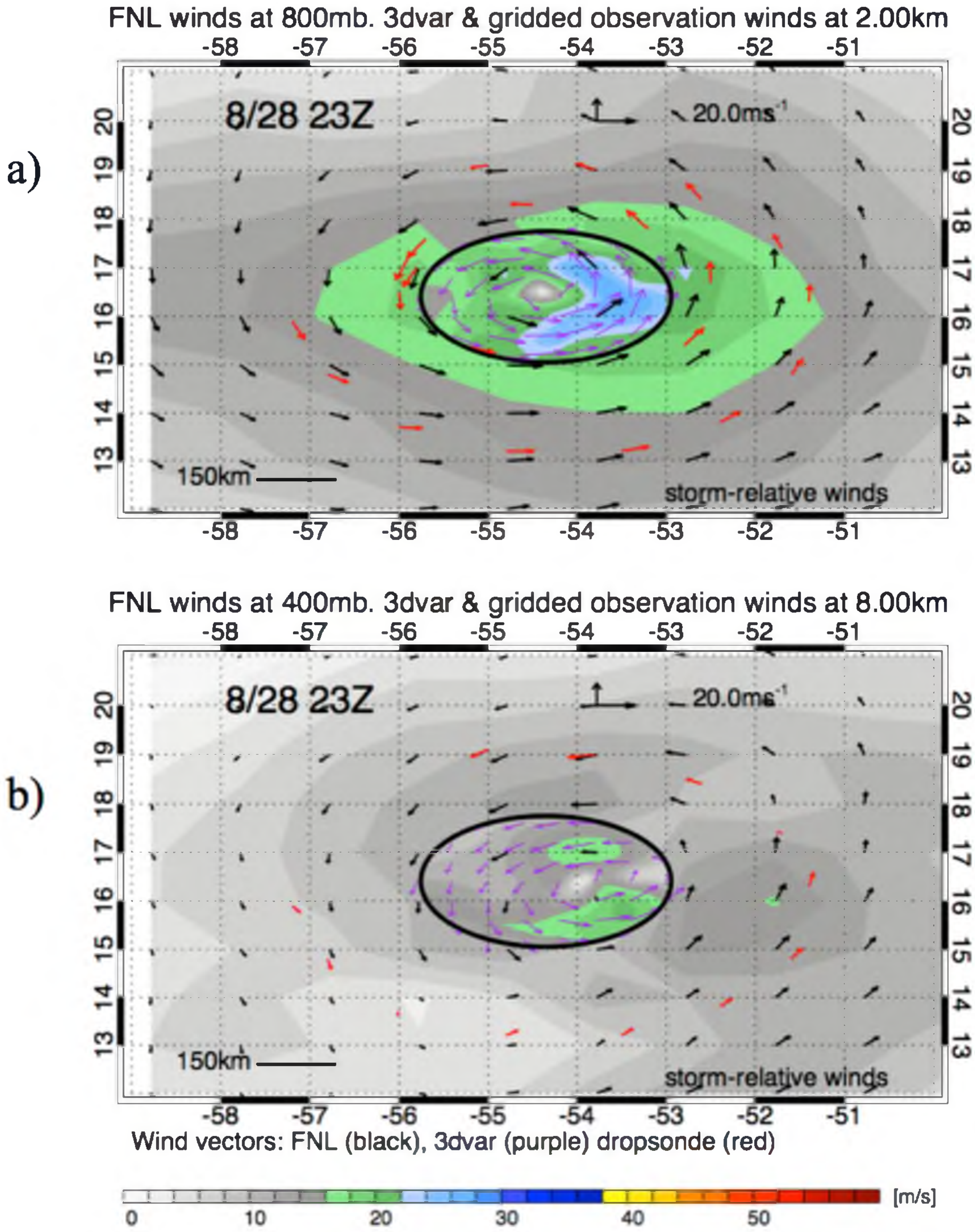
a)
FNL winds at 800mb. 3dvar & gridded observation winds at 2.00km
8/28 23Z
20.0ms⁻¹
150km
storm-relative winds
-58 -57 -56 -55 -54 -53 -52 -51
13 14 15 16 17 18 19 20
b)
FNL winds at 400mb. 3dvar & gridded observation winds at 8.00km
8/28 23Z
20.0ms⁻¹
150km
storm-relative winds
-58 -57 -56 -55 -54 -53 -52 -51
13 14 15 16 17 18 19 20
Wind vectors: FNL (black), 3dvar (purple) dropsonde (red)
[m/s]
0 10 20 30 40 50

Figure 23. Storm-relative winds at 2300 UTC August 28 (7 hours before RI onset) from 828I NMT-3dvar analysis (purple vectors, color shading inside 150-km radius), gridded dropsondes outside of 150-km radius (red vectors), and FNL (black vectors, color shading outside of 150km radius) at 2 km (a) and 8 km (b). FNL winds are renavigated from 0000 UTC August 29 analysis.

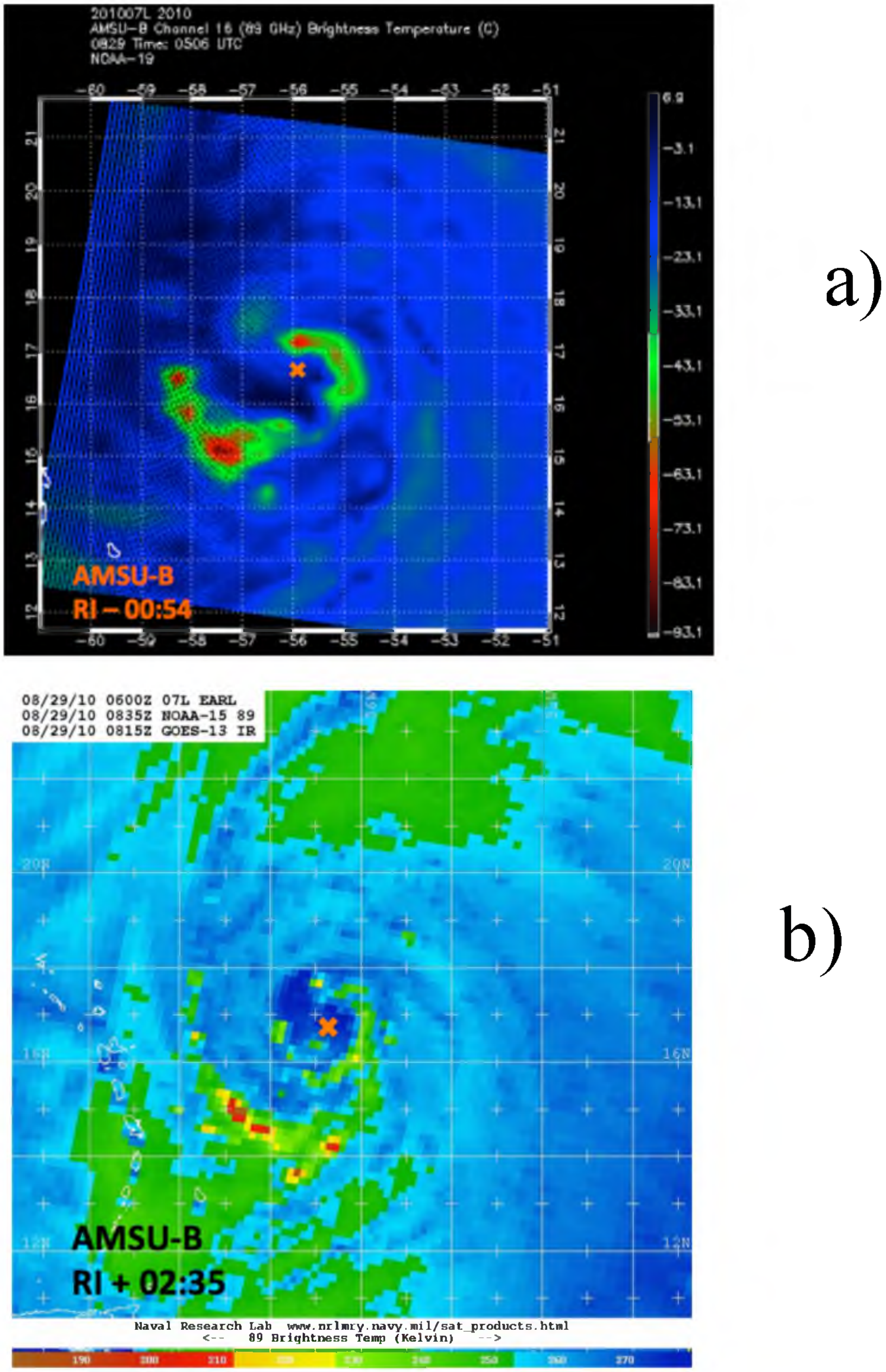
201007L 2010
AMSU-B Channel 16 (89 GHz) Brightness Temperature (C)
0829 Time: 0506 UTC
NOAA-19
AMSU-B
RI – 00:54
a)
08/29/10 0600Z 07L EARL
08/29/10 0835Z NOAA-15 89
08/29/10 0815Z GOES-13 IR
AMSU-B
RI + 02:35
Naval Research Lab www.nrlmry.navy.mil/sat_products.html
<-- 89 Brightness Temp (Kelvin) -->
b)

Figure 24. AMSU-B 89 GHz brightness temperatures at 0506Z (a) and 0835Z (b) August 29. HCF TC positions are indicated by orange ‘X’.

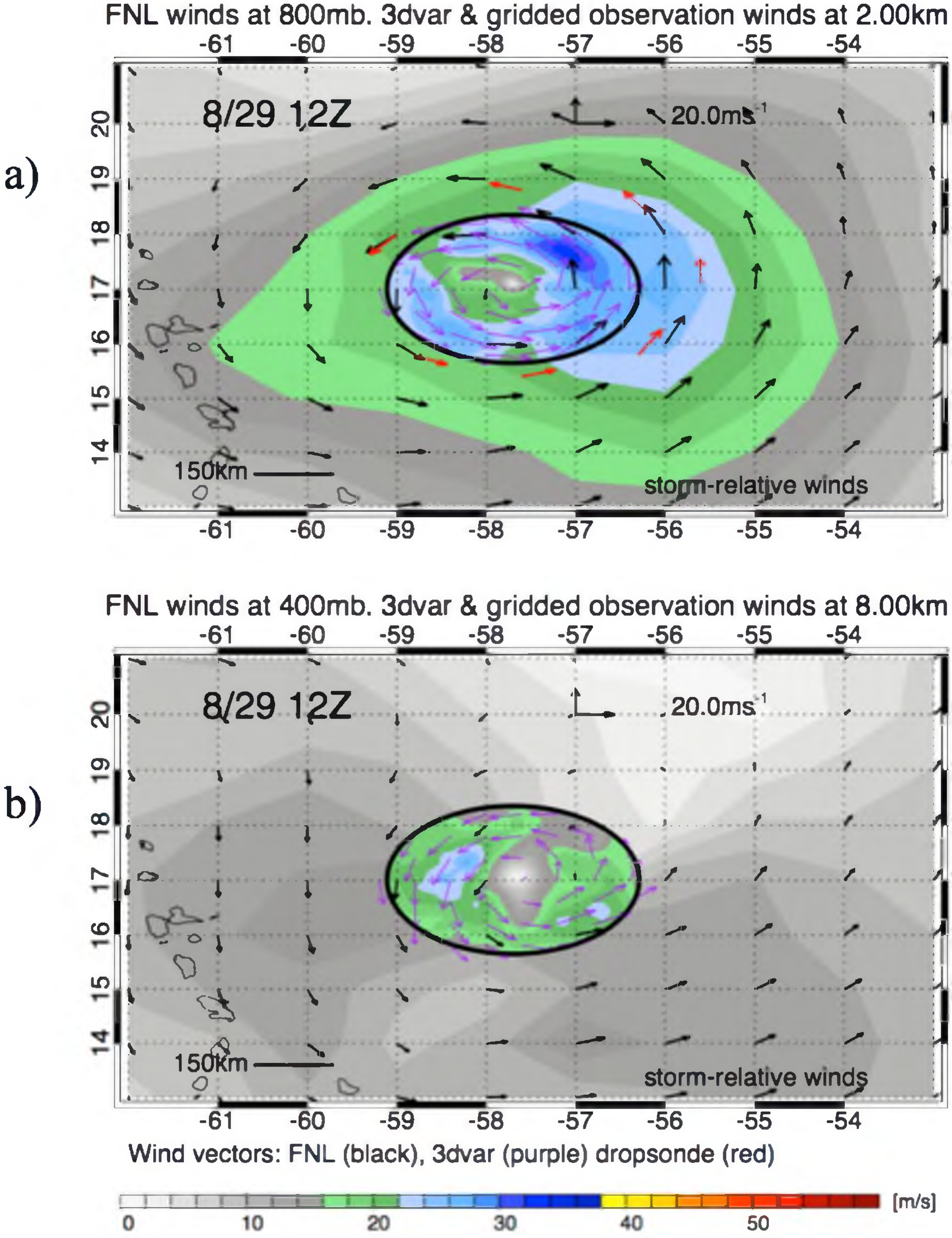
a)
FNL winds at 800mb. 3dvar & gridded observation winds at 2.00km
8/29 12Z
20.0ms⁻¹
150km
storm-relative winds
-61 -60 -59 -58 -57 -56 -55 -54
14 15 16 17 18 19 20
b)
FNL winds at 400mb. 3dvar & gridded observation winds at 8.00km
8/29 12Z
20.0ms⁻¹
150km
storm-relative winds
-61 -60 -59 -58 -57 -56 -55 -54
14 15 16 17 18 19 20
Wind vectors: FNL (black), 3dvar (purple) dropsonde (red)
0 10 20 30 40 50
[m/s]

Figure 25. Storm-relative winds at 1200 UTC August 29 (6 hours after RI onset) from 829H NMT-3dvar analysis (purple vectors, color shading inside 150-km radius), gridded dropsondes outside of 150-km radius (red vectors), and FNL (black vectors, color shading outside of 150km radius) at 2 km (a) and 8 km (b).

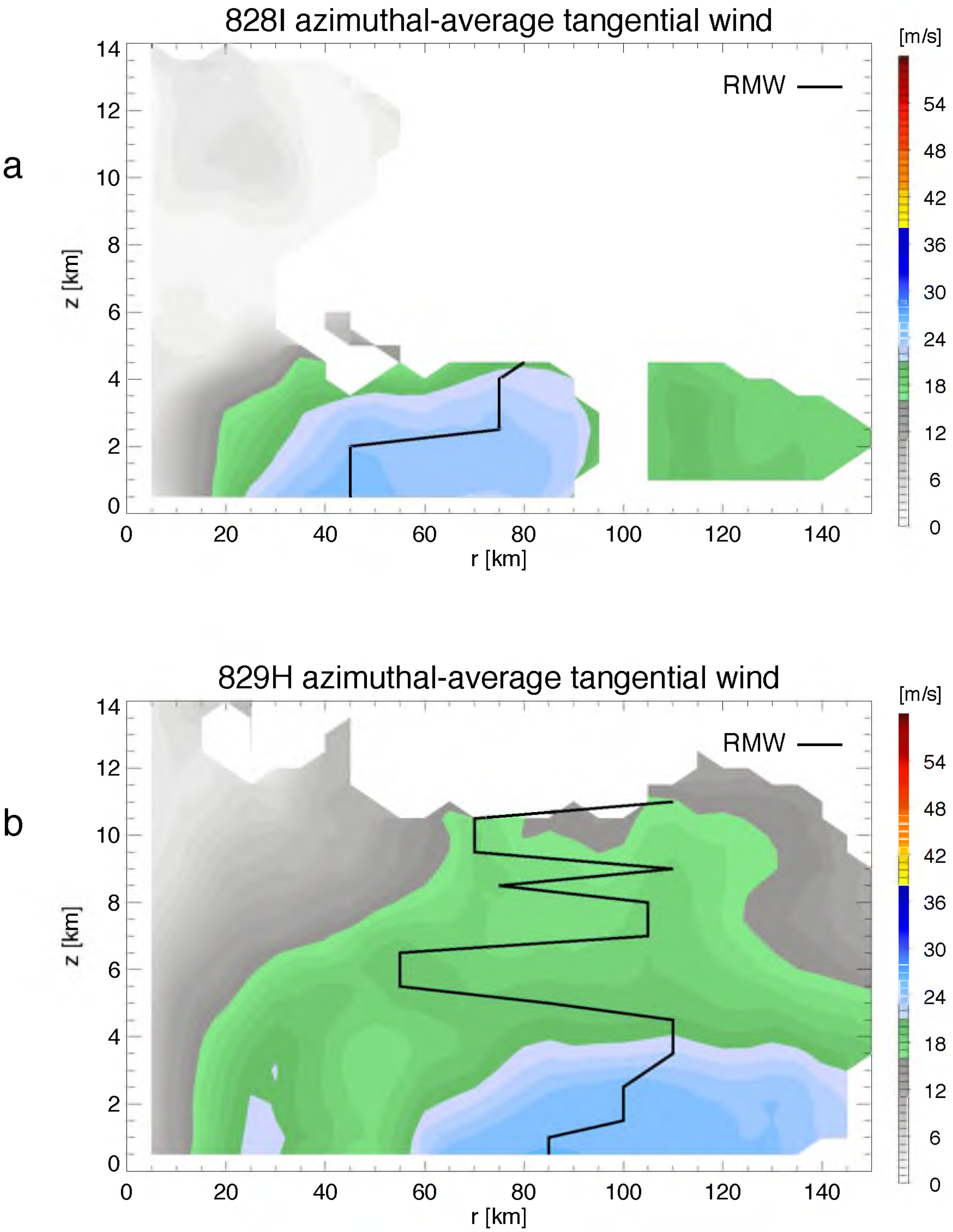

Figure 26. Merged analyses azimuthally averaged tangential winds from the 828I (a), 829H (b), 829I (c), 830H (d), and 830I (e) NOAA P3 flights.

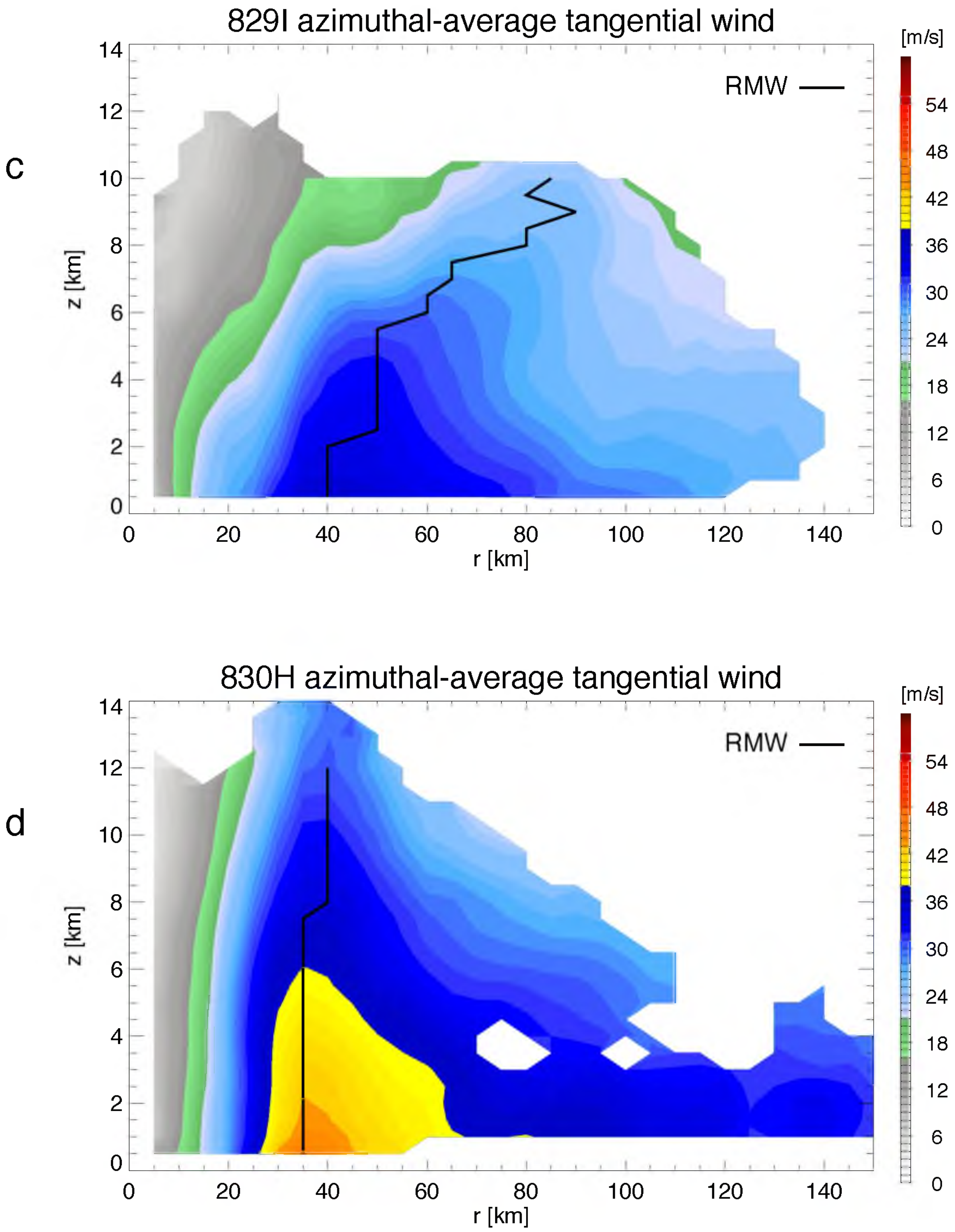

Figure 26. (Continued)

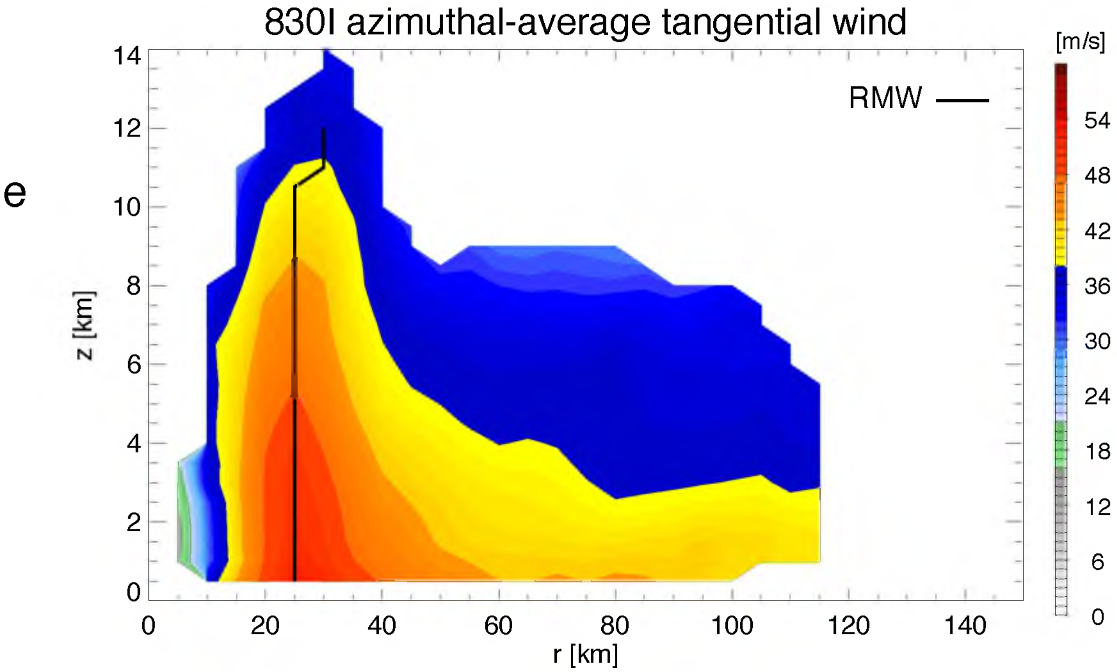

Figure 26. (Continued)

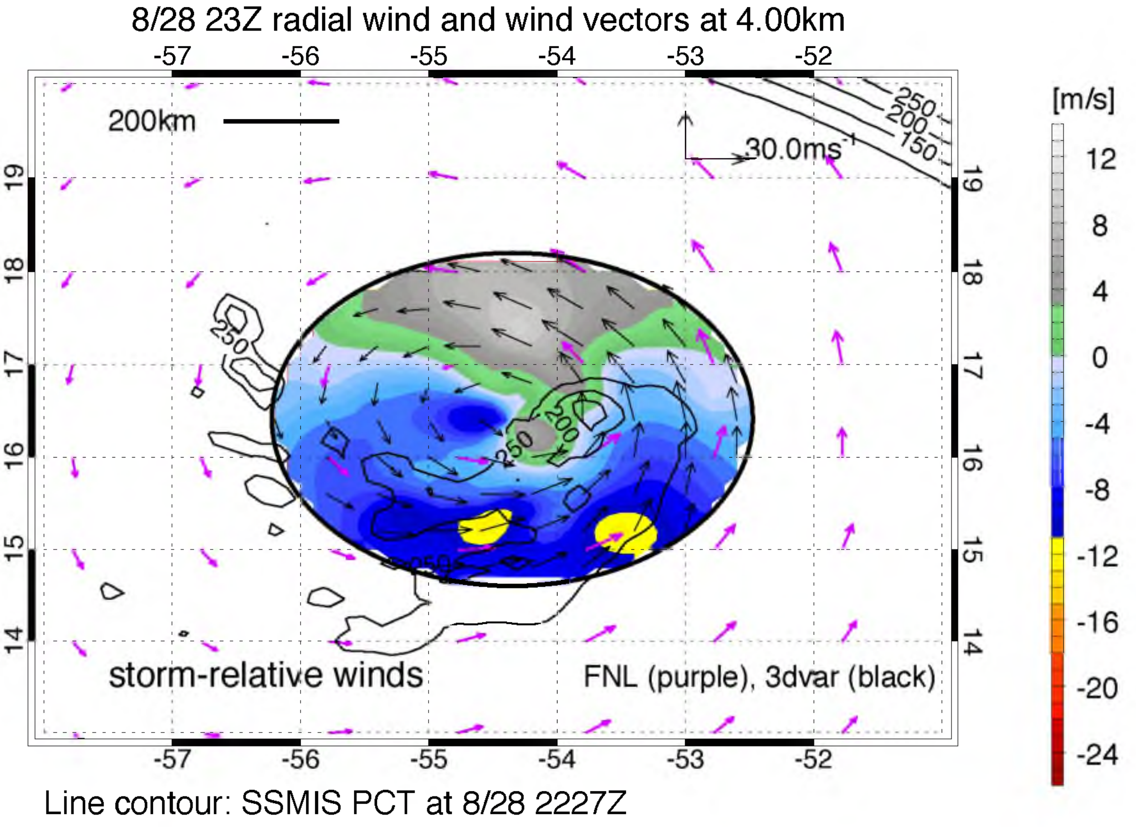
8/28 23Z radial wind and wind vectors at 4.00km
-57
-56
-55
-54
-53
-52
19
18
17
16
15
14
200km
30.0ms^{-1}
250
200
150
storm-relative winds
FNL (purple), 3dvar (black)
Line contour: SSMIS PCT at 8/28 2227Z
[m/s]
12
8
4
0
-4
-8
-12
-16
-20
-24

Figure 27. 828I NMT-3dvar analysis storm-relative winds and radial wind (shaded) at 2300 UTC August 28 (7 hours before start of RI), FNL winds renavigated from 0000 UTC August 29 analysis, and renavigated SSMIS 91GHz PCT at 2227 UTC August 28.

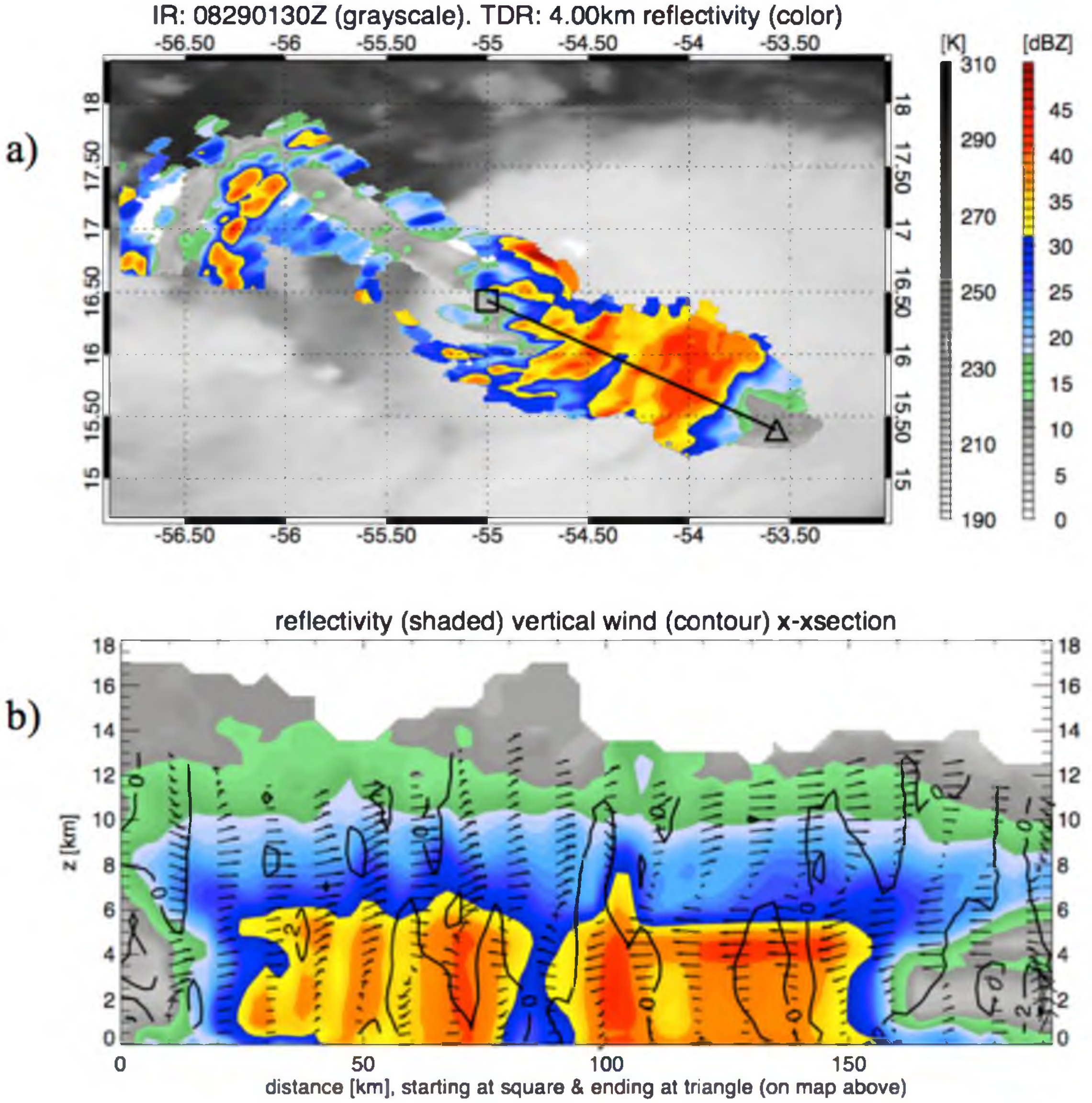

Figure 28. 828I TDR analysis plan view (a) and cross-section (b) at 0131 UTC August 29. Vectors are vector projection of TDR analysis storm-relative wind upon the cross-section plane.

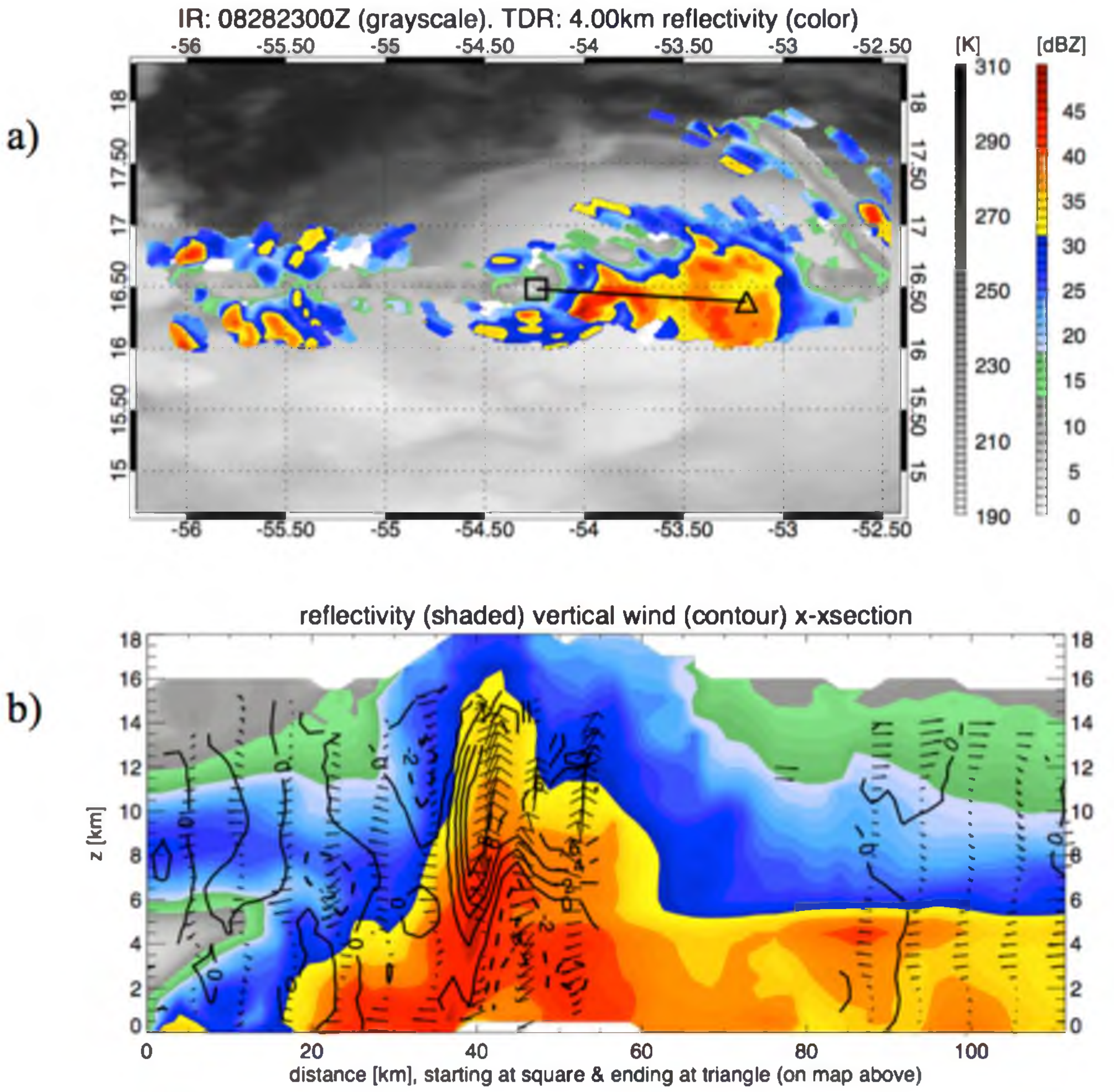

Figure 29. 828I TDR analysis plan view (a) and cross-section (b) at 2251 UTC August 28. Vectors are vector projection of TDR analysis storm-relative wind upon the cross-section plane.

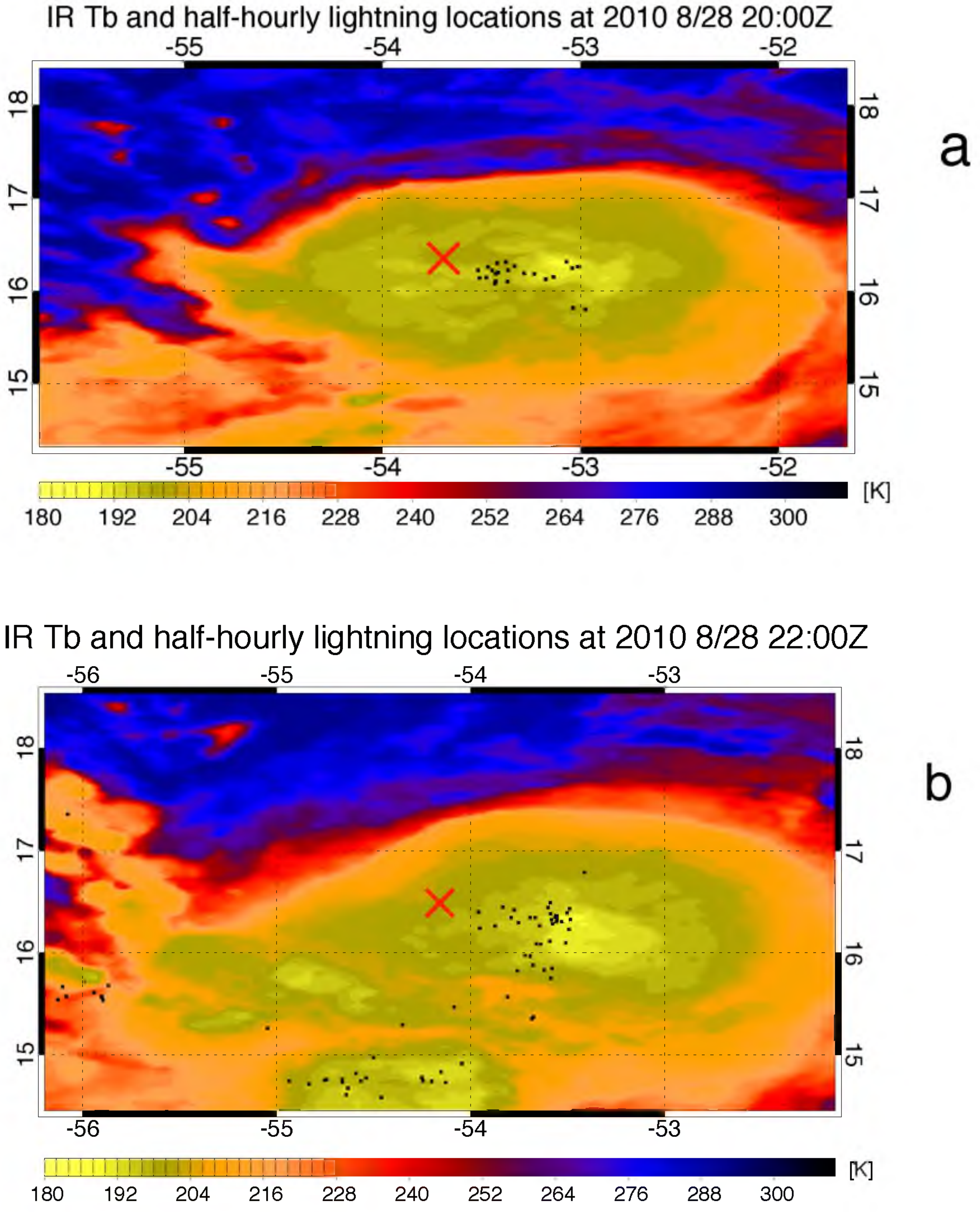
IR Tb and half-hourly lightning locations at 2010 8/28 20:00Z
-55
-54
-53
-52
18
17
16
15
a
[K]
180
192
204
216
228
240
252
264
276
288
300
IR Tb and half-hourly lightning locations at 2010 8/28 22:00Z
-56
-55
-54
-53
18
17
16
15
b
[K]
180
192
204
216
228
240
252
264
276
288
300

Figure 30. GOES IR T_b (shaded) and half-hourly lightning locations (dots) at 2000 UTC August 28 (a), 2200 UTC August 28 (b), 0000 UTC August 29 (c), 0100 UTC August 29 (d), 0200 UTC August 29 (e), and 0400 UTC August 29 (f).

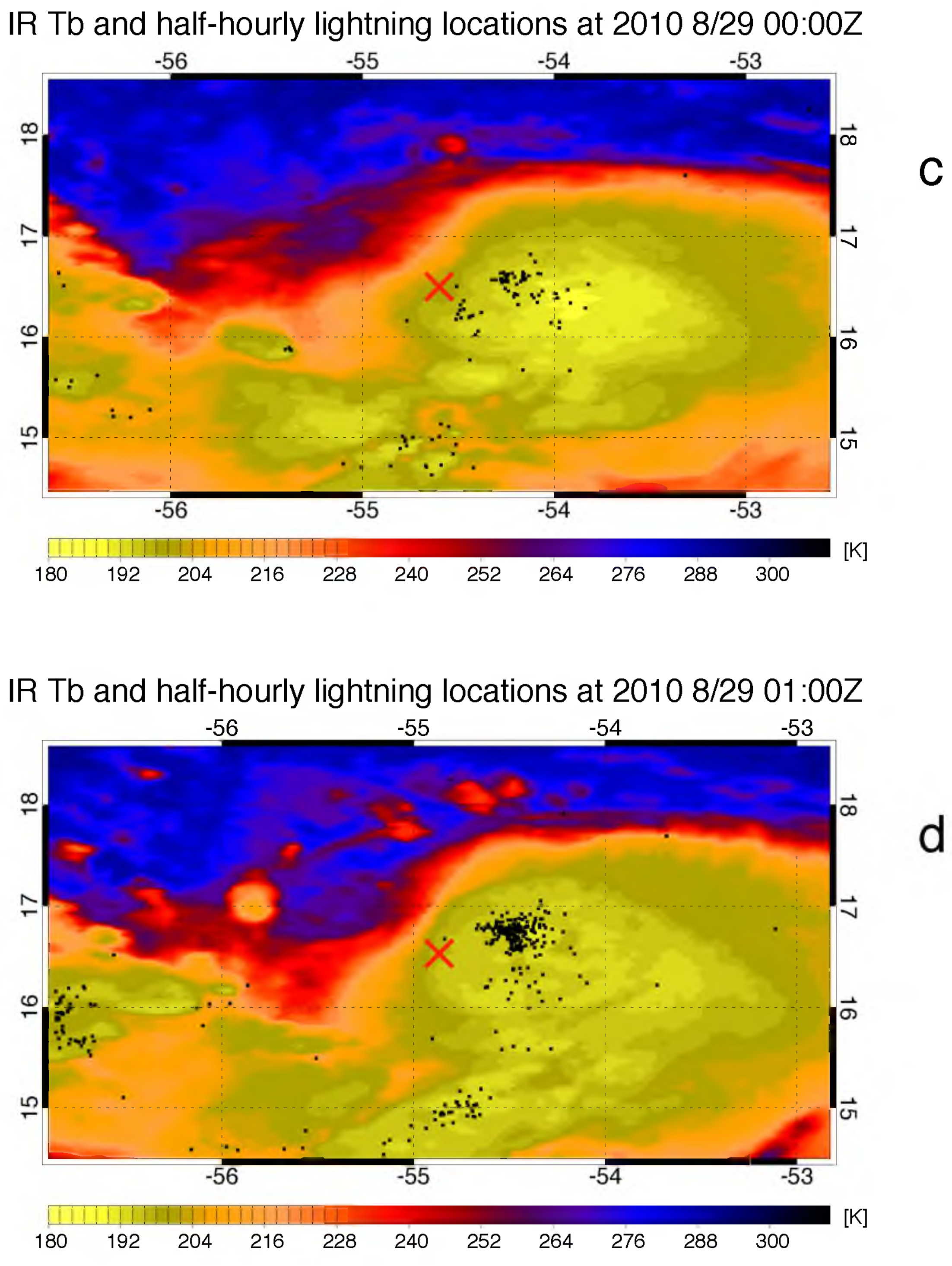
IR Tb and half-hourly lightning locations at 2010 8/29 00:00Z
-56
-55
-54
-53
18
17
16
15
c
[K]
180
192
204
216
228
240
252
264
276
288
300
IR Tb and half-hourly lightning locations at 2010 8/29 01:00Z
-56
-55
-54
-53
18
17
16
15
d
[K]
180
192
204
216
228
240
252
264
276
288
300

Figure 30. (Continued)

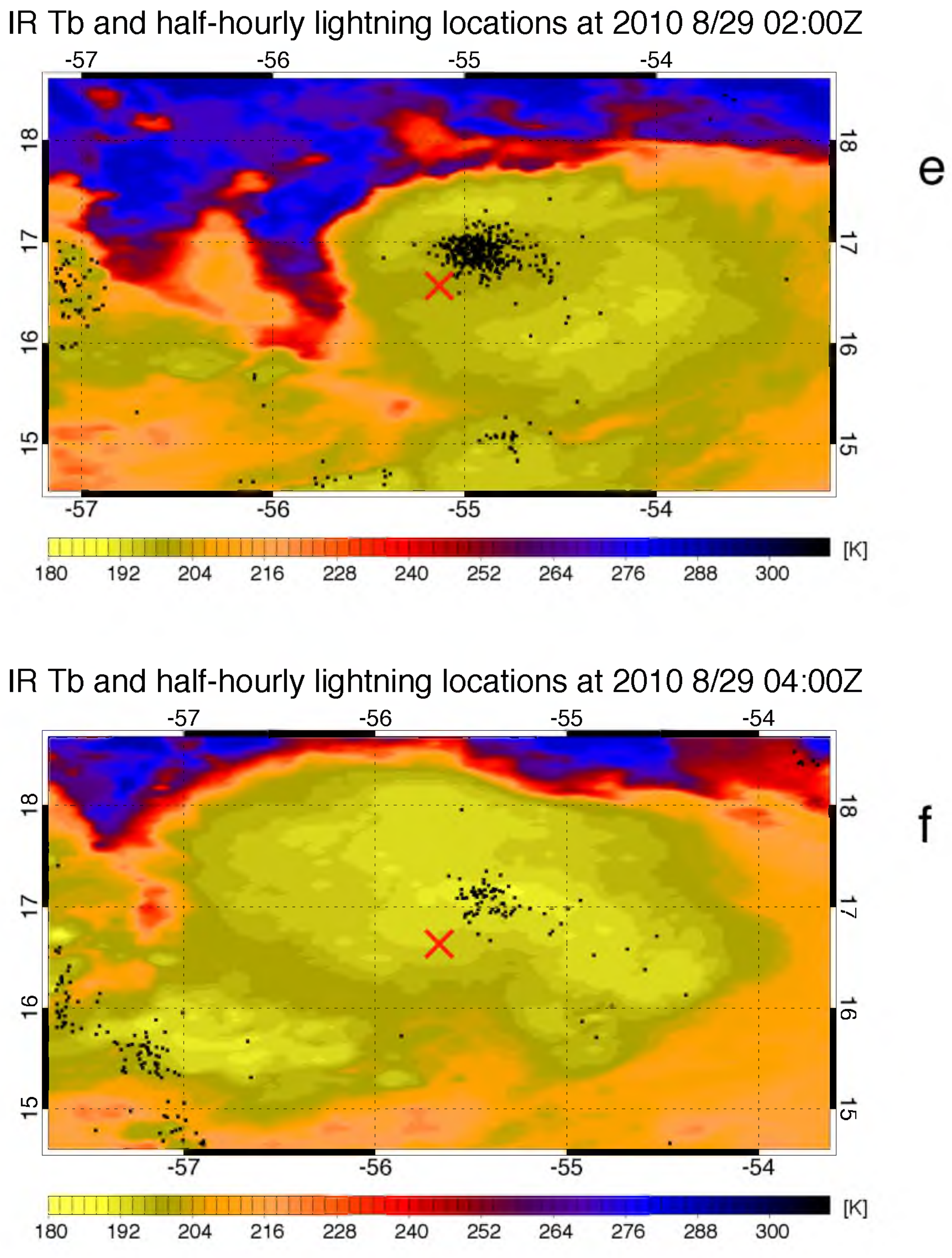
IR Tb and half-hourly lightning locations at 2010 8/29 02:00Z
-57
-56
-55
-54
18
17
16
15
e
[K]
180
192
204
216
228
240
252
264
276
288
300
IR Tb and half-hourly lightning locations at 2010 8/29 04:00Z
-57
-56
-55
-54
18
17
16
15
f
[K]
180
192
204
216
228
240
252
264
276
288
300

Figure 30. (Continued)

CHAPTER 6

DISCUSSION

6.1. Summary

This thesis has documented the environmental conditions, precipitation characteristics, and kinematic structure before, during, and following the 36-hour period of Earl's RI. This study employed a combination of global analysis data, IR and passive microwave satellite brightness temperatures, in-situ aircraft measurements, lightning data, and Doppler radar wind and reflectivity analyses.

Between 24–48 hours before the onset of RI, Earl slowly intensified in the presence of low shear and SSTs sufficiently high for RI. The delay in the onset of RI is likely explained by the disorganization and occasional complete lack of inner-core convection during most of this time. By the end of this time period, the inner-core cold-cloud precipitation organized into a feature resembling a developing eyewall. The appearance of a cyan ring (Kieper and Jiang 2012) at 0413 UTC August 28 (26 hours before RI onset) suggests that RI would have begun closer to that time if the vertical shear had not increased.

Deep layer shear increased to moderate levels between 12–24 hours before the onset of RI, causing pronounced cloud and deep precipitation asymmetries and likely causing the vortex tilt observed 4–9 hours before RI onset. Following the increase in shear, the inner-core cold-cloud precipitation organized into a region of intense convection in the eastern and southern quadrants, and this convective 'burst' persisted until ~2 hours before the start of RI. Lightning data indicate that a large portion of the convection in this burst was located within the RMW. Between 2–6 hours before the onset of RI, an outbreak of inner-core lightning occurred as the region of intense convection migrated to the northeastern and northern quadrants.

An examination of the dual-Doppler winds 4–9 hours before RI onset suggests that the increased shear led to the creation of a prominent stationary rainband (Willoughby et al. 1984) and a region of strong mid-tropospheric inflow associated with this rainband. Dual-Doppler cross-sections indicate this midlevel inflow ventilated the inner-core of Earl. A comparison of this feature with the rainband circulation shown in Didlake and Houze (2013) suggests that the region of midlevel inflow also resulted in increased tangential wind well outside of the RMW, leading to the doubling of the RMW observed 3–8 hours after the onset of RI. This combination of effects suggests that although forced subsidence (Heymsfield et al. 2001; Guimond et al. 2010) and local vorticity generation (Nguyen et al. 2008) may have occurred in the intense convection 4-9 hours prior to RI, the vortex-scale kinematic structure may have prevented rapid intensification during that time period.

On the other hand, the migration of the burst around the TC center might have led to the onset of RI. AMSU-B images indicate an increasing trend in near-inner-core cold-cloud precipitation symmetry soon after this convective migration, suggesting that the migration of convection into the northern and northeastern quadrants may have caused these increases in cold-cloud precipitation symmetry. Alternatively, the evolution of 8-km TDR analysis winds 4–9 hours before RI onset (Rogers et al. 2014) suggests that the migration of convection into the northeastern and northern quadrants may have coincided with the precession of the upper-level vortex into these same (upshear) quadrants, and this vortex precession may have also contributed to reduced vortex tilt. The convective migration, possible vortex precession, or both of these factors likely initiated a positive feedback between increasing deep precipitation symmetry and increasing vortex alignment, and this feedback likely led to the increased vortex alignment and weakened azimuthally averaged midlevel inflow that prevailed 3–8 hours after the onset of RI.

Another convective burst occurred approximately 6–12 hours after the onset of RI. This convective burst was associated with a lower frequency of intense convection than the one before RI onset, but it occurred in the presence of an aligned mid- and upper-level vortex, and most of the intense convection was located within the RMW. In the simulation of Chen and Zhang (2013), forced subsidence from strong convective towers appeared to contribute more effectively to the warm core after the development of an inertially stable upper-level cyclonic circulation. This post-RI-onset convective burst in Earl probably contributed more to TC strengthening than the burst before RI onset because of the increase in mid- and upper-level inertial stability provided by the vortex alignment, and the radial location of the burst.

In the later stages of RI and following a decrease in shear, a convective ring eyewall formed and contracted. Throughout its formation and contraction, the eyewall convective ring was located along or within the 8-km RMW, most of the strongest convection occurred within the RMW, and dual-Doppler fields indicate that the strongest azimuthally averaged ascent was located within the RMW as well. This favorable convective and kinematic structure persisted through at least 40 hours after the onset of

RI. This inner-core structure probably produced the continued decreases in MSLP up to 48 hours after RI onset. The wind speed increases ended 36 hours after the onset of RI. Dual-Doppler analyses and PMW images suggest that the formation of a secondary eyewall caused the wind speed to reach steady state, and the strengthening of this outer eyewall likely ended the trend of decreasing MSLP.

6.2. Conclusions

None of the inner-core precipitation characteristics of cold-cloud precipitation coverage, convective intensity, or coverage of intense convection appear to be the sole cause of the rapid intensification (RI) of Earl. Instead, the data from Earl suggest that different aspects of the core precipitation structure become relatively important at different times relative to the RI.

An axisymmetric precipitation ring did not cause the onset of RI in Earl. However, an increasing trend in core cold-cloud precipitation symmetry does appear to lead to the onset of RI and contribute to the early stages of RI, and the later stages of RI proceed via the formation and contraction of a convective ring. Axisymmetric convective rings only appeared during periods of low shear, in agreement with previous studies that indicate that the axisymmetric ring mode of RI tends to occur in favorable environmental conditions (Harnos and Nesbitt 2011; Kieper and Jiang 2012).

An intense convective burst occurred before RI onset, but an examination of the precipitation and wind fields suggests that the strength of this burst alone did not cause the onset of RI. Instead, the dual-Doppler, lightning, and microwave data suggest that a necessary condition for the onset of RI was an increasing trend in cold-cloud precipitation symmetry following the migration of inner-core convection into the northeastern and northern quadrants of the storm within a few hours before RI onset.

Overall, the evolution of convection in Earl reaffirms the importance of the radial distribution of convection. Throughout the RI period, the strongest convection tends to be located within the radius of maximum wind (RMW). Dual-Doppler data indicate that this predominance of convection within the RMW occurs because a significant portion of the ascending component of the secondary circulation is located within the RMW during the early stages of RI, and nearly the entire ascending leg is confined within the RMW during the later stages of RI.

The results presented here and in Rogers et al. (2013a) indicate the potential use of the location of strong convection relative to the RMW in TC intensity prediction. The RMW of Earl was highly slanted during part of the RI, and only considering the RMW at low levels could lead to the false impression that most of the strong convection was occurring outside of the RMW at those times. Any future TC guidance based on the radial distribution of convection should consider the location of the RMW at multiple levels. The real-time NOAA P3 dual-Doppler retrievals could serve that purpose. Alternatively, hurricane reconnaissance flights could be flown at both lower and upper levels, and the RMW slant could be inferred from the upper-level and lower-level aircraft in situ data.

REFERENCES

Abarca, S. F., K. L. Corbosiero, and T. J. Galarneau Jr., 2010: An evaluation of the Worldwide Lightning Location Network (WWLLN) using the National Lightning Detection Network (NLDN) as ground truth. *J. Geophys. Res.*, **115**, D18206, doi:10.1029/2009JD013411.

——, and D. Vollaro, 2011: The World Wide Lightning Location Network and convective activity in tropical cyclones. *Mon. Wea. Rev.*, **139**, 175–191.

Ashcroft, P., and F. J. Wentz., 2013: *AMSR-E/Aqua L2A Global Swath Spatially-Resampled Brightness Temperatures*. Version 3. Boulder, Colorado USA: NASA DAAC at the National Snow and Ice Data Center. http://dx.doi.org/10.5067/AMSR-E/AE_L2A.003.

Beven, J., cited 2014: Hurricane Wilma discussion number 14. [Available online at http://www.nhc.noaa.gov/archive/2005/dis/al242005.discus.014.shtml?]

Black, R. A., and J. Hallett, 1999: Electrification of the hurricane. *J. Atmos. Sci.*, **56**, 2004–2028.

Braun, S. A., and coauthors, 2013: NASA's Genesis and Rapid Intensification Processes (GRIP) field experiment. *Bull. Amer. Meteor. Soc.*, **94**, 345–363.

Cangiolosi, J. P, 2011: Tropical cyclone report Hurricane Earl (AL072010). [Available online at http://www.nhc.noaa.gov/pdf/TCR-AL072010_Earl.pdf].

Cecil, D. J., and E. J. Zipser, 1999: Relationships between tropical cyclone intensity and satellite-based indicators of inner core convection: 85-GHz ice-scattering signature and lightning. *Mon. Wea. Rev.*, **127**, 103–123.

Chan, J. C. L., and J. D. Kepert, 2010: *Global perspectives on tropical cyclones— from science to mitigation.* World Scientific Publishing Co., 436pp.

Chen, H., and D. L. Zhang, 2013: On the rapid intensification of Hurricane Wilma (2005). Part II: Convective bursts and the upper-level warm core. *J. Atmos. Sci,* **70**, 146–162.

Chen, S. S., J. A. Knaff, and F. D. Marks, 2006: Effects of vertical wind shear and storm motion on tropical cyclone rainfall asymmetries deduced from TRMM. *Mon. Wea.*

Rev., **134**, 3190–3208.

Corbosiero, K. L., and J. Molinari, 2002: The effects of vertical wind shear on the distribution of convection in tropical cyclones. *Mon. Wea. Rev.*, **130**, 2110–2123.

——, J. Molinari, S. Stevenson, and D. Vollaro, 2013: The unusual beginning (and ending) of rapid intensification in Hurricane Earl (2010). *Proceedings*, *HS3 Science Team & Deployment Preparation Meeting*, Mountain View, CA, May 7–9 2013. [https://espo.nasa.gov/missions/hs3/content/HS3_Science_Presentations]

DeMaria, M., 1996: The effect of vertical shear on tropical cyclone intensity change. *J. Atmos. Sci.*, **53**, 2076–2088.

——, and J. Kaplan 1994: Sea surface temperature and the maximum intensity of Atlantic tropical cyclones. *J. Climate*, **7**, 1324–1334.

——, M. Mainelli, L. K. Shay, J. A. Knaff, and J. Kaplan, 2005: Further improvements to the Statistical Hurricane Intensity Prediction Scheme (SHIPS). *Wea. Forecasting*, **20**, 531–543.

——, R. T. DeMaria, J. A. Knaff, and D. Molenar, 2012: Tropical cyclone lightning and rapid intensity change. *Mon. Wea. Rev.*, **140**, 1828–1842.

Didlake, A. C., and R. A. Houze, 2013: Dynamics of the stratiform Sector of a tropical cyclone rainband. *J. Atmos. Sci.*, **70**, 1891–1911.

Dunion, J. P., and C. S. Velden, 2004: The impact of the Saharan air layer (SAL) on Atlantic tropical cyclone activity. *Bull. Amer. Meteor. Soc.* **85**, 353–364.

Frank, W. M., and E. A. Ritchie, 2001: Effects of vertical wind shear on the intensity and structure of numerically simulated hurricanes. *Mon. Wea. Rev.*, **129**, 2249–2269.

Gallina, G. M., and C. Velden, 2002: Environmental vertical wind shear and tropical cyclone intensity change utilizing enhanced satellite derived wind information. *Extended Abstracts*, *25th AMS Conf. on Hurr. and Trop. Meteor.*, San Diego, CA, Amer. Meteor. Soc., 172–173.

Gamache, J. F., F. D. Marks, and F. Roux, 1995: Comparison of three airborne doppler sampling techniques with airborne in situ wind observations in Hurricane Gustav (1990). *J. Atmos. Oceanic Technol.*, **12**, 171–181.

——, P. P. Dodge, and N. F. Griffin, 2008: Automatic quality control and analysis of airborne Doppler data: Real-time applications, and automatically post-processesd analysis for research. *Extended Abstracts*, *28th AMS Conf. on Hurr. and Trop. Meteor.*, Orlando, FL, Amer. Meteor. Soc.

Guimond, S. R., G. M. Heymsfield, and F. J. Turk, 2010: Multiscale observations of Hurricane Dennis (2005): The effects of hot towers on rapid intensification. *J. Atmos. Sci.*, **67**, 633–654.

Harnos, D. S., and S. W. Nesbitt, 2011: Convective structure in rapidly intensifying tropical cyclones as depicted by passive microwave instruments. *Geophys. Ress. Lett.*, **38,** L07805, doi: 10.1029/2011GL047010.

Hendricks, E. A., M. S. Peng, B. Fu, and T. Li, 2010: Quantifying environmental control on tropical cyclone intensity change. *Mon. Wea. Rev.*, **138**, 3243–3271.

Hennon, P. A., 2006: The role of the ocean in convective burst initiation: Implications for iropical cyclone intensification. Dissertation, Ohio State University, 162pp.

Heymsfield, G. M., J. B. Halverson, J. Simpson, L. Tian, and T. P. Bui, 2001: ER-2 Doppler radar investigations of the eyewall of Hurricane Bonnie during the Convection and Moisture Experiment-3. *J. Appl. Meteor.*, **40**, 1310–1330.

Houze, R. A., S. S. Chen, J. Moore, R. Dirks, and J. Meitin, 2005: The Hurricane Rainband and Intensity Change Experiment (RAINEX) operations plan. 53pp.

——, W. C. Lee, and M. M. Bell, 2009: Convective contribution to the genesis of Hurricane Ophelia (2005). *Mon. Wea. Rev.*, **137**, 2778–2800.

Hurricane Intensity Research Working Group, 2006: Majority Report. [Available online at http://www.sab.noaa.gov/Reports/HIRWG_final73.pdf]

Hutchins, M. L., R. H. Holzworth, C. J. Rodger, S. Heckman, and J. B. Brundell, 2012: WWLLN absolute detection efficiencies and the global lightning source function. *Proc., EGU General Assembly 2012,* Vienna, Austria, European Geosciences Union.

Jiang, H., 2012: The relationship between tropical cyclone intensity change and the strength of inner-core convection. *Mon. Wea. Rev.*, **140**, 1164–1176.

——, and E. M. Ramirez, 2013: Necessary conditions for tropical cyclone rapid intensification as derived from 11 years of TRMM data. *J. Climate*, **26**, 6459–6470.

Jones, S. C., 1995: The evolution of vortices in vertical shear. I: Initially baratropic vortices. *Quart. J. Roy. Meteor. Soc.* **121,** 821–851.

Jones, T. A., D. Cecil, and M. DeMaria, 2006: Passive-microwave-enhanced Statistical Hurricane Intensity Prediction Scheme. *Wea. Forecasting*, **21**, 613–635.

Kaplan, J., and M. Demaria, 2003: Large-scale characteristics of rapidly intensifying tropical cyclones on the North Atlantic basin. *Wea. Forecasting*, **18,** 1093–1108.

——, M. DeMaria, and J. A. Knaff, 2010: A revised tropical cyclone rapid intensification index for the Atlantic and Eastern North Pacific basins. *Wea. Forecasting*, **25**, 220–241.

Kelley, O. A., J. Stout, and J. B. Halverson, 2004: Tall precipitation cells in tropical cyclones eyewalls are associated with tropical cyclone intensification. *Geophys. Res. Lett.*, **31**, L24112, doi:10.1029/2004GL021616.

Kieper, M., and H. Jiang, 2012: Predicting tropical cyclone rapid intensification using the 37 GHz ring pattern identified from passive microwave measurements. *Geophys. Res. Lett.*,**39**, L13804,doi:10.1029/2012GL052115.

Liu, C., E. J. Zipser, D. J. Cecil, S. W. Nesbitt, and S. Sherwood, 2008: A cloud and precipitation feature database from nine years of TRMM observations. *J. Appl. Meteor.*, **47**, 2712–2728.

——, D. Cecil, and E.J. Zipser, 2011: Relationships between lightning flash rates and passive microwave brightness temperatures at 85 and 37 GHz over the tropics and subtropics. *J. Geophys. Res.*, **116**, D23108, doi:10.1029/2011JD016463.

Lopez Carrillo, C., and D. J. Raymond, 2011: Retrieval of three-dimensional wind fields from Doppler radar data using an efficient two-step approach. *Atmos. Meas. Tech.*, **4**, 2717–2733.

Marks, F. D, and L. K Shay, 1998: Landfalling tropical cyclones: Forecast problems and associated research opportunities. *Bull. Amer. Meteor. Soc.*, **79**, 305–523.

Merrill, R. T., 1988: Environmental influences on hurricane intensification. *J. Atmos. Sci.*, **45**, 1678–1687.

Molinari, J., P. Dodge, D. Vollaro, and K. L. Corbosiero, Frank Marks, 2006: Mesoscale aspects of the downshear reformation of a tropical cyclone. *J. Atmos. Sci.*, **63**, 341–354.

——, and D. Vollaro, 2010: Rapid intensification of a sheared tropical storm. *Mon. Wea. Rev.*, **138**, 3869–3885.

National Hurricane Center, cited 2014: National Hurricane Center forecast verification. [Available online at http://www.nhc.noaa.gov/verification/verify5.shtml]

Nguyen, L. T, and J. Molinari; 2012: Rapid intensification of a sheared, fast-moving hurricane over the Gulf Stream. *Mon. Wea. Rev.*, **140**, 3361–3378.

Nguyen, S. V, R. K Smith, and M. T Montgomery, 2008: Tropical-cyclone intensification and predictability in three dimensions. *Q. J. R. Meteorol. Soc.*, **128**, 2641–2661.

Nolan, D. S., Y. Moon, and D. P. Stern, 2007: Tropical cyclone intensification from asymmetric convection: Energetics and efficiency. *J. Atmos. Sci.*, **64**, 3377–3405.

Pendergrass, A. G., and H. E. Willoughby, 2009: Diabatically induced secondary flows in tropical cyclones. Part I: Quasi-steady forcing. *Mon. Wea. Rev.*, **137**, 805–821.

Reasor, P. D., M. D. Eastin, and J. F. Gamache, 2009: Rapidly intensifying Hurricane Guillermo (1997). Part I: Low-wavenumber structure and evolution. *Mon. Wea. Rev.*, **137,** 603–631.

——, R. Rogers, and S. Lorsolo, 2013: Environmental flow impacts on tropical cyclone structure diagnosed from airborne Doppler radar composites. *Mon. Wea. Rev.*, **141**, 2949–2969.

Reinhart, B., and coauthors, 2014: Understanding the relationships between lightning, cloud microphysics, and airborne radar-derived storm structure during Hurricane Karl (2010). *Mon. Wea. Rev*, **142**, 590–605.

Rhome, J. R., C. A. Sisko, and R. D. Knabb, 2006: On the calculation of vertical shear: An operational perspective. *Extended Abstracts, 27th AMS Conf. on Hurr. and Trop. Meteor.*, Monterey, CA, Amer. Meteor. Soc.

Riemer, M., Montgomery, M. T., and M. E. Nicholls, 2010: A new paradigm for intensity modification of tropical cyclones: Thermodynamic impact of vertical wind shear on the inflow layer. *Atmos. Chem. Phys.*, **10,** 3163–3188.

Rodger, C. J., S. Werner, J. B. Brundell, E. H. Lay, N. R. Thomson, R. H. Holzworth, and R. L. Dowden, 2006: Detection efficiency of the VLF World-Wide Lightning Location Network (WWLLN): Initial case study. *Ann. Geophys.*, **24**, 3197–3214.

Rogers, R., 2010: Convective-scale structure and evolution during a high-resolution simulation of tropical cyclone rapid intensification. *J. Atmos. Sci.*, **67**, 44–70.

——, R., P. Reasor, and S. Lorsolo, 2013a: Airborne doppler observations of the inner-core structural differences between intensifying and steady-state tropical cyclones. *Mon. Wea. Rev.*, **141**, 2970–2991.

——, and coauthors, 2013b: NOAA'S Hurricane Intensity Forecasting Experiment: A progress report. *Bull. Amer. Meteor. Soc.*, **94**, 859–882.

——, P. Reasor, and J. Zhang, 2014: Multiscale structure and evolution of Earl (2010) during rapid intensification. *Extended Abstracts, 31st Conf. on Hurr. and Trop. Meteor.*, San Diego, CA, Amer. Meteor. Soc.

Rozoff, C. M., C. S. Velden, J. Kaplan, A. Wimmers, and J. P. Kossin, 2012: Improvements in the probabilistic prediction of tropical cyclone rapid intensification resulting from inclusion of satellite passive microwave observations. *Extended Abstracts, 30th AMS Conf on Hurr. and Trop. Meteor.*, Ponte Vedra Beach, FL, Amer. Meteor. Soc.

Sanger, N. T., M. T. Montgomery, R. K. Smith, and M. M. Bell, 2014: An observational study of tropical cyclone spinup in Supertyphoon Jangmi (2008) from 24 to 27 September. *Mon. Wea. Rev.*, **142**, 3–28.

Sapiano, M., W. Berg, D. McKague, and C. Kummerow, 2013: Towards an intercalibrated fundamental climate data record of the SSM/I Sensors, *IEEE Transactions on Geoscience and Remote Sensing*, **51**, 1492–1503.

Schubert, W. H., and J. J Hack, 1982: Inertial stability and tropical cyclone development. *J. Atmos. Sci.*, **39**, 1687–1697.

Spencer, R. W., H. M. Goodman, and R. E. Hood, 1989: Precipitation retrieval over land and ocean with the SSM/I: Identification and characteristics of the scattering signal. *J. Atmos. Oceanic Technol.*, **6**, 254–273.

Steranka, J., E. B. Rodgers, and R. C. Gentry, 1986: The relationship between satellite measured convective bursts and tropical cyclone intensification. *Mon. Wea. Rev.*, **114**, 1539–1546.

Vigh, J. L., and W. H. Schubert, 2009: Rapid development of the tropical cyclone warm core. *J. Atmos. Sci.*, **66**, 3335–3350.

Vila, D., R. Ferraro, H. Meng, and J. Janowiak, 2007: Large-scale validation of daily rainfall estimates of uncorrected and corrected AMSU-B derived rain rate retrievals. *Extended Abstracts, Joint 2007 EUMETSAT Meteorological Satellite Conference and the 15th Satellite Meteorology & Oceanography Conference of the American Meteorological Society,* Amsterdam, Netherlands, September 24–28 2007.

Vivekanandan, J., J. Turk, and V. N. Bringi, 1991: Ice water path estimation and characterization using passive microwave radiometry. *J. Appl. Meteor.*, **30**, 1407–1421.

Willoughby, H. E., 1990: Temporal changes of the primary circulation in tropical cyclones. *J. Atmos. Sci.*, **47,** 242– 264.

——, F. D. Marks, and R. J. Feinberg, 1984: Stationary and moving convective bands in hurricanes. *J. Atmos. Sci.*, **41**, 3189–3211.